High-Resolution fs/ps CARS for Quantitative Measurements of Temperature and Species in a Dual-Mode Scramjet

---

A Thesis

Presented to

the Faculty of the School of Engineering and Applied Science

University of Virginia

In Partial Fulfillment

of the requirements for the Degree

Master of Science (Mechanical and Aerospace Engineering)

by

Alan Junghoon Kim

August 2023

Approval Sheet

This Thesis is submitted in partial fulfillment of the requirements for the degree of

Master of Science (Mechanical and Aerospace Engineering)

Alan Junghoon Kim

This Thesis has been read and approved by the Examining Committee:

Dr. Chloe Dedic, Advisor

Dr. Harsha Chelliah, Chair

Dr. Christopher Goyne

Accepted for the School of Engineering and Applied Science:

Jennifer L. West, Dean, School of Engineering and Applied Science

August 2023

But when the goodness and loving kindness of God our Savior appeared, he saved us, not because of works done by us in righteousness, but according to his own mercy, by the washing of regeneration and renewal of the Holy Spirit, whom he poured out on us richly through Jesus Christ our Savior, so that being justified by his grace we might become heirs according to the hope of eternal life (Titus 3:4-7). Therefore whatever you do, in word or deed, do everything in the name of the Lord Jesus, giving thanks to God the Father through him (Col. 3:17).

Acknowledgments

Firstly, I would like to thank my mother, who loved and raised me. I have only reached this point in life and in my education because of your hard work, love, and care. From our humble beginnings in the Midwest to navigating the challenges of New York, I will always appreciate the time and energy you sacrificed to put me through college and into adulthood. I'd also like to thank my father, who was a source of great council during my studies. Your experience, wisdom, and advice helped me get through difficult points in graduate school.

Next, I would like to thank my advisor Dr. Chloe Dedic for your support and guidance during graduate school. I will always appreciate the opportunity you gave to me to come and work and study at the University of Virginia. I admire your work ethic and passion for what you do every day and the amount of energy you give to helping us, your students. Thank you for teaching and mentoring me as a researcher, and for being patient with me when I was struggling with the stresses of graduate school and life.

My time in Charlottesville would not have been the same had I not met the wonderful people at Jefferson Park Baptist Church. Thank you for the friendship, community, and love you have given me in my time here. Special thanks to Hoon, Keith, Zach, John Mark, Jacob(s), Natalie, Noel, and many others whom I hope to be lifelong friends with. Your friendship has been an incredible blessing and has been extremely meaningful during this time.

Additional thanks to my cohort and lab mates in the Reacting Flow and Aerospace Research Laboratories, as well as Dr. Andrew Cutler of the George Washington University

for significant guidance and laboratory assistance. I would also like to thank Dr. Robert Rockwell for your help and time with operation of the combustion tunnel and help during experiments. Thank you Ryan, for your help in countless experiments and answering all of my questions. Andrew and Laurie, joking around with you guys in lab was a source of joy during the workday and I appreciate your friendship. Special thanks to Zach and Owen for being trustworthy partners on our project.

Funding for the work done in this thesis was provided by the Department of Mechanical and Aerospace Engineering and the Defense Advanced Research Projects Agency (DARPA) Young Faculty Award (Grant #HR00112010014).

Contents

Acknowledgments **iii**

Contents **v**
  List of Tables vii
  List of Figures viii

Abstract **1**

1 Introduction **2**
  1.1 Motivation 2
  1.2 Scramjet Engines 3
    1.2.1 Flameholding 3
    1.2.2 Ground Testing of Scramjets: Optical Diagnostics 4
  1.3 Coherent anti-Stokes Raman Scattering (CARS) 6
    1.3.1 CARS in Scramjet Engines 6
    1.3.2 Hybrid fs/ps CARS 7
    1.3.3 CARS Spatial Resolution 8
  1.4 Research Objectives 10
  1.5 Thesis Summary 11

2 Theory and Experimental Methods **13**
  2.1 Hybrid fs/ps CARS 13
  2.2 Optical Setup 15
  2.3 Picosecond Pulse Shapers 18
    2.3.1 4f-Pulse Shaper 18
    2.3.2 Second Harmonic Bandwidth Compressor 19
  2.4 CARS Spectral Modeling 22
  2.5 CARS Spectral Fitting 24

3 Counter-propagating fs/ps CARS **33**
  3.1 Motivation and Objectives 33
  3.2 Experimental Setup 35
    3.2.1 Optical Layout 35
    3.2.2 Microscale Gas Jet 37
    3.2.3 Schlieren Imaging of the Microscale Gas Jet 39

3.2.4 Estimated Probe Volume Size 42
3.2.5 Measuring Spatial Resolution 43
3.2.6 Adjustment of Probe Volume Location using Temporal Overlap . . . 44
3.3 Results and Discussion 45
3.3.1 Spatial Resolution 45
3.3.2 Temperature Measurements of a Microscale Gas Jet 48
3.3.3 Adjustment of Measurement Volume Location with Relative Pulse Timing 52
3.4 Conclusion 53

4 fs/ps CARS in a Dual-Mode Scramjet 55
4.1 Motivation and Objectives 55
4.2 Experimental Setup 56
4.2.1 University of Virginia Supersonic Combustion Facility 56
4.2.2 Optical Setup 57
4.2.3 Spatial Resolution 64
4.3 Facility Considerations 66
4.3.1 CARS System Stability 66
4.3.2 Test Section Windows 67
4.4 Test Cases and Measurement Locations 69
4.5 Results and Discussion 71
4.5.1 Temperature Measurements 71
4.5.2 Qualitative Fuel Distributions 81
4.6 Conclusion 88

5 Quantifying Local Equivalence Ratio with fs/ps CARS 90
5.1 Motivation and Objectives 90
5.2 CARS Spectral Modeling of Fuel Species 91
5.2.1 Hydrogen (H_2) 91
5.2.2 Ethylene (C_2H_4) 95
5.3 Calibration Method 99
5.4 Experimental Setup 100
5.5 Results and Discussion 102
5.5.1 Preliminary Model Validation 102
5.5.2 Low Temperature Calibration for Measuring Local Equivalence Ratio 104
5.6 Conclusion 108

6 Summary and Future Work 110
6.1 Summary 110
6.2 Future Work 111

Bibliography 113

List of Tables

1.1 Measured CARS spatial resolution for various phase-matching schemes. 9

2.1 Pixel corresponding to the maximum CARS signal intensity at various temperatures and ps probe delays. 27

3.1 Beam energies used in the experiment for each pulse duration. 37
3.2 Pulse Duration vs. Measured Probe Volume Size 47

4.1 Fueling conditions used for CARS measurement campaign. 69

5.1 Molecular constants for calculating H_2 line positions. 93
5.2 Molecular constants for calculating H_2 Raman intensities. 93
5.3 Vibrational constants for calculating C_2H_4 energy levels. 97
5.4 Raman cross sections relative to N_2 for the Raman-active vibrational modes of Ethylene. 98
5.5 Flow rates used and corresponding concentration of C_2H_4. 101
5.6 Measured mole fraction of C_2H_4 using the constant K determined from the ν_1 band of C_2H_4. Measurements are shown for T = 300 K to 500 K in increments of 50 K. 105
5.7 Values for K found for 300 K to 500 K for the ν_1 band of C_2H_4. 105
5.8 Measured mole fraction of C_2H_4 for T = 300 K for each band of C_2H_4. 108

List of Figures

2.1 Folded BOXCARS phase matching scheme. 14

2.2 CARS energy level diagrams for both Q and S-branch CARS. a) Q-branch. b) S-branch. 15

2.3 Timing diagram of the CARS process. 15

2.4 General experimental setup for performing vibrational fs/ps CARS. 16

2.5 General experimental setup for performing rotational fs/ps CARS. 17

2.6 $4f$-pulse shaper. 18

2.7 SHBC Layout. 20

2.8 A) and C) show experimentally measured time profiles of the SHBC output at two different stretcher positions along with a Gaussian fit, and B) and D) show the Fourier transform of the measured time profile in panels A and C (respectively) showing the bandwidth in frequency. 22

2.9 Sample CARS spectra showing shot-to-shot fluctuations in line positions. . . 26

2.10 Simulated CARS spectra at the three probe delays used in the current thesis. A) 4.5 ps. B) 32 ps. C) 42 ps. 26

2.11 Line positions corrected with Method B. 29

2.12 A) Scatter plot of fit temperature compared to the magnitude of shift computed using Method B. B) Scatter plot showing the difference between the fit temperature with and without correcting for the shift as a function of the shift magnitude. 29

2.13 A) Correlation plot comparing the fit temperature for each frame with and without correcting for frequency shift. B) Correlation plot comparing the fit temperature obtained using Method A vs. Method B. 30

2.14 Comparison of fit temperatures resulting from Method A (NLLSQ) vs. Method B. Data was taken in Case 1 at position 6.1 with a probe delay of 4.5 ps. . . 31

2.15 Additional comparison of fit temperatures resulting from the Method A (NLLSQ) vs. Method B. Data was taken in Case 1 at position 6.1 with a probe delay of 4.5 ps. 32

3.1 Folded BOXCARS phase matching scheme for the counter-propagating fs/ps CARS set up. 34

3.2 Schematic of the optical layout used in the counter-propagating CARS experiment. 35

3.3 Photograph of the optical layout used in the counter-propagating CARS experiment with beam paths added. 36

3.4 Schematic of the optical layout of the Schlieren imaging system used to visualize the gas jet at the exit of the hypodermic needle. 40
3.5 Schlieren image of the microscale gas jet. 41
3.6 A) Abel inversion of the Schlieren image. B) Reconstruction of gas jet from Abel inversion. 41
3.7 CARS signal intensity vs. glass position for various pulse durations. 46
3.8 Estimated probe volume size vs. pulse duration 47
3.9 Temperature measurements of the cold air jet with 60 fs pulses. Reported temperature is the average fit temperature to 300 shots. Vertical bars represent one standard deviation in temperature in each direction. 49
3.10 Sample CARS temperature fits at various jet positions. A) $\Delta x = -65$ µm. B) $\Delta x = -25$ µm. C) $\Delta x = -5$ µm 51
3.11 Location of the CARS measurement volume vs. pump delay stage position for 200 fs pulses. Blue symbols shows displacement of the measurement volume after a change in temporal overlap of pump/Stokes without simultaneous adjustment of spatial overlap for signal optimization. Red symbols shows data set when spatial overlap was reoptimized after a change in temporal overlap. 52

4.1 Schematic of the combustor geometry showing the location of the fuel injectors used in the experiment. 57
4.2 Optical layout of the CARS laser cart and primary/secondary CARS systems. PC: pulse compressor. OPA: optical parametric amplifier. BS: beam splitter. SHBC: second harmonic bandwidth compressor. A detailed diagram of the Transmission/Collection plates is shown in Fig. 4.7. 58
4.3 Time profile of the SHBC output used in the experiment. The measured pulse duration was 2.47 ps. 59
4.4 Beam routing in UVA Supersonic Combustion Facility. 60
4.5 Initial design of the optical plates used in the experiment. 61
4.6 Beam profile images of the Stokes beam at the focal plane. A) No telescope. B) With telescope. 62
4.7 Beam path and optical setup of the transmission and collection plates shown in Fig. 4.4 used to overlap the beams in the combustion tunnel. 63
4.8 Estimate of the CARS measurement volume derived from the simulation of the argon jet and the experimental measured convolution of the Ar jet and the CARS probe volume. 65
4.9 A) Measured CARS signal intensity during tunnel operation. B) Shot to shot CARS signal intensity while the tunnel was in operation with and without combustion. 66
4.10 Photograph of the window degradation prohibiting CARS measurements. . . 68
4.11 Coolant present in the test section. 68
4.12 Wall pressure measurements for Cases 1, 2, and 3. 70
4.13 Nomenclature for CARS measurement locations in the model scramjet. . . . 70
4.14 A) Sample single-shot CARS with the resulting best-fit temperature. B) Histogram corresponding to Case 1, position 4.1. Average fit temperature: 2075 K. Temperature standard deviation: 223 K. 72

4.15 Averaged CARS spectra acquired at three probe delays. A) 4.5 ps, B) 32 ps, C) 42 ps. 73
4.16 Histograms of temperature fits for a probe delay of 4.5 ps (A) and 42 ps (B). Data acquired at position 7.1 for Case 1. 74
4.17 CARS data set acquired at a 32 ps probe delay. Data acquired at position 1.5 for Case 3. A) Sample temperature fit at a probe delay of 32 ps. B) Histogram of temperature at position 1.5 for Case 3. 74
4.18 Average fit temperatures in the combustor. A) Case 1. B) Case 2. C) Case 3. 75
4.19 Contour plots of average fit temperatures for measurement positions located in the region cavity. Measurements at the discrete locations were interpolated to generate the contour plots. A) Case 1. B) Case 2. C) Case 3. 76
4.20 Contour plots of the standard deviations corresponding to the data shown in Fig. 4.19. A) Case 1. B) Case 2. C) Case 3. 77
4.21 Temperatures at various x-positions in the cavity for cases 1, 2, and 3. x = 0 corresponds to the beginning of the cavity step. A) Measurement Row 1. B) Measurement Row 2. C) Measurement Row 3. 80
4.22 Histograms of fit temperatures for Case 3 at positions 5.1 (A), 5.2 (B), and 5.3 (C). 81
4.23 A) CARS spectra recorded at a 4.5 ps probe delay with C_2H_4 present. Data recorded at position 1.5 for Case 2. B) Histogram of measured peak ratios at this position. 82
4.24 Average C_2H_4 peak ratio upstream of the cavity. A) Case 1. B) Case 2. C) Case 3. 83
4.25 C_2H_4 peak ratio standard deviation upstream of the cavity. A) Case 1. B) Case 2. C) Case 3. 84
4.26 Contour plots of average C_2H_4 peak ratios in the cavity. A) Case 1. B) Case 2. C) Case 3. 85
4.27 Contour plots of C_2H_4 peak ratio standard deviation in the cavity. A) Case 1. B) Case 2. C) Case 3. 86
4.28 Correlation between measured relative fuel concentration and measured temperature. Data recorded at Case 2, position 2.4 with CARS spectra acquired at 32 ps. 88

5.1 Stick diagram of Q-branch line positions and Raman intensities for H_2 at T = 273 K. 94
5.2 Boltzmann distributions of H_2 at three different temperatures: T = 273 K, T = 1200 K, and T = 2000 K. 94
5.3 Q-branch CARS spectra of H_2. $T = 273$ K, $\tau_{probe} = 6$ ps. 95
5.4 Energy level diagram accounting for zero-point energy for ν_1, ν_2, and ν_3 modes of C_2H_4 from v = 0 to v = 6. 98
5.5 Simulated Raman spectrum of ν_1, ν_2, and ν_3 modes of C_2H_4 at T = 1100 K. 99
5.6 CARS optical layout used to acquire spectra of heated mixtures of ethylene and air. 101

5.7 A) CARS spectra obtained at 300 K (blue) and 500 K (red) for a mixture consisting of 20% ethylene and 80% air. The spectra demonstrate how the spectral features change with temperature (B) and species concentration (C). 102

5.8 A comparison of the fs/ps CARS model (red) and experimental measurements (blue) at 300 K. 103

5.9 Experimental CARS spectra of a mixture of Ethylene and air. Both spectra are normalized to Nitrogen. 104

5.10 Measured mole fractions of C_2H_4 obtained from the ν_1 band of C_2H_4 are plotted as a function of mole fraction determined from the mass flow controller. The trend line represents the relationship between the measured mole fractions and the known mole fractions. 106

5.11 Calibration curve generated from values of K found from T = 300 K to 500 K. 107

5.12 Measured mole fractions of C_2H_4 from the ν_2 and ν_3 bands of C_2H_4, and trend line as a function of mole fraction determined from mass flow controller. . . . 107

Abstract

High-resolution quantitative measurements of thermodynamic properties provide key insight into the fundamental combustion processes occurring within a scramjet engine. Quantitative measurements are necessary for validating numerical simulations of the reacting flowfield, locating reaction zones, and elucidating flame stabilization mechanisms within a scramjet engine.

A novel counter-propagating (CoP) phase-matching configuration for hybrid femtosecond/picosecond coherent anti-Stokes Raman scattering (fs/ps CARS) is demonstrated to have ultra-high spatial resolution on the order of 10's of µm. This represents a significant improvement over traditional phase matching schemes, enabling precise measurements in regions with steep temperature gradients and minimizing the impact of spatial averaging. Utilizing the CoPCARS system, the temperature gradient resulting from a high-velocity microscale gas jet emanating from a hypodermic needle (51 µm inner diameter) was accurately quantified.

To quantify temperature and relative species concentration in the flow of a dual-mode scramjet combustor, a fs/ps CARS system is developed and implemented in the University of Virginia Supersonic Combustion Facility (UVaSCF). Temperature measurements using fs/ps CARS within the combustor are presented for various fueling configurations. Ongoing work to develop a CARS spectral model for quantifying local equivalence ratio is discussed, and preliminary comparisons between experimental spectra and the spectral model are presented.

Chapter 1

Introduction

1.1 Motivation

The purpose of this thesis is to develop an instrument for investigating reacting flows with small characteristic spatial scales. Firstly, it aims to enhance the spatial measurement resolution of hybrid femtosecond/picosecond coherent anti-Stokes Raman scattering (fs/ps CARS) by employing counter-propagating fs pulses. An increase in the spatial resolution of CARS would maximize the utility of fs/ps CARS for precise measurements of temperature and species concentration in scramjet engines.

Secondly, the thesis aims to utilize fs/ps CARS for quantitative measurements of temperature and species concentration in a dual-mode scramjet. Specifically, it focuses on investigating how variations in local fuel-to-air distributions impact the local temperature and fuel concentration in partially-premixed ethylene/air flames. This investigation is conducted within a model scramjet combustor in the University of Virginia Supersonic Combustion Facility (UVaSCF).

This thesis provides the necessary background, theory, and methodologies for developing a counter-propagating fs/ps CARS system, as well as integrating a fs/ps CARS system within the UVaSCF for measurements in a scramjet. Discussion of the results from both sets of experiments are also given.

1.2 Scramjet Engines

Air-breathing engines have emerged as promising solutions for enabling sustained and repeatable hypersonic flight, offering high specific impulse and long-range capabilities at high Mach number conditions [1]. Ramjets utilize the incoming airflow resulting from the forward motion of an aircraft to generate ram pressure. The incoming flow is compressed and decelerated to subsonic speeds at the inlet of the engine. Fuel injection and combustion take place in the combustor while the flow remains subsonic. The resulting high-enthalpy flow then accelerates to supersonic velocities through a converging-diverging nozzle at the exit of the engine, generating thrust as the reacting flow leaves the engine with greater velocity and momentum than it had at the inlet [1].

The concept of utilizing ram pressure for propulsion was explored as early as 1913, and the patenting of ramjets for supersonic flight began in the 1930s [2]. Ramjets have a simplistic design, lack of moving parts, and the capability to compress air through changes in internal geometries. These features, combined with their efficiency at supersonic flight speeds where gas-turbine engines become less effective, make ramjets the ideal propulsion system for supersonic flight between Mach 3 and Mach 6. However, as flight speeds exceed Mach 6, the efficiency of traditional ramjets diminish, necessitating combustion within a supersonic flow [3]. Instead, ramjets where combustion occurs under supersonic conditions—supersonic combustion ramjets (scramjets)—offer the potential for improved efficiency at higher vehicle velocities.

1.2.1 Flameholding

Scramjet engines require stable combustion within the engine to achieve optimal propulsion efficiency and maintain consistent thrust production. The integration of scramjets on practical aircraft has been impeded by significant challenges associated with flame instability during ram to scram transitions [4]. Combustion instability within the engine can lead to undesirable phenomena such as flame blowout or flame propagation upstream, resulting in engine unstart and abrupt loss of thrust [5].

Flame stability in scramjet engines is dependent upon the balance between flame propagation and local gas velocity. However, the fluid velocity in these engines often exceeds the flame speed, leading to variations in flow residence time and chemical reaction rates across a wide range of flight conditions. This can result in unfavorable conditions for achieving stable combustion in scramjet engines [3, 6]. Flameholding in dual-mode combustors is also difficult to achieve because of the need to achieve flame ignition and stabilization across diverse flow speeds, including the ram-to-scram mode transition where the mechanism and location of combustion stabilization often changes [7].

To address these challenges and enhance combustion stabilization, cavity flameholders are commonly employed in dual-mode combustors [8]. Incorporating a cavity creates a recirculation zone within the flow, promoting extended residence time for fuel/air mixing and chemical reactions as well as generating a stabilizing cavity shear layer. Additionally, the cavity serves as a source of heat and radical formation, aiding ignition and stabilization of combustion in the main flow [7]. Previous studies have demonstrated the efficacy of cavity flameholders in improving the combustion efficiency of hydrocarbons in supersonic environments [9, 10, 11].

1.2.2 Ground Testing of Scramjets: Optical Diagnostics

Quantitative thermodynamic measurements throughout the flowpath are vital for improving understanding of the combustion processes occurring within a scramjet engine. Quantitative measurements can also be used to validate numerical simulations of the reacting flowfield.

While wall-based instrumentation can prove quantitative measurements of wall temperature and pressure, optical diagnostic methods have emerged as effective tools for studying supersonic combustion through in-stream measurements and visualization. Among the optical imaging techniques used, planar laser-induced fluorescence (PLIF) and 3D tomographic chemiluminescence have proven particularly valuable [12]. PLIF allows for the visualization of flame structures and in some circumstances the quantification of species concentrations, providing insights into product formation and reaction regions in the combustor [13, 14, 15]. Similarly, 3D tomographic chemiluminescence enables the three-dimensional reconstruction of flame structures, aiding in the understanding of flame behavior and stabilization mechanisms [16].

Other optical methods have been employed to investigate various aspects of the scramjet combustion process. Raman scattering, for instance, has been utilized to probe molecular composition and temperature distributions within the flowfield [17, 18]. Laser-Induced Breakdown Spectroscopy (LIBS) has been employed for studies of fuel-air mixing and combustion efficiency [19, 20]. Laser Absorption Spectroscopy has also been applied to measure the concentration of specific species in the combustor of a scramjet [21]. Additionally, Imaging Fourier-transform spectroscopy (IFTS) has been used to map out temperature and fuel distribution within the cavity of a scramjet combustor [22].

Some of these optical measurement techniques suffer from limitations such as path integration (PLIF, IFTS) or limited spatial resolution (LIBS). Path-integrated measurements provide information about the average properties along the entire path of the optical beam, which can restrict the accuracy and precision of the obtained measurements. Limited spatial resolution poses challenges in capturing spatial gradients within the combustion region. Methods such as PLIF suffer from limited accuracy in measurements of concentration due to variable collisional quenching in reacting flows. Furthermore, techniques such as FTS suffer from low temporal resolution as measurements must average over a period of time.

1.3 Coherent anti-Stokes Raman Scattering (CARS)

One laser-based method of measurement that overcomes these limitations is coherent anti-Stokes Raman scattering (CARS). CARS involves the spatio-temporal overlap of three laser pulses: pump, Stokes, and probe pulses. When overlapped, the three pulses generate a coherent, laser-like signal referred to as CARS. This signal carries information about the thermodynamic state of the molecules within the overlapping region. CARS enables spatially and temporally resolved, in-stream measurements of thermodynamic properties, including local temperature and species composition. Greater discussion on the theory of CARS is discussed in Chapter 2.1 of this thesis.

CARS has gained favor in fundamental combustion research due to its high spatio-temporal resolution, accuracy, and precision [23, 24, 25, 26]. The high spatio-temporal resolution of CARS measurements, along with the fact that that it is non-intrusive to the flow under study, make CARS suitable for studying dynamic, high-temperature environments such as scramjets. This non-intrusive nature eliminates the need for physical probes or sensors in the flowfield, reducing perturbations in the flowfield due to instrumentation.

1.3.1 CARS in Scramjet Engines

Nanosecond (ns) CARS has already been successfully used to quantify local flow properties within a hydrogen-fueled scramjet engine [27, 28]. It has also been used in the University of Virginia Supersonic Combustion Facility (UVaSCF) to study both hydrogen-air flames and fully-premixed ethylene-air flames in a scramjet [29, 30].

However, the use of ns lasers in these experiments introduced certain limitations. One of the key challenges was the insufficient spatial resolution, as observed in the experiment described in Ref. [30]. While flame structures on the order of 100 µm were observed, the length of the CARS measurement was 0.7 mm. This was measured by translating a C_2H_4-air gas mixture along the measurement volume to the limits where any significant C_2H_4 CARS signal could be detected [30].

This resulted in significant spatial averaging, compromising the ability to capture fine-scale details and gradients in flow properties throughout the flow. Thus, an increase in the spatial resolution available with CARS is called for to maximize the utility of the method to quantify local flow properties in a scramjet engine.

Another issue associated with ns pulse durations was the high laser energy required to generate a Raman coherence. The high-energy laser pulses would damage the windows of the combustor, which were necessary for optical access. To address this problem, window box extensions were employed to enable optical access without the use of windows [30]. However, the presence of the window boxes resulted in additional issues, such as restricting the available measurement planes and modifying the local flowfield. Specifically, placing the window boxes in the plane of the cavity introduced a recirculation region for the flow, allowing the low-velocity flow to enter the boxes which would prevent flame stabilization. Consequently, measurements in the plane of the cavity flameholder were unattainable with ns CARS.

Measurements of temperature and species concentrations in the cavity are important in order to study flame stabilization and locate reaction zones for various fueling configurations in a scramjet. As mentioned earlier, the cavity assists ignition and stabilization of combustion in the engine. Measurements of temperature and species in this region would help correlate local fuel-air ratios and temperature, providing insight into how the performance of the engine changes with various operating conditions.

1.3.2 Hybrid fs/ps CARS

The development of pulsed lasers with higher repetition rates and shorter pulse durations on the order of femtoseconds (fs) have resulted in the development novel CARS techniques such as hybrid femtosecond/picosecond (fs/ps) CARS, which has the potential to overcome the limitations of ns CARS for use in a scramjet. Hybrid fs/ps CARS has been demonstrated successfully for gas-phase thermometry and measurements of relative species concentration in gas mixtures [31, 32, 33, 34].

The utilization of fs lasers in CARS measurements brings several advantages, particularly in the context of reacting gas-phase flows. The use of fs lasers enables data acquisition rates on the order of 1 kHz [35]. Hybrid fs/ps CARS also exhibits the ability to suppress non-resonant background. This can increase signal-to-noise ratios in spectra, allowing for more accurate and reliable measurements. Additionally, fs CARS is also insensitive to collisions [36].

1.3.3 CARS Spatial Resolution

As mentioned previously, improvement in the spatial resolution of CARS is necessary to fully maximize its utility to study combustion in scramjet engines. A temperature gradient within the CARS measurement volume itself hinders the accuracy of CARS measurements, an effect known as spatial averaging error. For example, Zhu et al. reported spatial averaging errors exceeding 300 K in typical flame sheets [37]. While spatial averaging effects on the CARS temperature measurement for N_2 are well known [38, 37, 39], Cutler et al. found while performing ns CARS in the UVaSCF that spatial averaging effects arising from the multi-species environment led to further uncertainty in measured temperatures due to the thin flame fronts (on the order of 100 µm) [30].

The nonlinear relationship between CARS signal intensity and number density leads to temperature measurements biased towards the lower temperature regions of the measurement volume, resulting in spatial averaging bias [40]. Measurements with spatial averaging fail to reflect the mean temperature of the gas within the measurement volume or the temperature at the center of the measurement volume. Therefore, achieving sufficient spatial resolution is vital for accurate measurements in flows with steep temperature gradients.

The spatial resolution of the CARS probe volume is determined by the spatial and temporal overlap of the three beams. Reducing the size of the region where the beams

Table 1.1: Measured CARS spatial resolution for various phase-matching schemes.

Phase matching scheme	Longitudinal resolution
Collinear	∼1-2 cm [41]
BOXCARS	∼700 µm - 1.3 mm [30, 42, 43, 44]
USEDCARS	∼3 mm [41]

overlap can increase the measurement resolution. Table 1.1 provides a summary of reported spatial resolutions for various phase-matching schemes. As seen in the table, different phase matching configurations can be employed for CARS signal generation, each offering varying degrees of spatial resolution.

Folded BOXCARS, a phase-matching configuration commonly used in CARS experiments [45, 46], has yielded the highest spatial resolution compared to other phase-matching configurations. Folded BOXCARS results in an ellipsoidal probe volume typically measured to be around 1 mm in length with some variance that depends on specific experimental configurations [30, 42, 43, 44].

The spatial resolution of the measurement volume in folded BOXCARS can be adjusted by changing the beam crossing angles. For instance, a crossing angle as steep as 33° can theoretically achieve spatial resolution on the order of 65 µm [44]. However, increasing the crossing angle significantly poses challenges in large-scale test facilities such as wind tunnels, which have limited optical access and space.

The use of counter-propagating fs pulses has the potential to enable spatial resolution on the order of ∼10 µm due to the fact that the length of the interaction of the pulses would be limited to the width of the pulses in time. CARS using counter propagating beams (CoPCARS) has been previously explored theoretically as a viable phase matching configuration for experimental convenience and large spatial separation of CARS signal [47, 48]. CoPCARS has been used by Laufer et al. for angularly resolved CARS [49] and for 1D imaging with ps CARS by Kliewer et al. [50], but counter-propagating CARS with fs pulses has not yet been established as a viable method of measurement until the work discussed in this thesis.

Various fields of study require increased CARS measurement resolution to avoid spatial averaging effects. For example, turbulent combustion studies have observed flame structures with Kolmogorov length scales on the order of 70 µm [51, 52]. In such cases, a CARS interrogation volume larger than 70 µm would result in spatial averaging of microscale product and reactant regions. Additionally, flowfields with spherical shocks necessitate increased CARS resolution to accurately quantify gradients in local flow properties [42].

These examples illustrate the insufficiency of current CARS phase matching geometries to avoid spatial averaging in various experiments. An increase in CARS measurement resolution while maintaining a reduced experimental footprint is necessary to maximize the utility of CARS in different environments such as scramjet engines. As mentioned earlier, OH PLIF experiments in the UVaSCF facility have observed flame structures on the order of 100 µm, while the CARS measurement volume was 0.7 mm in length. Therefore, improvement in CARS measurement resolution is crucial to accurately quantify local flow properties and study combustion in scramjet engines.

1.4 Research Objectives

In consideration of the existing literature, this thesis has the following objectives:

- Develop an ultra-high spatial resolution CARS system using counter-propagating fs pulses, accounting for limited optical access in test facilities like the UVaSCF.
- Integrate a fs/ps CARS system in the UVaSCF to quantify local gas temperature and fuel/air equivalence ratio in a dual-mode scramjet combustor and within a cavity flameholder in particular.

For the counter-propagating fs/ps CARS experiment, the specific objectives are as follows:

- Determine the exact spatial resolution achievable using fs counter-propagating CARS for various pulse durations.

- Verify the capability of the fs counter-propagating CARS system to characterize steep temperature gradients due to increased spatial resolution.
- Demonstrate the ability to change the measurement location by adjusting only the relative pulse timing.

For performing hybrid fs/ps CARS in a dual-mode scramjet, the objectives are as follows:

- Develop an experimental hybrid fs/ps CARS system in the UVaSCF scramjet facility to enable CARS measurements throughout the flow path without window extensions that were previously required.
- Acquire CARS measurements of temperature and relative fuel distributions in the cavity of the scramjet.
- Develop a method to quantify local equivalence ratios using fs/ps CARS for ethylene, the fuel species used in this work.

1.5 Thesis Summary

The following is a brief summary of the content covered in the remaining chapters of this thesis:

- Chapter 2 discusses the theory of CARS and the general experimental methods used throughout the experiments presented in this thesis.
- Chapter 3 focuses on the experimental setup, results, and discussion specific to the development and characterization of a counter-propagating fs/ps CARS system.
- Chapter 4 presents the development and integration of a hybrid fs/ps CARS system in the UVaSCF for quantitative measurements of local gas temperature and species concentration in a model scramjet engine.

- Chapter 5 covers the background and methods being pursued for quantifiying local equivalence ratios in the UVaSCF using fs/ps CARS.
- Chapter 6 concludes the thesis by summarizing the work completed and discussing future research opportunities based on the findings of this thesis.

Chapter 2

Theory and Experimental Methods

2.1 Hybrid fs/ps CARS

Hybrid femtosecond/picosecond (fs/ps) CARS is a third-order non-linear optical process involving three laser pulses—two fs pulses and one ps pulse—which are spatially and temporally overlapped to generate a fourth, coherent, laser-like signal. The fs pulses, referred to as the pump and Stokes pulses, excite the molecules in the region where the three beams overlap to a virtual energy state. The use of fs pulses for excitation offers the advantage of inherent broadband excitation, enabling the excitation of transitions over a wide range of frequencies and detection of multiple molecular species. After the system of molecules is excited by the broadband fs pulses, the narrowband ps probe pulse samples the excited system, resulting in the generation of the CARS signal. The narrowband nature of the ps pulse allows for the detection of frequency-resolved CARS spectra with high spectral resolution.

The equation for the propagating electric fields of pump, Stokes, and probe is given by

$$E(\mathbf{k}, t) = E(t) exp(i\mathbf{kr} - i\omega t), \tag{2.1}$$

where ω is the frequency of the wave and $\mathbf{k}$ is the wave propagation vector. CARS signal is generated in accordance with the conservation of energy given by Eq. 2.2,

$$\omega_{\text{pump}} - \omega_{\text{Stokes}} + \omega_{\text{probe}} = \omega_{\text{CARS}}, \tag{2.2}$$

where ω_i represents the respective frequencies of the electric fields involved [53]. In addition to energy conservation, the conservation of momentum must also be obeyed for CARS signal generation. This condition is determined by phase matching, as illustrated in Fig. 2.1 and expressed by Eq. 2.3,

$$\mathbf{k}_{\text{pump}} - \mathbf{k}_{\text{Stokes}} + \mathbf{k}_{\text{probe}} = \mathbf{k}_{\text{CARS}}, \tag{2.3}$$

where $\mathbf{k}_i$ represents the wavevector corresponding to the frequency ω_i.

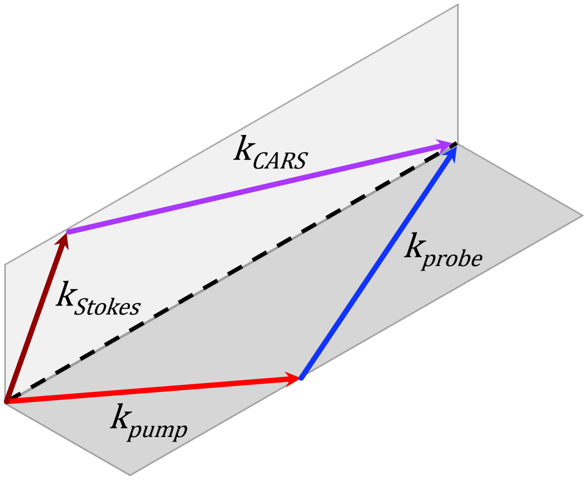

Figure 2.1: Folded BOXCARS phase matching scheme.

The generated CARS signal can then be directed to a spectrometer and camera, allowing for the determination of the thermodynamic state of the molecular system within the measurement volume from the acquired spectra.

Fig. 2.2 presents a frequency diagram of both the vibrational (Q-branch, Δv = 1, ΔJ = 0) and rotational (S-branch, Δv = 0, ΔJ = 2) CARS processes. The choice of the pump/Stokes excitation frequency enables the selective excitation of either vibrational or

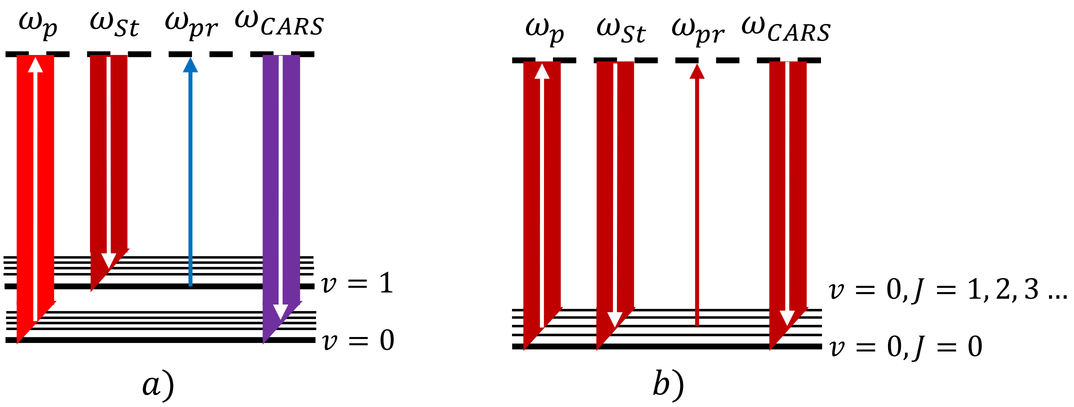

Figure 2.2: CARS energy level diagrams for both Q and S-branch CARS. a) Q-branch. b) S-branch.

rotational transitions of the molecules of interest [23]. Both vibrational and rotational CARS are utilized in the work presented in this thesis.

By delaying the ps probe pulse relative to the initial excitation by the pump and Stokes pulses, non-resonant contributions to CARS spectra can be avoided [31, 54]. A timing diagram of this process is depicted in Fig. 2.3.

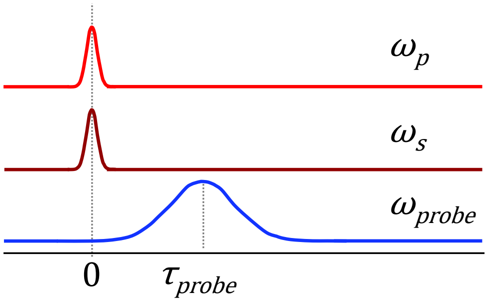

Figure 2.3: Timing diagram of the CARS process.

2.2 Optical Setup

The general experimental setup for performing both vibrational and rotational fs/ps CARS are discussed here. Specific optical layouts for the experiments discussed in this thesis can be found in their respective chapters.

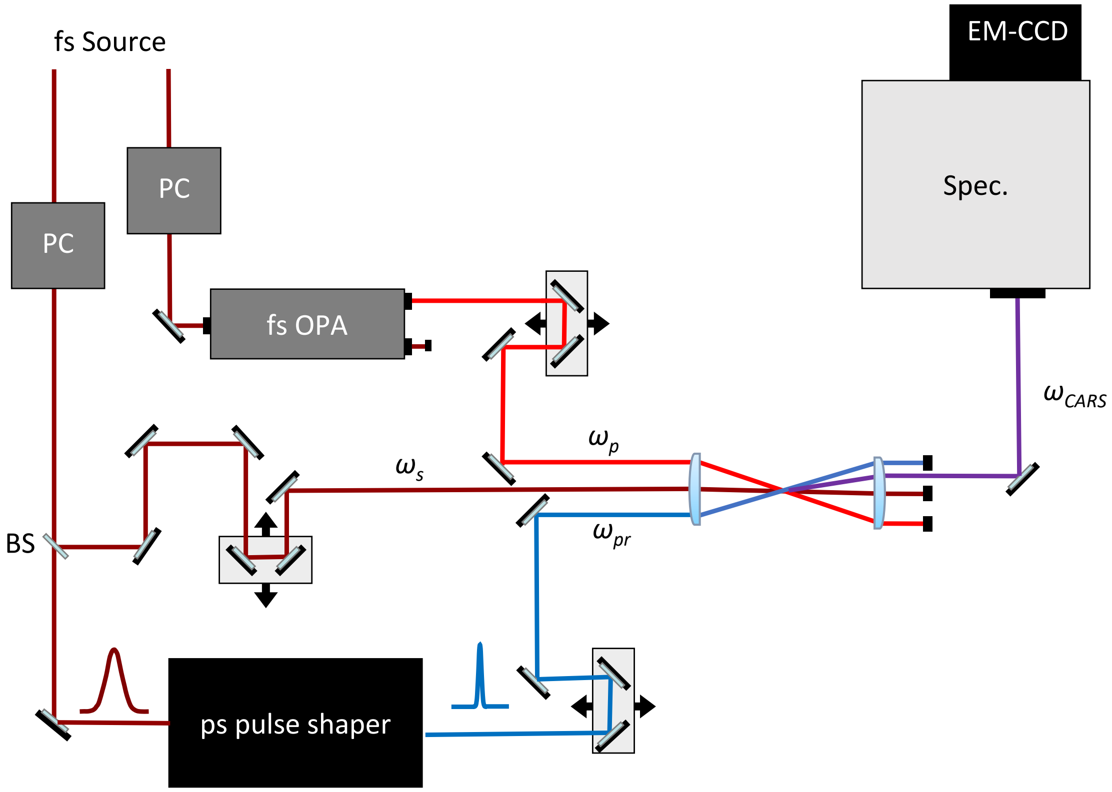

Figure 2.4: General experimental setup for performing vibrational fs/ps CARS.

A diagram of the general optical layout for performing vibrational fs/ps CARS is shown in Fig. 2.4. Here, the pump, Stokes, and probe pulses originate from a single fs source which outputs to two independent pulse compressors. The output of one pulse compressor, pump, is directed to a fs optical parametric amplifier (OPA) to tune the wavelength of the beam to excite Q-branch transitions for the desired molecule. For example, in the experiment discussed in Chapter 4 where N_2 Q-branch CARS is performed, the pump beam is tuned to 674 nm and paired with an 800 nm Stokes beam. The frequency difference between the two electric fields matches the $Q_{0\rightarrow 1}$ transition of N_2 at 2331 cm^{-1}.

The output of the other compressor is directed to a beamsplitter. One portion of the beam is used as the Stokes beam, and the other portion of the beam is directed to a picosecond pulse shaper. The picosecond pulse shaper transforms the broadband fs pulse into a narrowband ps probe pulse. Two pulse shapers are used in this thesis and both are detailed in Chapter 2.3.

A delay stage is included in the beam path for each of the three beams to ensure temporal overlap of the beams at the measurement location. The three beams are then directed to a single spherical focusing lens and crossed in the desired measurement region. CARS signal is generated in the crossing region and is collimated by an additional lens. The CARS signal is then directed to a spectrometer and camera for collection and data acquisition.

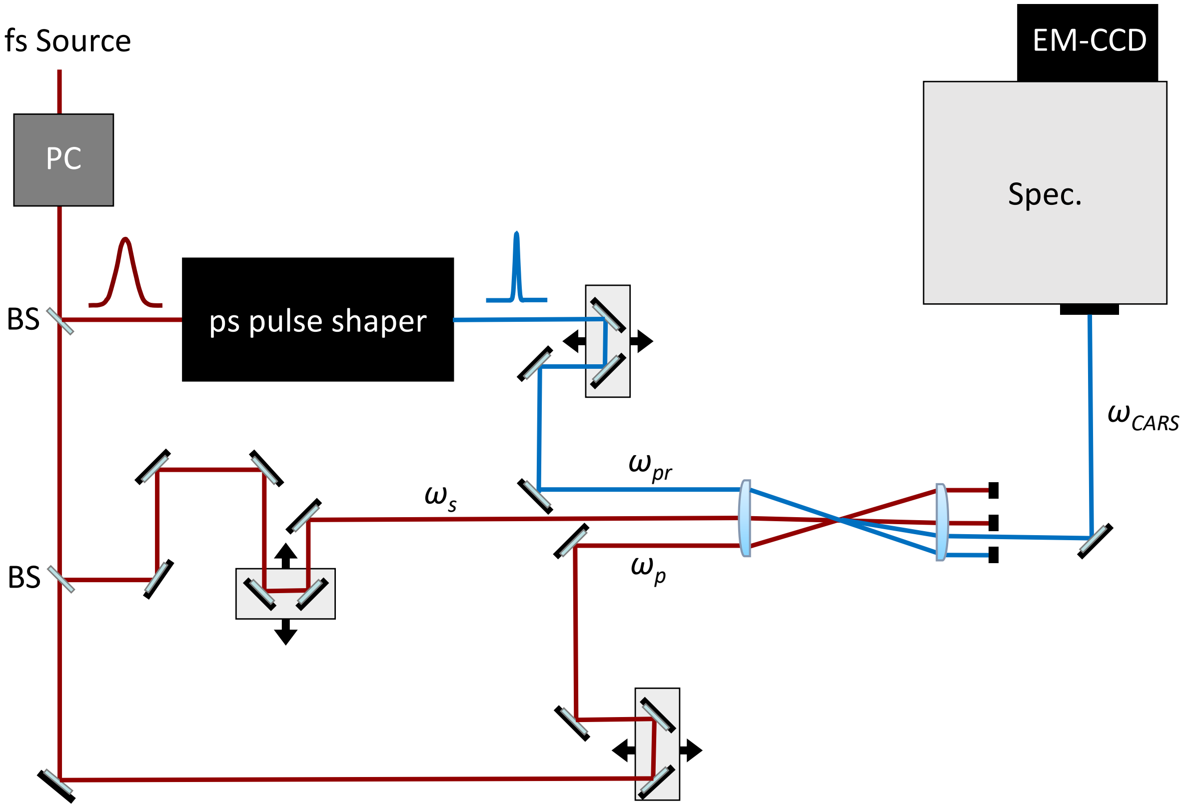

Figure 2.5: General experimental setup for performing rotational fs/ps CARS.

A diagram of the general optical layout for performing rotational fs/ps CARS is shown in Fig. 2.5. Here, degenerate pump and Stokes pulses are used. First, a ∼90/10 beam splitter was used to split 90% of the light to a ps-pulse shaper. Then, a 50/50 beams splitter was used to split the remaining 10% to form the pump and Stokes beams. As in the vibrational CARS set up, travel through delay stages and the three beams are then overlapped via a single focusing lens, and the resulting CARS signal is collimated and directed to a spectrometer and camera for collection.

2.3 Picosecond Pulse Shapers

Two picosecond pulse shapers were used in this thesis: a $4f$-pulse shaper and a second harmonic bandwidth compressor.

2.3.1 4f-Pulse Shaper

The $4f$-pulse shaper stretches the broadband femtosecond pulse into a picosecond pulse with adjustable bandwidth, and is frequently used in fs/ps CARS experiments [55, 35]. A schematic of the $4f$-pulse shaper used in this thesis is shown in Fig. 2.6.

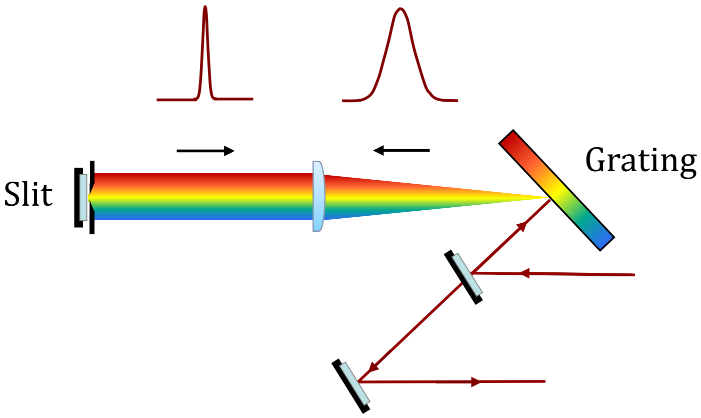

Figure 2.6: $4f$-pulse shaper.

In the $4f$-pulse shaper setup, the incoming beam from the fs laser is first directed onto a diffraction grating, which spatially disperses the frequency components of the beam. A cylindrical lens is placed at a distance of $1f$ away from the grating to collimate the light. This lens then images the spectral distribution of the beam at the Fourier plane, which is also located $1f$ away from the lens. A mirror with an adjustable slit is positioned at this plane to select a portion of the spectral content of the beam. The mirror then reflects the selected bandwidth back to the grating, resulting in a beam that is narrowband in frequency but ps-duration in time.

One of the disadvantages of the $4f$-pulse shaper is that the resulting beam typically has significantly reduced energy compared to the input beam. The typical efficiency of a 4f-pulse shaper is ∼1 to 3% depending on the width of the slit [54]. This reduction in energy can pose challenges, particularly in experiments that require high laser fluence or involve low number density environments, which is true of the high-enthalpy high-speed flows observed in a scramjet engine.

In environments where the available signal is already limited due to the low number density of the molecules being probed, the reduced energy of the output beam from the $4f$-pulse shaper can further limit CARS signal generation. Alternative pulse shaping techniques can be explored to address these challenges and improve the signal-to-noise ratio in such experiments.

2.3.2 Second Harmonic Bandwidth Compressor

One pulse shaper that generates a high-energy narrowband probe pulse is a second harmonic bandwidth compressor (SHBC) [56, 57]. The optical layout of the SHBC used in the fs/ps CARS experiment in Chapter 4 is depicted in Fig. 2.7. The entire system was assembled on a 18”×18” optical breadboard.

In this setup, the 800 nm output from one of the post-amplification pulse compressors in the CARS optical layout is directed onto the breadboard and then to a 50-50 beamsplitter. To ensure an equal split of the beam, a half-wave plate is positioned before the beamsplitter. The beamsplitter divides the incoming beam into two paths.

The reflected portion of the beam from the beamsplitter is directed through a pulse stretcher. The stretcher consists of a diffraction grating with a groove density of 1800 g/mm, a cylindrical lens with a focal length of 200 mm, and a mirror. The mirror and the lens are placed 1 focal length apart on rail mounted on a micrometer stage. The micrometer stage

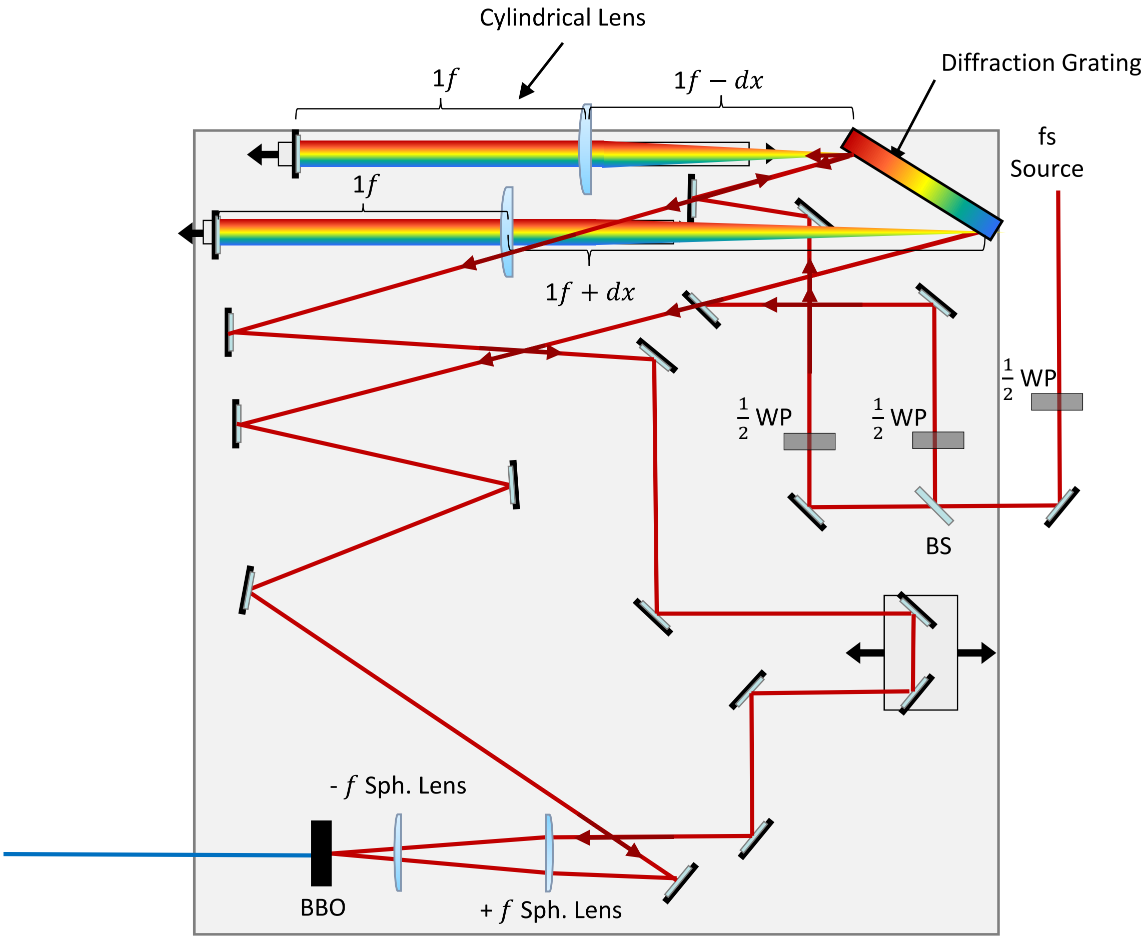

Figure 2.7: SHBC Layout.

allows for adjusting the position of the rail towards the grating, enabling changes in pulse duration.

The transmitted portion of the beam also passes through an identical stretcher system. However, in this case, the stretcher is moved away from the grating to chirp the pulse in the opposite direction compared to the reflected portion. A pulse is chirped when different wavelengths of light contained within a pulse occur at different times. The aim is to stretch each pulse equally in time but to chirp them in opposite directions. In other words, one pulse must be positively chirped—where the higher wavelengths precede the lower wavelengths in time—and the other must be negatively chirped.

The chirp outputs from the stretchers are directed to a beta barium borate (BBO) crystal, where second harmonic generation takes place. By positions of the stretchers, the duration and chirp of the pulses from the stretchers can be matched to achieve optimal second harmonic generation in the BBO crystal. The opposing stretching of the pulses ensures that the frequency pairs of the interacting pulses in the BBO crystal generate a narrowband output after the process of sum-frequency generation. To ensure temporal overlap in the BBO crystal, a delay stage mounted on a micrometer stage is included in the beam path of one of the stretcher legs. The pulse duration and corresponding bandwidth can be adjusted by adjusting the distance between the cylindrical lens and the diffraction grating within the SHBC pulse stretchers.

In order to measure the time profile of the SHBC output, CARS spectra were obtained by scanning the probe pulse in time while recording the CARS signal in argon, a non-resonant gas. CARS signal intensity at each probe delay was summed over all frequencies, and the results are shown in Fig. 2.8. Panels (A) and (C) of this illustrate the measured pulse in the time domain as well as a Gaussian fit to the measured time profile. Panels (B) and (D) represent the pulse in the frequency domain obtained through Fourier transforms of the corresponding experimental data and the Gaussian fit to the pulse in the frequency domain. The transformation was performed using a discrete Fourier transform function in MATLAB.

Quantitatively, a probe pulse duration of 3.61 ps yielded a bandwidth of 4.06 cm^{-1}, whereas a probe pulse duration of 5.03 ps resulted in a bandwidth of 2.92 cm^{-1}. These results highlight the flexibility of the SHBC in terms of adjusting the pulse duration and spectral resolution to optimize the generation of CARS signals.

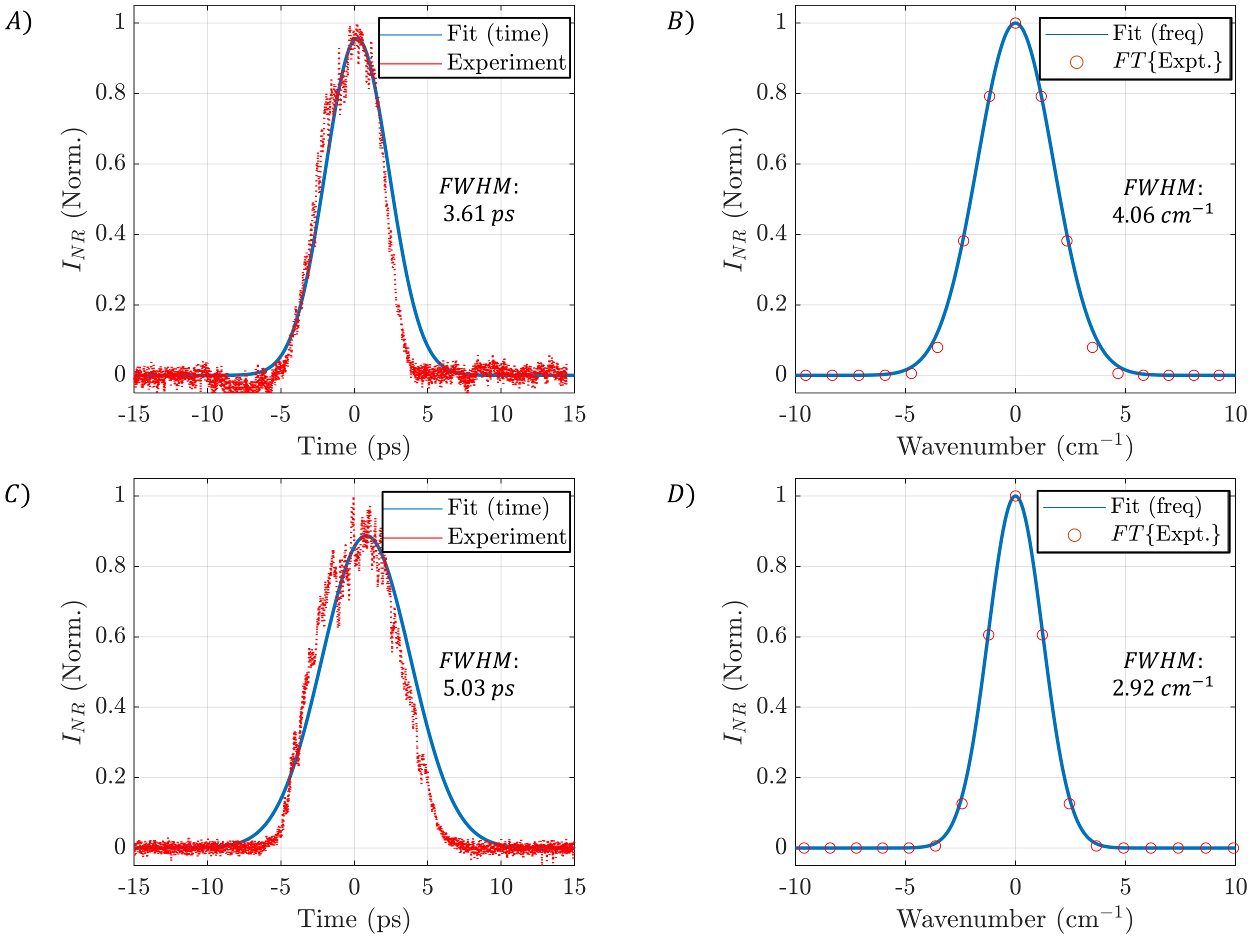

Figure 2.8: A) and C) show experimentally measured time profiles of the SHBC output at two different stretcher positions along with a Gaussian fit, and B) and D) show the Fourier transform of the measured time profile in panels A and C (respectively) showing the bandwidth in frequency.

2.4 CARS Spectral Modeling

A CARS spectral model is essential for determining experimental thermodynamic quantities from measured CARS spectra. An overview of the general theory employed in the CARS spectral model is provided here, while more details can be found in prior literature [58, 59]. Some of the equations included next will be referenced later on in Chapter 5.

The CARS signal intensity, denoted as $I_{CARS}(\omega)$, is proportional to the square of the polarization field [60]:

$$I_{CARS}(\omega) \propto \left|P^{(3)}_{res}(\omega) + P^{(3)}_{nonres}(\omega)\right|^2 \tag{2.4}$$

The nonresonant polarization, $P^{(3)}_{nonres}(\omega)$, can be neglected when experimentally delaying the probe pulse in time relative to the Stokes and pump pulses [31, 54]. The resonant polarization, $P^{(3)}_{res}(t)$, is given by the equation:

$$P^{(3)}_{res}(t) = \left(\frac{i}{\hbar}\right)^3 E_3(t) \int_0^\infty dt_2[R_4(t_2)E_2^*(t+\tau_{23}-t_2)E_1(t+\tau_{23}+\tau_{12}-t_2)exp[i(\omega_1-\omega_2)t]] \tag{2.5}$$

Here, E_1, E_2, and E_3 refer to the electric fields of the pump, Stokes, and probe, respectively. τ_{12} represents the delay between the pump and Stokes pulses (a zero delay is used for the current experiments), and τ_{23} is the delay between the probe and Stokes pulses. The molecular response function, $R_4(t)$, is formulated according to Ref. [31] by neglecting coherent line mixing:

$$R_4(t) = \sum_v \sum_J I_{i\to f} \exp\left[\frac{t}{\hbar}\left(i\Delta E_{i\to f} - \frac{1}{2}\Gamma_{i\to f}\right)\right] \tag{2.6}$$

In Eq. 2.6, v and J represent the vibrational and rotational quantum numbers, respectively. $I_{i\to f}$ represents the transition intensity, $\Delta E_{i\to f}$ is the transition frequency, and $\Gamma_{i\to f}$ is the transition linewidth. The spectral line positions, corresponding to the Raman transition frequencies of the molecule, can be calculated for Q-branch transitions ($\Delta v = 1, \Delta J = 0$) by computing the change in molecular rovibrational energy between the involved states:

$$\Delta E_{i\to f} = E_{v+1,J} - E_{v,J}. \tag{2.7}$$

Raman transition intensities are given by

$$I_{i\to f} \propto \Delta\rho(v,J)\frac{\partial\sigma}{\partial\omega}, \tag{2.8}$$

where $\Delta\rho(v, J)$ is the change in population between the states and $\frac{\partial\sigma}{\partial\omega}$ is the Raman cross-section of the molecule, which represents the probability of rotational Raman scattering as a function of the rotational quantum number [61]. For Q-branch transitions, the Raman cross-section can be calculated using the formulation in Eq. 2.9 provided by Marrocco et al. [62]:

$$\frac{\partial\sigma}{\partial\omega} \propto (v+1)\left(a'^2 F_{iso}(J) + \frac{4}{45} b_{J,J'} \gamma'^2 F_{aniso}(J)\right). \tag{2.9}$$

The Herman-Wallis factors, $F(J)$, in Eq. 2.9, can be calculated using the Tipping-Buanich formulation provided by Marrocco et al. [62]:

$$F(J) = 1 - \left(\frac{3(a_1+1)}{2} - 4\frac{p_2}{p_1}\right)\left(\frac{B_e}{\omega_e}\right)^2 J(J+1). \tag{2.10}$$

The constants B_e, ω_e, and a_1 must be tabulated or experimentally derived. F_{iso} and F_{aniso} are calculated using either the isotropic or anisotropic polarizability (p_1 and p_2). The Placzek-Teller coefficients, $b_{J,J'}$, for Q-branch transitions can be calculated according to Placzek [63] and Gaufres [64]:

$$b_{J,J'} = \frac{J(J+1)}{(2J+3)(2J-1)}. \tag{2.11}$$

2.5 CARS Spectral Fitting

The spectral fitting method employed to determine temperatures from the CARS spectra acquired in the experiment described in Chapter 5 of this thesis is discussed in this section. The temperatures were determined by comparing experimental spectra with a library of theoretically modeled spectra using a differential evolutionary (DE) algorithm, as described in Ref. [65, 66].

As discovered during the current thesis, it is essential to account for shot-to-shot fluctuations in the experimental frequency axis to accurately fit the CARS spectra for temperature. Figure 2.9 presents an example of these fluctuations. The figure displays multiple CARS spectra acquired at a rate of 1 kHz within a single data set for the experiment described in Chapter 4. The observed variations in spectral line positions can be attributed to slight changes in the angle of CARS signal generation, which result from beam steering in turbulent environments.

The turbulence time scale in the experiment is given by the Kolmogorov time scale given by:

$$\tau_\eta = \sqrt{\frac{\nu}{\epsilon}}, \tag{2.12}$$

where

$$\epsilon = u^4/\Lambda. \tag{2.13}$$

Here, ν is the kinematic viscosity of the fluid, u is the root-mean-square velocity, and Λ is the integral length scale. For the facility used in this experiment, $\nu = 4.5 \times 10^{-5}$ m^2/s, $u \approx 50$ m/s, and $\Lambda = 5$ mm [52, 67]. The calculated Kolmogorov time scale using these values is $\tau_\eta = 1.9 \times 10^{-7}$ s.

The data in this experiment was acquired 1 kHz, meaning CARS spectra were acquired every millisecond. Thus, it can be concluded that the the shot-to-shot fluctuations in the data could be due to beam steering in the turbulent environment. This effect is made more severe by the long propagation distances between the measurement volume and the spectrometer and camera system, as is the case in Chapter 4.

To ensure accurate temperature measurements from CARS data, the shifts in the frequency axis observed between frames must be accounted for, as these shifts are not caused by changes in gas temperature. Fig. 2.10 includes several simulated N_2 Q-branch CARS spectra for the range of temperatures observed in the combustion tunnel.

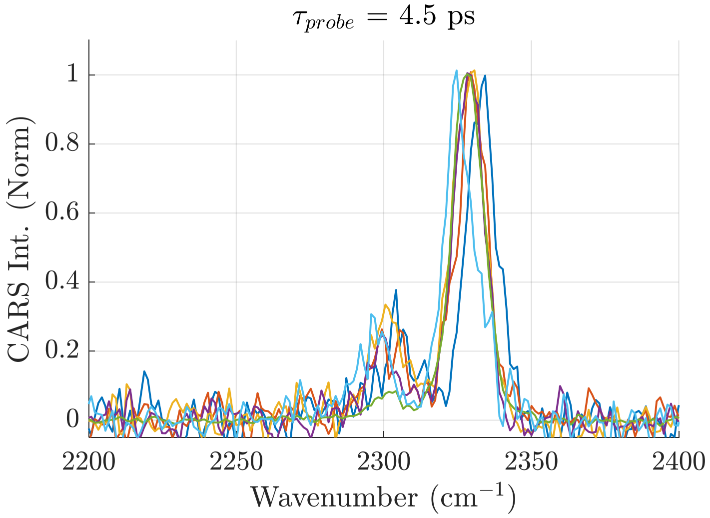

Figure 2.9: Sample CARS spectra showing shot-to-shot fluctuations in line positions.

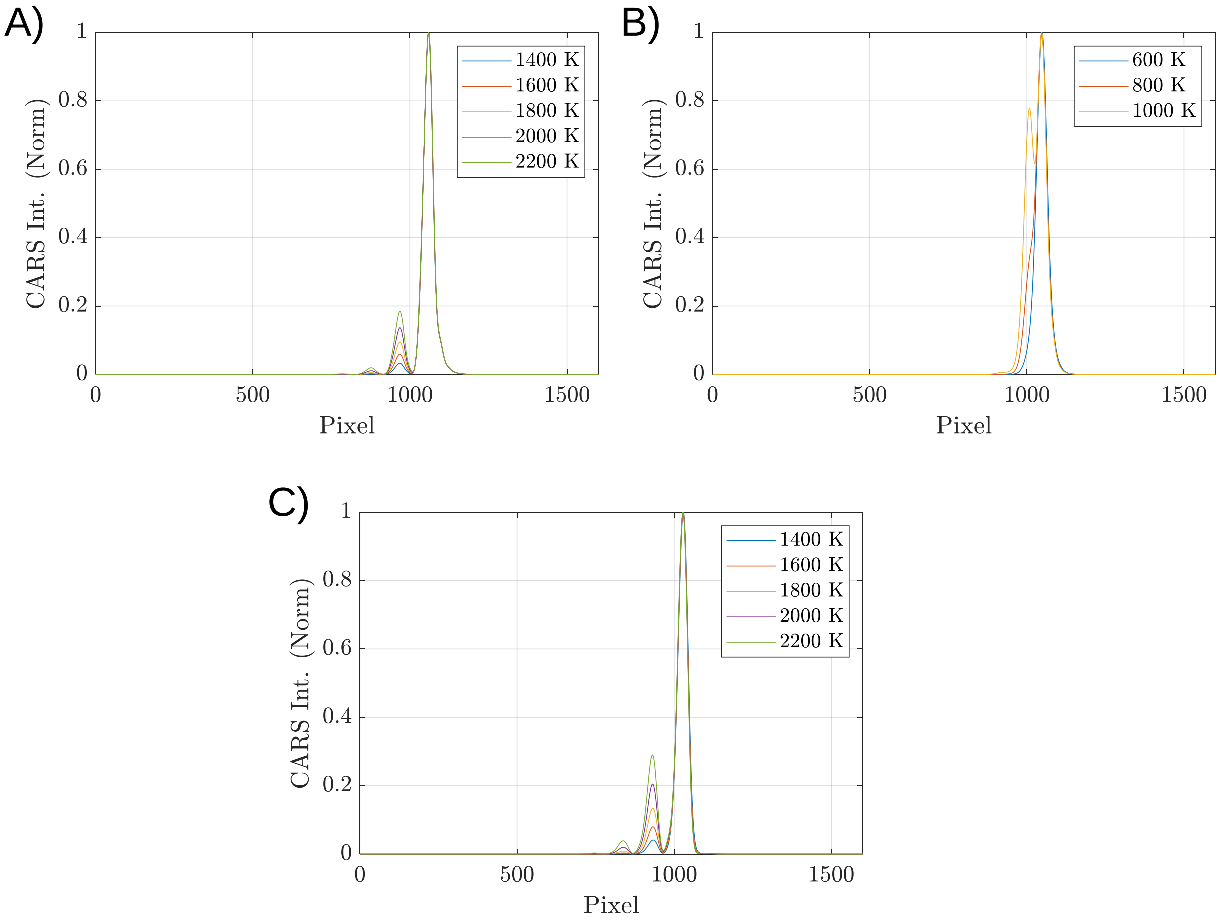

Figure 2.10: Simulated CARS spectra at the three probe delays used in the current thesis. A) 4.5 ps. B) 32 ps. C) 42 ps.

In order to match the experimental spectra, the simulated CARS spectra were downsampled to 1600 points (the amount of pixels in the experimental wavelength axis of the CARS spectra shown in Chapter 4), and the shift in the pixel corresponding to the maximum CARS signal intensity was computed for each frame. The spectra were generated at three probe delays used in the experiment in order to confirm that the frequency shifts observed in the experimental data were not due to temperature effects.

Table 2.1 displays the pixel corresponding to the maximum CARS intensity for the experimental wavelength axis for the spectra recorded in Chapter 4. This pixel is reported at various temperatures for each probe delay. For example, for a probe delay of 4.5 ps and at T = 1400 K and T = 1600 K, the pixel corresponding to the maximum CARS signal intensity is 1059. For T = 1800 K, 2000 K, and 2200 K, the pixel corresponding to maximum CARS signal intensity was 1060.

Table 2.1: Pixel corresponding to the maximum CARS signal intensity at various temperatures and ps probe delays.

T (K)	Pixel (4.5 ps)
1400 K	1059
1600 K	1059
1800 K	1060
2000 K	1060
2200 K	1060
T (K)	**Pixel (32 ps)**
600 K	1048
800 K	1047
1100 K	1047
T (K)	**Pixel (42 ps)**
1400 K	1029
1600 K	1029
1800 K	1028
2000 K	1028
2200 K	1028

As depicted in Fig. 2.10 and shown in Table 2.1, the maximum pixel shift related to temperature is 1 pixel. This is true for all three probe delays. This confirms that the large shifts observed between frames are not temperature-related. Thus, the observed changes in frequency between spectra are due to an experimental effect such as beam steering and must be accounted for to accurately quantify temperature.

Two methods were investigated to address the shift in line position between frames. The first method employed a non-linear least squares (NLLSQ) fitting routine implemented in MATLAB to offset the experimental spectra in frequency to match the simulated CARS spectra positions. This method will be referred to as “Method A”. This approach was computationally expensive, as 10,000 frames were acquired at each measurement location, and each frame took approximately 1 to 15 seconds to fit.

As an alternative, a faster approach was investigated, which involved shifting each experimental spectrum to match the maximum intensity pixel for each frame. In MATLAB, the index of the maximum value in the experimental CARS spectra was determined, and then the entire array was shifted to ensure that the maximum value resided at the same index for each frame. This method, referred to as “Method B”, was much less time intensive and took ∼2 seconds for each data set. To demonstrate the application of Method B, the spectra shown in Fig. 2.9 were processed and the results of Method B are presented in Fig. 2.11.

Fig. 2.12(A) presents a scatter plot that compares the pixel shift calculated for each frame with the resulting temperature fit obtained from the DE algorithm. As evident from the figure, the frequency shift observed is not correlated with the temperature, confirming that correcting the experimental spectra by shifting them to match simulations will not lead to inaccurate temperature fits.

In Fig. 2.12(B) the horizontal axis is given by the magnitude of the pixel shift calculated by Method B for the frame. The vertical axis is given by the difference in the temperature fit with and without the shift determined by Method B. It can be observed that as the magnitude of the shift increases, the error in the temperature fit also increases. Specifically, when no shift is required, the same temperature is obtained regardless of the correction. When a positive pixel shift is necessary, failing to correct for the shift results in a significant

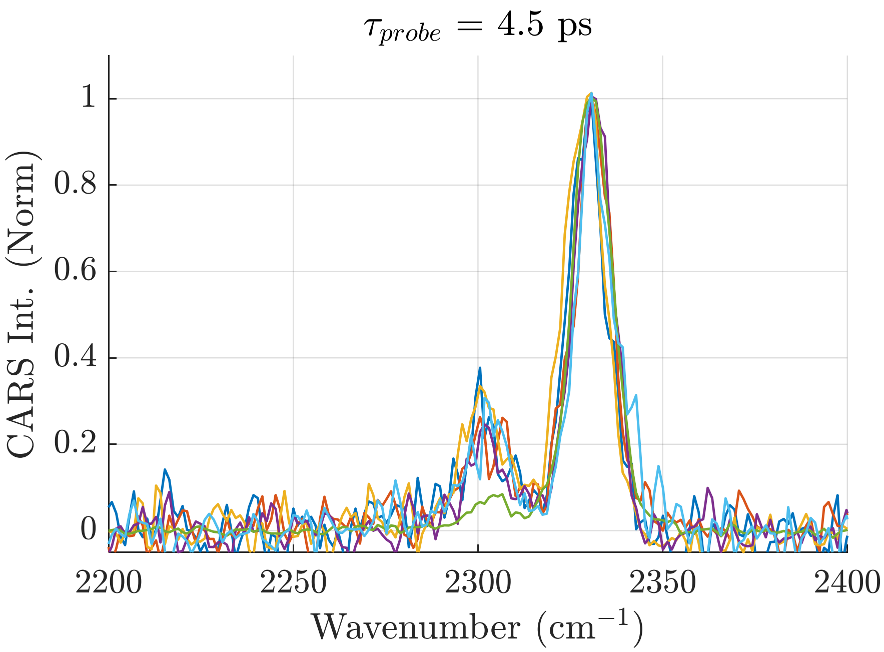

Figure 2.11: Line positions corrected with Method B.

overestimate of the temperature. Conversely, when a negative shift is required, not applying the correction leads to an underestimation of the temperature.

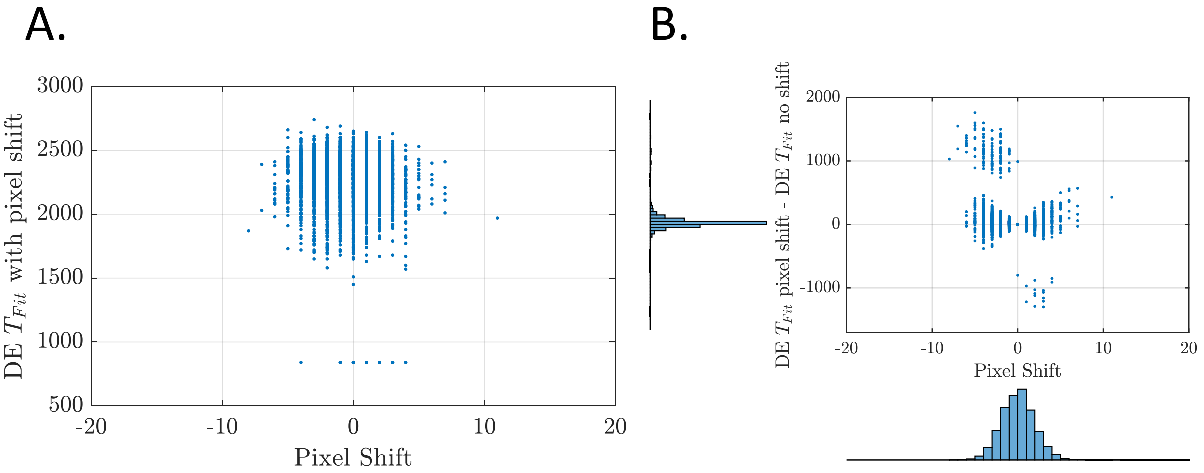

Figure 2.12: A) Scatter plot of fit temperature compared to the magnitude of shift computed using Method B. B) Scatter plot showing the difference between the fit temperature with and without correcting for the shift as a function of the shift magnitude.

Fig. 2.13(A) displays a scatter plot comparing the temperature fits obtained when the shift is corrected for using Method B versus when the shift is not applied. Without the shift correction, many frames tend to fit to the edge of the library in the DE algorithm, indicating a significant mismatch in the frequency axis between the experiment and the simulation. When the shift is applied, the number of frames fitting to the library edge decreases significantly, and the frames that still fit to the library edge can be removed to compute average fit temperatures and standard deviations. Additionally, the spread of fit temperatures away from the red line shown in Fig. 2.13(A) is consistent with the finding that the fit temperatures derived from frames without the correcting the shift in the experimental frequency axis leads to significant errors in fit temperatures.

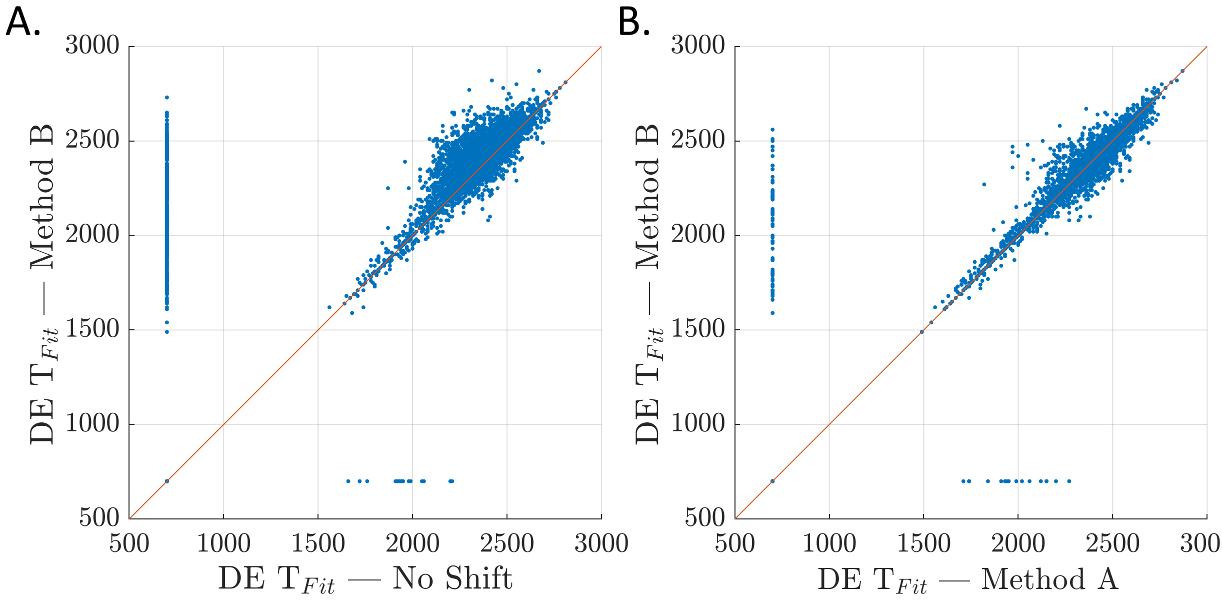

Figure 2.13: A) Correlation plot comparing the fit temperature for each frame with and without correcting for frequency shift. B) Correlation plot comparing the fit temperature obtained using Method A vs. Method B.

Fig. 2.13(B) presents a scatter plot comparing the temperature fits resulting from Method A and Method B. In general, Method B resulted in fewer frames fitting to the library edge compared to Method A. However, a comparison of the temperature fits obtained using the shifts computed with Method A and the Method B (shown in Fig. 2.14 and Fig. 2.15) reveals that the methods can at times yield different shift values for the same frame. This is evident as not all fit temperatures fall along the red line shown in Fig. 2.15(B). These disparities in the shift calculation between the two methods contribute to the differences observed in the resulting temperature fits from the DE algorithm in Fig. 2.13(B).

In Fig. 2.14, Method A failed to properly shift the spectrum, resulting in an inaccurate temperature fit at the library edge. Conversely, Method B corrected for the shift correctly and provided a reasonable fit temperature. However, Method B is not without error and can be affected more significantly by noise at the CARS bandhead, as observed in Fig. 2.15. Method A accurately fit the frequency shift for this particular spectrum, while Method B did not due to the presence of noise at the bandhead. This highlights the fact that neither method is perfect, and further work is needed to account for frequency axis shifting when using the DE algorithm to fit CARS spectra.

For the purposes of this thesis, Method B was chosen to fit temperatures due to its time efficiency compared to Method A. Additionally, Method B was better at reducing the number of frames fitting to the library edge, which was often caused by significant discrepancies in the frequency axis, as shown in Fig. 2.14.

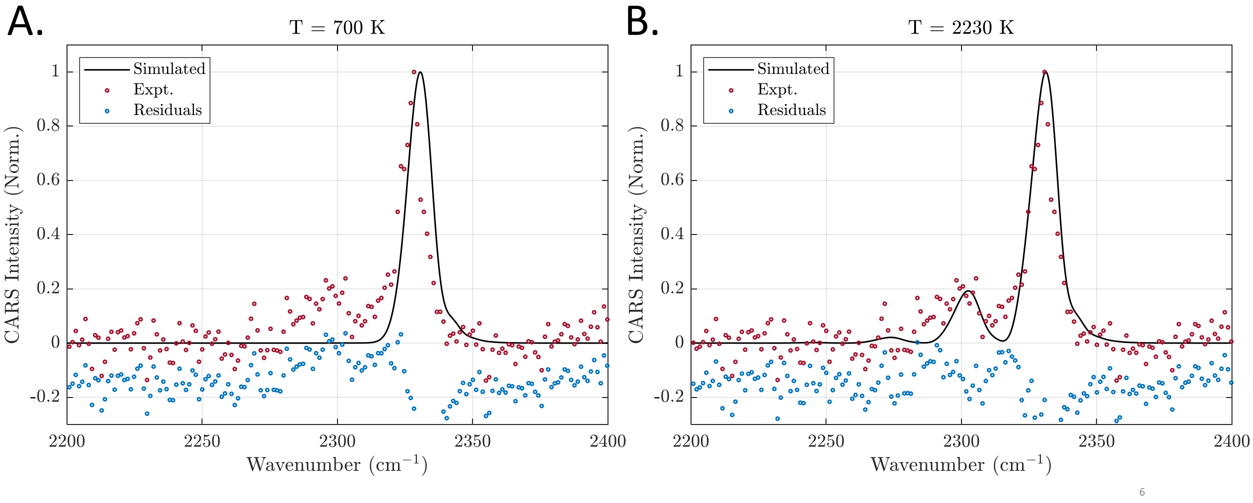

Figure 2.14: Comparison of fit temperatures resulting from Method A (NLLSQ) vs. Method B. Data was taken in Case 1 at position 6.1 with a probe delay of 4.5 ps.

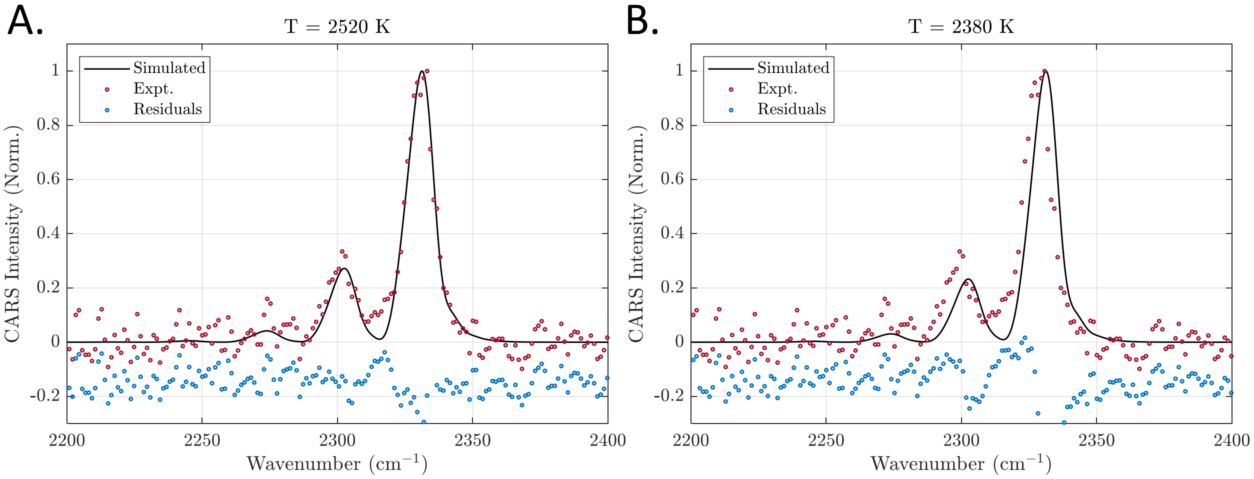

Figure 2.15: Additional comparison of fit temperatures resulting from the Method A (NLLSQ) vs. Method B. Data was taken in Case 1 at position 6.1 with a probe delay of 4.5 ps.

Chapter 3

Counter-propagating fs/ps CARS

The work presented in this chapter is currently in preparation for journal submission. A modified version with extended discussion is included in this chapter.

3.1 Motivation and Objectives

As noted in Chapter 1, improvement in CARS spatial resolution is necessary in order to investigate reacting flows with small characteristic spatial scales while avoiding spatial averaging effects. The use of a counter-propagating phase-matching configuration with two counter-propagating fs pulses has the potential to enable spatial resolution on the order of ∼10 µm due to the fact that the length of CARS measurement volume would be limited to the width of the pulses in time (60 fs in the current work). This experimental set up would allow for ultra-high spatial resolution even when limited optical access is available in test facilities.

A schematic of the phase matching scheme for rotational counter-propagating fs/ps CARS is shown in Fig. 3.1. The use of counter-propagating phase matching allows for a compact experimental setup as there is no need to drastically increase the crossing angle to achieve microscale resolution. While no angle is necessary to satisfy phase matching, a 6° crossing angle was chosen in this experiment to allow for spatial separation of the CARS signal from the pump, Stokes, and probe beams.

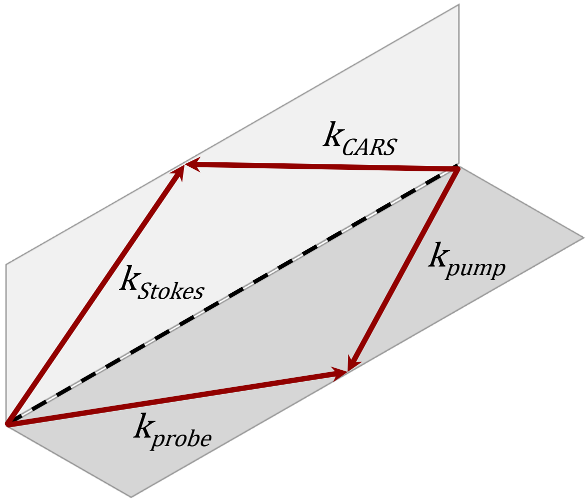

Figure 3.1: Folded BOXCARS phase matching scheme for the counter-propagating fs/ps CARS set up.

The objective of this experiment is threefold. Firstly, it aims to quantify the spatial resolution of the fs/ps CARS system with a counter-propagating phase-matching configuration. This characterization is crucial for understanding the precision and accuracy of the measurement technique.Secondly, the experiment aims to demonstrate the capability of the fs/ps CARS system with counter-propagating phase matching to quantify the small-scale temperature gradients generated by a sonic gas jet originating from a microscale hypodermic needle. By utilizing the counter-propagating phase matching, it is possible to obtain temperature information with high spatial resolution, enabling the investigation of microscale phenomena. Thirdly, the experiment demonstrates an additional feature of the counter-propagating phase-matching configuration, namely the ability to translate the location of the measurement volume by adjusting only the temporal overlap of the fs pulses.

These objectives collectively highlight the potential and versatility of counter-propagating fs/ps CARS system in quantifying temperature gradients with high spatial resolution.

3.2 Experimental Setup

3.2.1 Optical Layout

A diagram illustrating the optical layout utilized in the counter-propagating experiment is depicted in Fig. 3.2. The experimental setup uses a Coherent Astrella laser system operating at a wavelength of 800 nm with a pulse duration of 60 fs and a repetition rate of 1 kHz. The output from a post-amplification pulse compressor was initially split into two parts using an 80/20 beamsplitter. The majority of the laser energy was directed towards a 4f-pulse shaper, which was employed to generate a narrowband picosecond probe beam. The remaining portion of the laser beam was directed through a 50/50 beamsplitter to generate the pump and Stokes beams.

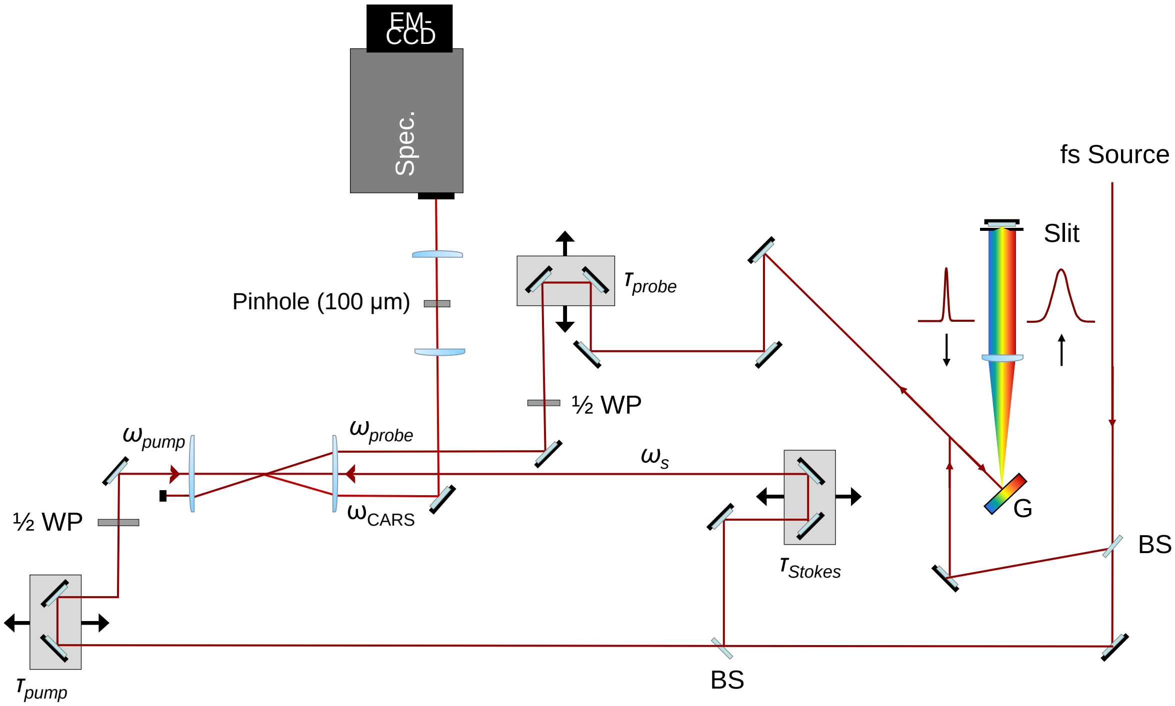

Figure 3.2: Schematic of the optical layout used in the counter-propagating CARS experiment.

To ensure the temporal overlap of the pump and Stokes pulses in the measurement region, each beam passed through an optical delay line mounted on a micrometer stage. This setup allowed for precise adjustment of the relative delay between the pulses.

Half-waveplates were included in each beam path in order to optimize the generation of coherent anti-Stokes Raman scattering (CARS) signals. These waveplates allowed for the manipulation of the polarization of the pump and Stokes beams to maximize the efficiency of CARS signal generation.

An image depicting the counter-propagating CARS setup is presented in Fig. 3.3. The optical layout involved directing two femtosecond (fs) pulses, namely the Stokes and pump beams, in opposing directions toward the measurement volume. To achieve this, two lenses with a focal length of 300 mm were positioned 600 mm apart. Both beams passing through these lenses were focused to the same location at the center of the lenses. The lens responsible for focusing the Stokes and probe beams is referred to as ”Lens A”, while the lens directing the pump beam is called ”Lens B”.

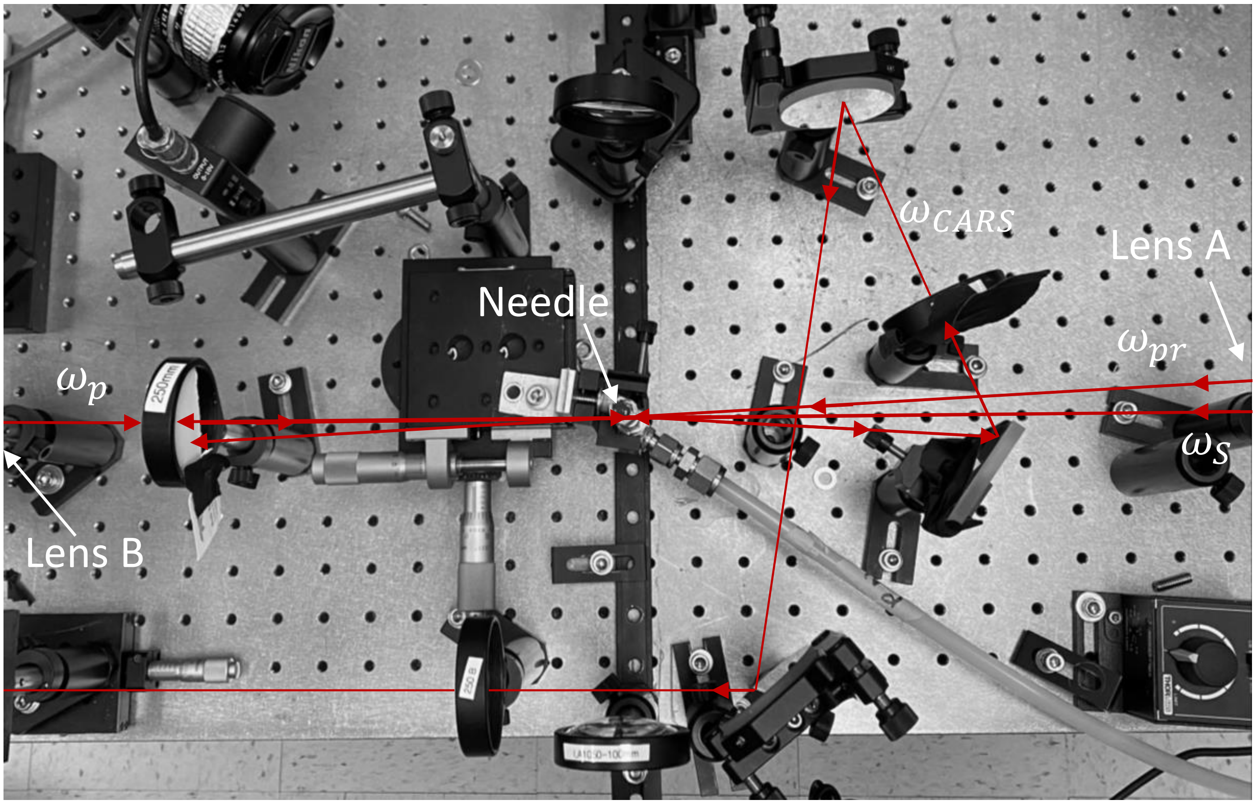

Figure 3.3: Photograph of the optical layout used in the counter-propagating CARS experiment with beam paths added.

The rotational CARS signal generated in the measurement volume was then redirected to a third lens using a square mirror to collimate the signal. This mirror was positioned between Lens A and the gas jet, as shown in Fig. 3.3. The collimated CARS signal was then directed to a spatial filter consisting of two lenses and a 100 µm pinhole. This spatial filter helped eliminate excess laser scatter before the signal was directed into a spectrometer (Princeton Instruments, SCT 320) and an electron-multiplied charge-coupled device (EM-CCD) camera (Princeton Instruments, ProEM 1600 eXcelon 3) for detection.

The pulse width in the time domain of the two fs pulses were adjusted using a post-amplification pulse compressor, and its duration was measured using a custom GRENOUILLE system [68]. The post-amplification pulse compressor, provided by the laser manufacturer (Coherent), was employed after the chirped pulse amplifier to compress the pulse back to its original duration of 60 fs, which is the output pulse duration from the laser.

In this experiment, the post-amplification pulse compressor was utilized to adjust the actual pulse compression from 60 fs to 300 fs to investigate the effect of pulse duration on the size of the measurement volume. The beam energies used for the various pulse durations in the experiment are listed in Table 3.1.

Table 3.1: Beam energies used in the experiment for each pulse duration.

Pulse Duration (fs)	Pump and Stokes (µJ)	Probe (µJ)
60	67	18.6
100	166	18.6
150	204	18.6
200	186	18.6
300	268	18.6

3.2.2 Microscale Gas Jet

In the experiment, a microscale gas jet of air traveling at sonic velocities was employed to test the measurement resolution of the counter-propagating fs/ps CARS setup. A compressed air source and a 34-gauge hypodermic needle (Hamilton Company) with an inner diameter of 51 µm were used to create a steep temperature gradient for testing the capabilities of the counter-propagating fs/ps CARS system. The needle was translated in steps of 5 µm into the stationary measurement region, and CARS spectra were acquired at each jet position to measure the temperature. The pulse duration used was 60 fs. The air for the gas jet was supplied from an air compressor, and the gas flow rate was controlled using a mass flow controller. The air pressure upstream of the mass flow controller was measured to be 50 psig.

Fanno flow assumptions were used to estimate the expected temperature of the air jet for comparison with the CARS measurements. Assuming a calorically perfect gas, adiabatic flow, constant area nozzle, one-dimensional steady flow, and a sonic condition at the exit of the needle, the temperature of the air leaving the needle was estimated using

$$\frac{T}{T^{\star}} = \frac{\gamma + 1}{2 + (\gamma - 1)M^2} \tag{3.1}$$

where temperature at the exit is denoted as $T^{\star}$. Here, γ represents the ratio of specific heats for air, known to be $\gamma = 1.4$. The air pressure after the mass flow controller, p_1, was approximated to be 50 psig, the pressure at the inlet of the mass flow controller. The pressure at the exit of the needle, p_2, was assumed to be atmospheric. The temperature of the gas before the needle was assumed to be $T_1 = 293$ K.

The gas velocity before the needle was approximated using the mass flow rate measured by the mass flow controller, which was 0.3 standard liters per minute (SLPM). The gas velocity at the needle inlet was calculated assuming one-dimensional, incompressible flow:

$$\dot{m} = \rho u A, \tag{3.2}$$

where $\dot{m}$ is the mass flow rate, ρ is the gas density, u is the gas velocity, and A is the cross-sectional area of the duct. The area of the duct was calculated assuming a constant area (no deformities in the needle) and using the inner diameter of the needle, 51 µm. The

Mach number, denoted as M, was calculated using a perfect gas assumption for the speed of sound:

$$u_{\text{sound}} = \sqrt{\frac{\gamma RT}{\text{Mass}}}, \tag{3.3}$$

and the definition of Mach number:

$$M_i = \frac{u_i}{u_{\text{sound}}}, \tag{3.4}$$

where M_i is the Mach number and u_i is the gas velocity. The calculated Mach number at the inlet of the needle, M_1, was found to be 0.44. Using this information, along with the previously mentioned input conditions and assumptions, the estimated temperature of the gas jet at the exit of the needle, as given by Eq. 3.1, was determined to be 254.6 K.

3.2.3 Schlieren Imaging of the Microscale Gas Jet

The width of the gas jet was estimated using Schlieren imaging to visualize the jet at the exit of the hypodermic needle. In this setup, helium gas was used to visualize the density changes between the gas jet and the surrounding air. The optical layout of the Schlieren imaging system is shown in Fig. 3.4, which is a "Z-type" Schlieren setup.

The system consisted of a mounted point source that emitted an 840-mW white LED. The light from the point source was collimated by a concave mirror placed $1f$ away from the source. The collimated light was then reflected towards a second concave mirror placed $2f$ away from the first mirror. The gas jet was positioned between these two mirrors, within the path of the collimated light. Density changes in the gas jet caused bending of the collimated light, which could be observed and recorded. A knife edge was inserted at the focal point of the second mirror to obstruct half of the incoming light, allowing for better visualization of

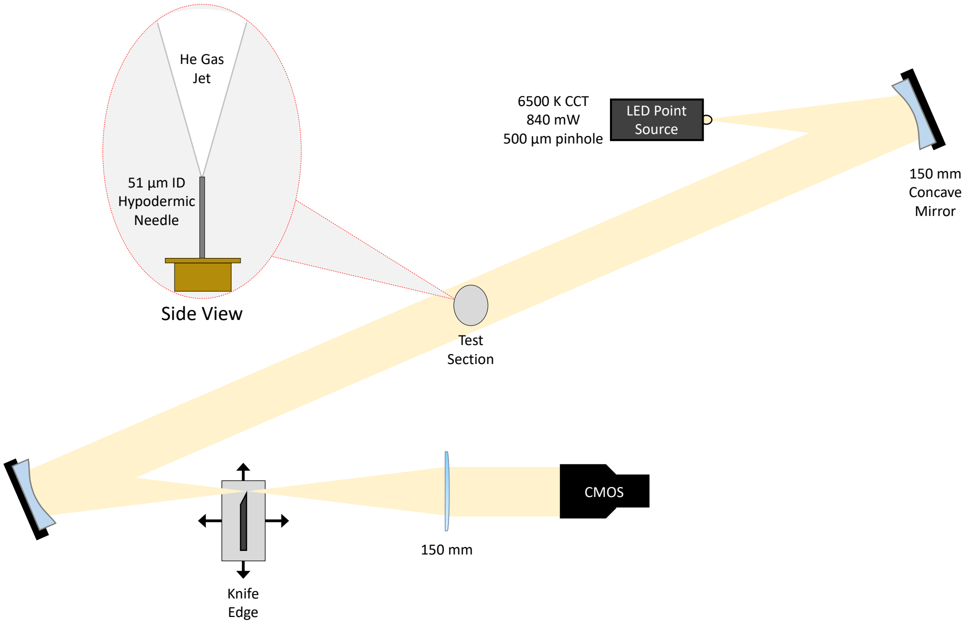

Figure 3.4: Schematic of the optical layout of the Schlieren imaging system used to visualize the gas jet at the exit of the hypodermic needle.

the density changes. The remaining light was collimated by a 150 mm spherical lens, and the image was recorded using a CMOS image sensor.

A Schlieren image of the gas jet is shown in Fig. 3.5. To estimate the width of the gas jet, the Schlieren image was reconstructed assuming axial symmetry and using an inverse Abel transform [69]. The inverse Abel transform is an integral transform used to analyze axisymmetric functions and can be used to calculate an axisymmetric function from a projection such as a photograph. The density profile of the gas jet as a function of radial distance from the core of the jet, denoted as $f(r)$, can be obtained using the inverse Abel transform integral:

$$f(r) = -\frac{1}{\pi}\int_r^\infty \frac{dF}{dy}\frac{dy}{\sqrt{y^2 - r^2}}. \tag{3.5}$$

The Abel reconstruction of the gas jet is shown in Fig. 3.6. Based on the Abel reconstruction, the FWHM of the density profile of the gas jet at the plane of measurement was estimated to be 84 µm.

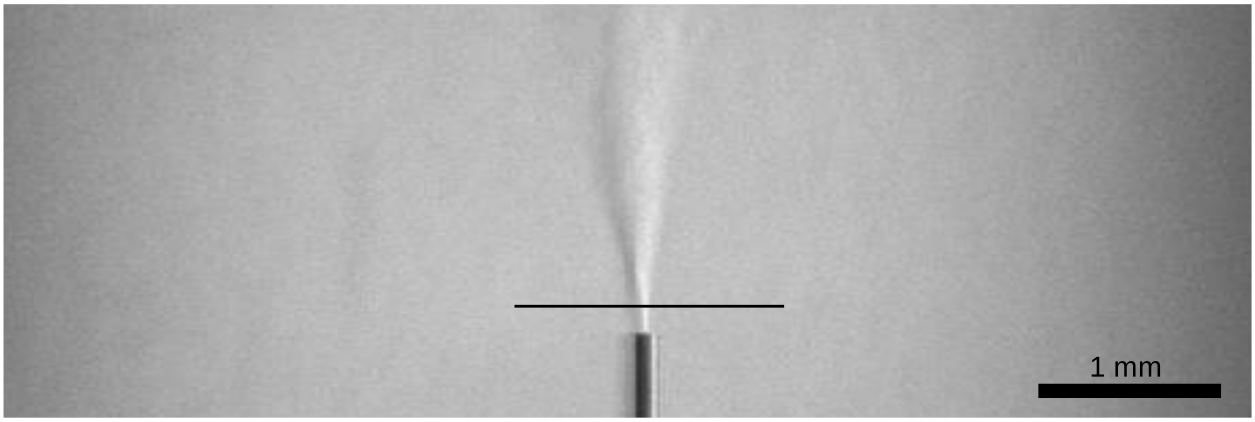

Figure 3.5: Schlieren image of the microscale gas jet.

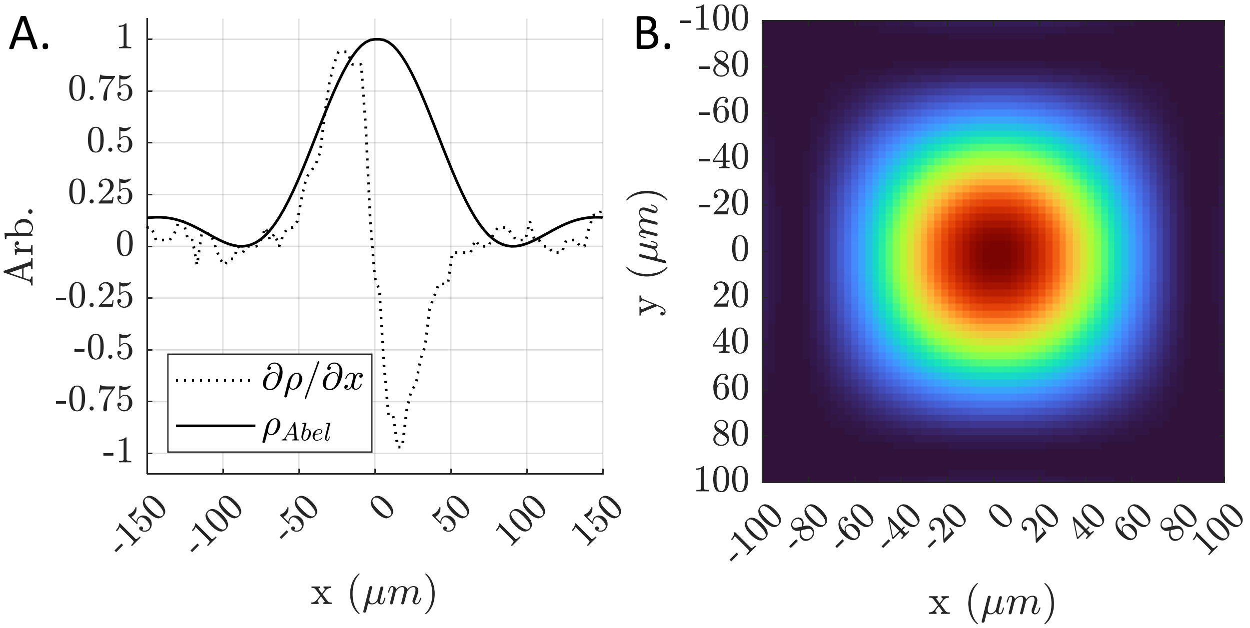

Figure 3.6: A) Abel inversion of the Schlieren image. B) Reconstruction of gas jet from Abel inversion.

It is important to note that helium was used to visualize the gas jet, and thus a direct comparison between the Schlieren measurements and the CARS measurements may not be exact due to differences in the ratio of specific heats (γ) between air and helium. Additionally, Schlieren is used to determine gas density while CARS is used to measure gas temperature. However, the Schlieren images can be used for relative comparison to validate the measurements obtained with CARS.

3.2.4 Estimated Probe Volume Size

The size of the CARS measurement volume using counter-propagating pulses was estimated by calculating the convolution of two Gaussian pulses in the time domain. The calculations in this section as well as Chapter 3.2.5 were performed by a colleague and partner on the project, Ryan Thompson. The analysis is included here to give context to the results shown in this chapter.

The time- and space-dependence of the pump and Stokes pulses can be represented as $E_1(x - ct)$ and $E_2(x + ct)$, where the pump pulse is traveling in the positive x-direction and the Stokes pulse is traveling in the negative x-direction. Making the substitution $\xi = x - ct$, the convolution in time is

$$\begin{aligned}\int_{-\infty}^{\infty} E_2^*(x+ct)E_1(x-ct)t &= \int_{\infty}^{-\infty} E_2^*(2x-\xi)E_1(\xi)(-\xi/c) \\ &= \frac{1}{c}\int_{-\infty}^{\infty} E_2^*(2x-\xi)E_1(\xi)\xi \\ &= \left(E_2^* * E_1\right)(2x). \end{aligned} \tag{3.6}$$

Here, the convolution between the two electric fields E_1 and E_2 that are functions of x is written as $(f * g)(x)$. Assuming the spatial distributions of the pump and Stokes pulses at an instant in time can be represented as Gaussian with standard deviations σ_1 and σ_2, the convolution in Eq. 3.6 can be written as

$$\begin{aligned}
\left(E_2^* * E_1\right)(x) &= \int_{-\infty}^{\infty} \exp\left[-\frac{1}{2}\frac{(x')^2}{\sigma_2^2}\right] \exp\left[-\frac{1}{2}\frac{(x-x')^2}{\sigma_1^2}\right] x' \\
&= \sqrt{\frac{\pi}{a}} \exp\left[-\frac{x^2}{2(\sigma_1^2+\sigma_2^2)}\right], \qquad (3.7)
\end{aligned}$$

where $a = (1/\sigma_1^2 + 1/\sigma_2^2)/2$. Combining the results from Eqs. 3.6 and 3.7 and assuming that $\sigma_1 = \sigma_2$ since the pump and Stokes pulses have the same pulse duration,

$$\begin{aligned}
\left(E_2^* * E_1\right)(2x) &= \sqrt{\frac{\pi}{a}} \exp\left[-\frac{(2x)^2}{2(2\sigma_1^2)}\right] \\
&= \sqrt{\frac{\pi}{a}} \exp\left[-\frac{x^2}{\sigma_1^2}\right] \\
&= \sqrt{\frac{\pi}{a}} \exp\left[-\frac{1}{2}\frac{x^2}{(\sigma_1/\sqrt{2})^2}\right]. \qquad (3.8)
\end{aligned}$$

The convolution is a Gaussian with standard deviation smaller by a factor of $\sqrt{2}$ than the pump and Stokes Gaussian pulses. Thus, the theoretical estimate of probe volume size according to Eq. 3.8 using two counter-propagating 60 fs pulses is 13 µm—orders of magnitude improvement in spatial resolution compared to conventional phase-matching configurations (resolution on the order of 1 mm). Additionally, this implies that the size of the CARS measurement volume can be adjusted by adjusting pulse duration in time by changing the post-amplification pulse compression, as the size of the measurement volume is determined the duration of the pump and Stokes pulses, as dictated by σ in Eq. 3.8.

3.2.5 Measuring Spatial Resolution

The width of the CARS measurement volume was quantified by translating a Borosilicate glass microscope slide (Fisherbrand, 170 µm thick) through the probe volume to measure changes in CARS signal generation in the glass. Due to the flat edge of the glass and the small size of the CARS probe volume, a sharp increase in CARS signal intensity was observed as the glass was translated into the probe volume. Deconvolution of the measured signal intensity and the glass provided an absolute measurement of probe volume size.

A convolution of a Gaussian probe volume $f(x)$ from Eq. 3.8 with a step function $g(x)$ representing the glass is given by

$$\begin{aligned}
(f * g)(x) &= \int_{-\infty}^{\infty} f(x')g(x-x')x' \\
&= \int_{-\infty}^{\infty} \sqrt{\frac{\pi}{a}} \exp\left[-\frac{(x')^2}{\sigma_1^2}\right] g(x-x')x' \\
&= \sqrt{\frac{\pi}{a}} \int_{-\infty}^{x} \exp\left[-\frac{(x')^2}{\sigma_1^2}\right] x' \\
&= \sqrt{\frac{\pi}{a}} \frac{\sigma_1\sqrt{\pi}}{2} \left[\operatorname{erf}\left(\frac{x}{\sigma_1}\right) + 1\right] \\
&= \frac{\pi\Delta x}{4} \sqrt{\frac{1}{a \ln 2}} \left[\operatorname{erf}\left(\frac{2\sqrt{\ln 2}}{\Delta x} x\right) + 1\right]. \qquad (3.9)
\end{aligned}$$

Here, erf is the error function and $\Delta x = 2\sigma_1\sqrt{\ln 2}$ represents the full-width at half-maximum of the Gaussian probe volume profile. Experimental data was fit to Eq. 3.9 and values for the parameter Δx were used in order to derive an estimated probe volume size from the measured convolution.

3.2.6 Adjustment of Probe Volume Location using Temporal Overlap

The flexibility of adjusting the probe volume location was demonstrated by tracking the movement of the probe volume with a flowing gas non-resonant with the CARS process while controlling the temporal overlap of the fs pulses. This was achieved by adjusting the delay stage of the pump beam by a known amount and observing the resulting displacement of the probe volume. The location of the gas jet was adjusted to match the new probe volume location, where the CARS signal intensity would disappear due to the presence of the non-resonant gas. By recording the change in jet position for each offset in time, the corresponding change in the measurement volume locations could be determined.

This capability allows for precise control and manipulation of the measurement volume in space, providing flexibility in targeting specific regions of interest. By adjusting the temporal overlap of the fs pulses, the location of the measurement volume can be translated with high accuracy. This feature enhances the utility of the counter-propagating phase matching technique, enabling targeted measurements in different regions of a sample or allowing for dynamic tracking of spatial changes in a sample over time.

3.3 Results and Discussion

3.3.1 Spatial Resolution

Fig. 3.7 shows the observed CARS signal intensity at different positions of the glass sample. The full width at half maximum (FWHM) of the CARS probe volume, which represents the spatial resolution, can be directly determined from the fit using Eq. 3.9. A range of pulse widths from 60 fs to 300 fs were investigated.

In Fig. 3.8, the measured probe volume sizes for each pulse duration are presented. The values for the probe volume size corresponding to each pulse duration are also provided in Table 3.2. The smallest measured CARS measurement region is 15.52 µm, which was achieved with a pulse duration of 60 fs. This is a significant improvement in spatial resolution compared to previous phase matching configurations, which typically yield spatial resolution on the order of 100 µm or larger. It is worth noting that this enhanced resolution was achieved with a relatively small crossing angle of 6°, which is much smaller than the 33° crossing angle required for sub-100 µm resolution in BOXCARS configurations (as mentioned in Chapter 1). This result highlights the capability of fs/ps CARS with counter-propagating fs pulses to achieve high spatial resolution measurements while overcoming the limitations of previous techniques such as experimental footprint.

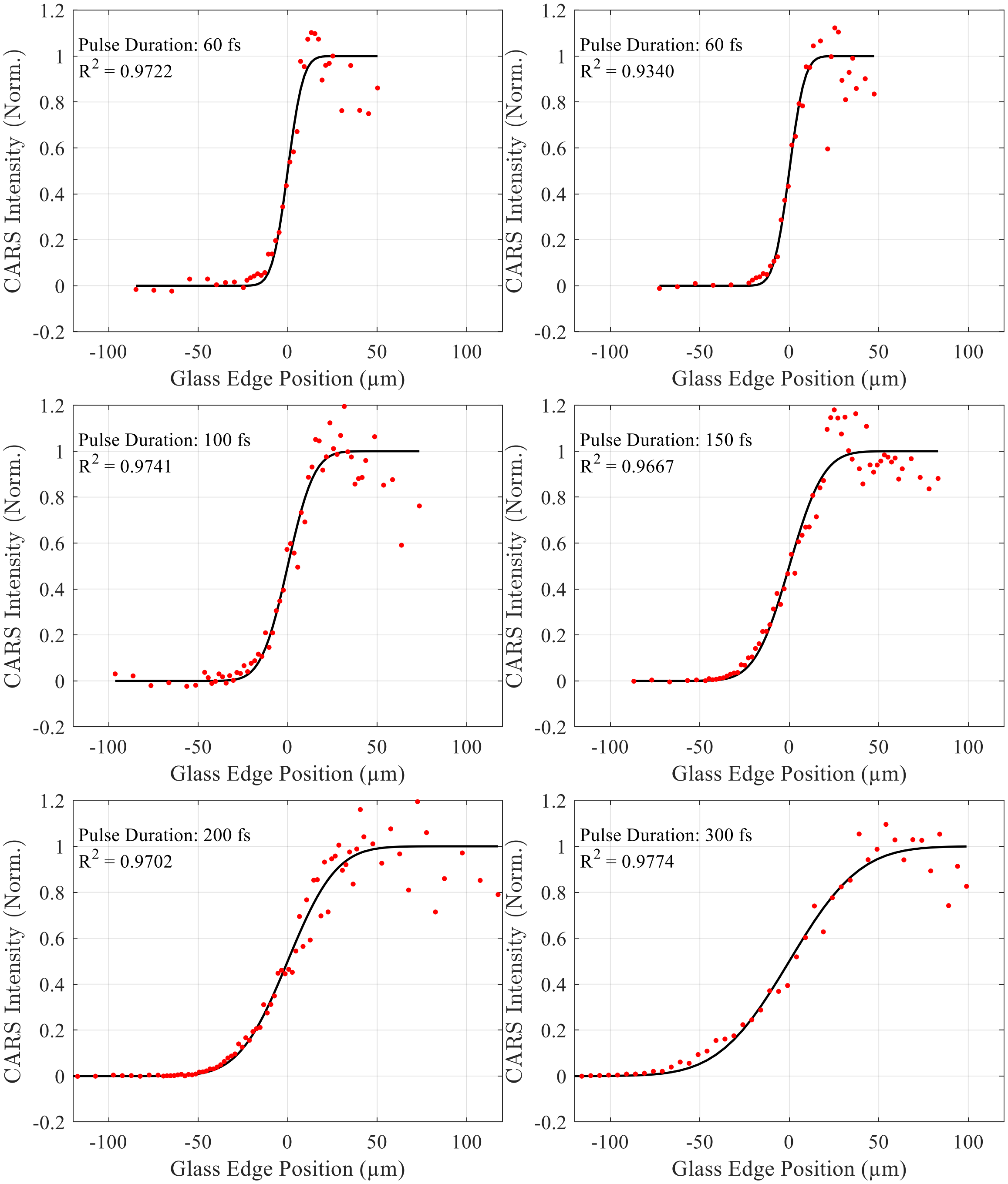

Figure 3.7: CARS signal intensity vs. glass position for various pulse durations.

The two reported probe volume sizes reported for the 60 fs pulse duration were recorded at different beam energies to demonstrate that variations in pulse energy do not lead to variation in the measured probe volume size. The first set, taken with pump and Stokes beam energies of 67 μJ, resulted in a measured probe volume size of 15.52 μm. The second

Table 3.2: Pulse Duration vs. Measured Probe Volume Size

Pulse Duration (fs)	PV Size (µm)
60	15.52, 15.93
100	27.79
150	37.17
200	48.00
300	71.00

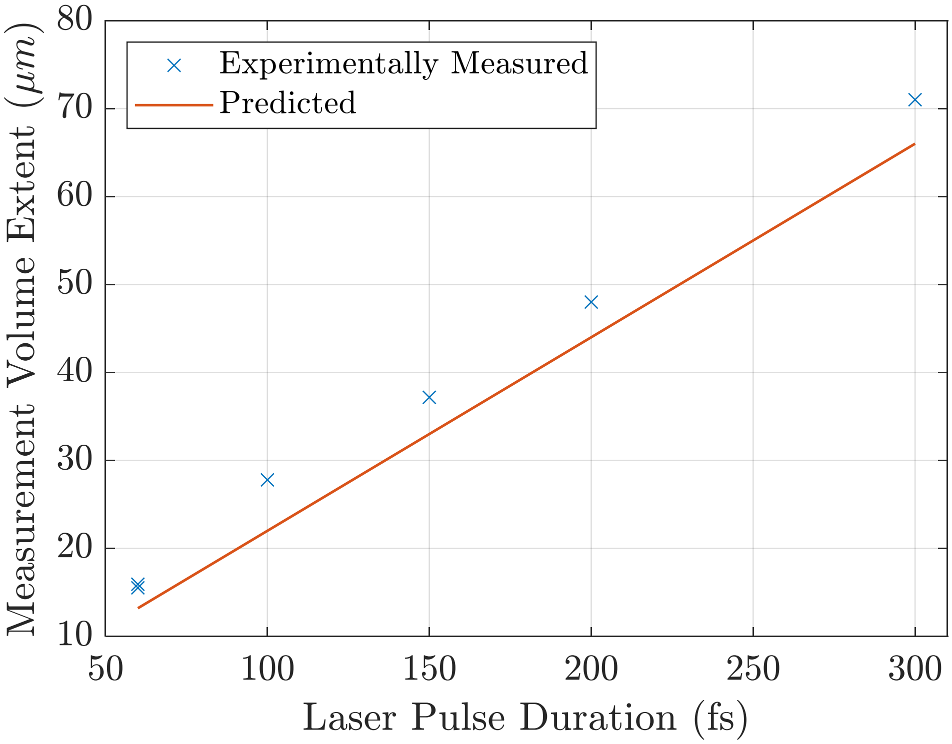

Figure 3.8: Estimated probe volume size vs. pulse duration

set, taken with lower beam energies of 36.3 µJ, yielded a slightly larger measurement of 15.93 µm. This confirms that changes in laser energy do not significantly affect the measured probe volume size, indicating the reliability of the measurement.

In Fig. 3.8, it is observed that the measured probe volume sizes are consistently greater than the predicted values for the given pulse duration. However, the rate at which the spatial resolution changes with pulse duration, as obtained from the experimental data, is in very good agreement with the theoretical prediction. The experimental data shows that the size of the probe volume changes at a rate of 0.21 µm/fs, which closely matches the predicted value of 0.22 μm/fs. The discrepancy between the experimental measurements and the predicted values could be attributed to a couple of factors. One possibility is that the GRENOUILLE system used to measure the pulse width may be miscalibrated, leading to a slight underestimation of the true pulse width. An additional explanation is that the pulses in the GRENOUILLE are different than those at the measurement volume due to the variance in the amount of glass and optical materials that the pulses travel through (lenses, waveplates, etc.). Another explanation could be that the actual pulses are not exactly Gaussian, resulting in deviations from the simulated values. Further investigation is required to determine the source of the discrepancy.

Despite the small difference between the measured and predicted values, the consistency in the rate of spatial resolution change with pulse duration between the experimental and theoretical results confirms the concept that the spatial resolution of CARS can be controlled as desired through post-amplification pulse compression.

3.3.2 Temperature Measurements of a Microscale Gas Jet

Shown in Fig. 3.9 are the measured gas temperatures obtained at various positions across a microscale sonic gas jet using CARS with counter-propagating 60 fs pulses. Here, the temperature reported is the average fit temperature to 300 CARS spectra. The error bars represent the standard deviation of the distribution of temperatures observed in that position. These measurements demonstrate the capability of accurately characterizing the temperature change between the ambient room air and the microscale gas jet.

Since the measurement volume length (∼16 μm) is smaller than the distance over which the temperature gradient spans, counter-propagating phase matching with 60 fs pulses provides the necessary spatial resolution to capture the temperature variations within the jet (66 μm).

Temperatures were extracted from the experimental data via the DE algorithm mentioned in Chapter 2.5 of this thesis. S-branch CARS spectra of air at various temperatures were simulated using a CARS spectral model. The experimental spectra were fit to a library of

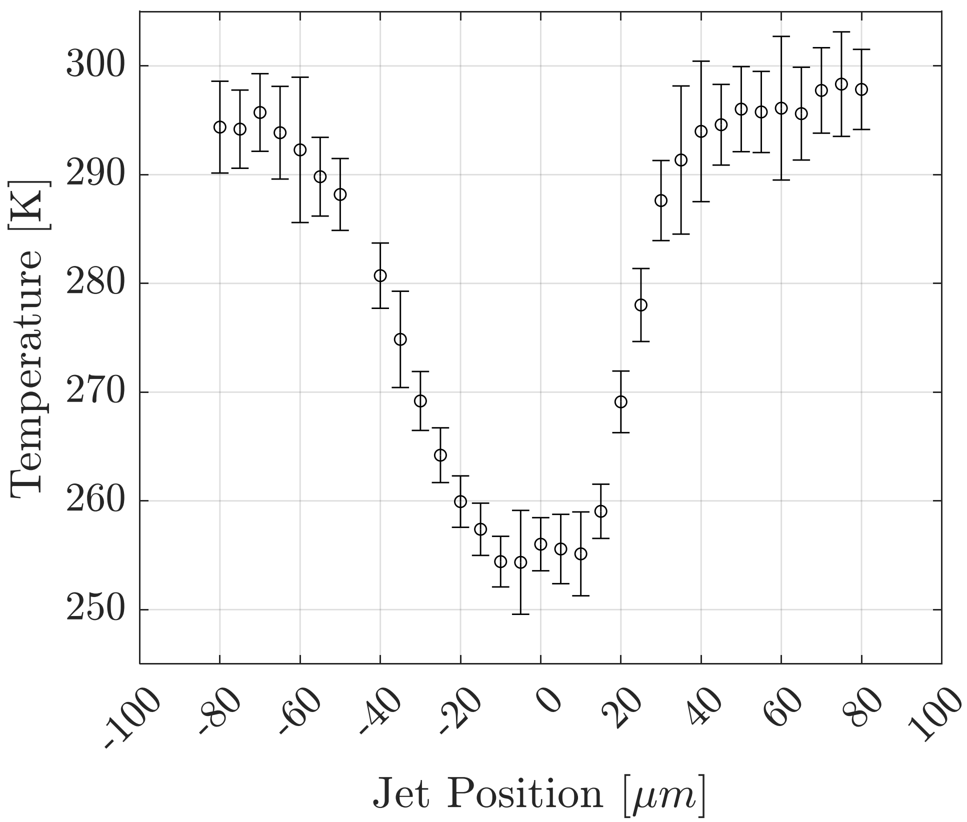

Figure 3.9: Temperature measurements of the cold air jet with 60 fs pulses. Reported temperature is the average fit temperature to 300 shots. Vertical bars represent one standard deviation in temperature in each direction.

simulated CARS spectra for a range of temperatures between 200 K and 400 K. The library generated spectra in steps of 2 K.

Fig. 3.10 show a sample spectral simulation at the best-fit temperature, the averaged experimental CARS spectrum, and the corresponding histogram of fitted temperatures to single frames at different positions within the gas jet. These figures provide insight into the temperature distribution and variations observed in the measurement region. In Fig. 3.10(A), corresponding to a jet position of $\Delta x = -65$ µm outside of the gas jet, shows a sample temperature fit to a single spectrum acquired at this jet position. The histogram of fitted temperatures displays the distribution of temperature values obtained from multiple measurements at this position. Similarly, Fig. 3.10(B) and Fig. 3.10(C) correspond to jet positions of $\Delta x = -25$ µm and $\Delta x = -5$ µm, respectively. These examples highlight the change in temperature as the core of the jet is translated to fully encapsulate the probe volume. The measured gas temperature steadily decreases as the jet core approaches the measurement region.

The core temperature of the gas jet was found to be 256 K over a region approximately 30 µm long. This observation is consistent with the trends observed in both Fig. 3.9 and the Fanno Flow calculations, which estimated the gas temperature in the jet core to be 254 K.

According to the CARS measurements, the FWHM of the jet is 66 µm. This is smaller than the estimate determined from the Schlieren reconstruction (84 µm). This provides confidence that the temperature measurements are not suffering from spatial averaging, as then the FWHM of the jet would be larger than the width determined from the Schlieren reconstruction.

It is worth noting that the discrepancy between the jet width determined from the Schlieren reconstruction and the measurement with CARS could be attributed to the difference in γ between air and helium, as previously mentioned. The discrepancy could also be due to the fact that this is a comparison between different properties (density and temperature). Additionally, experimental factors such as the Schlieren camera resolution may contribute to the differences observed between the CARS measurement and the Schlieren reconstruction.

Nevertheless, the width of the gas jet measured using CARS and the temperature profiles obtained from the temperature fits are consistent with the expectations, and these results demonstrate the accuracy and capability of counter-propagating fs/ps CARS to capture temperature variations and gradients in microscale systems.

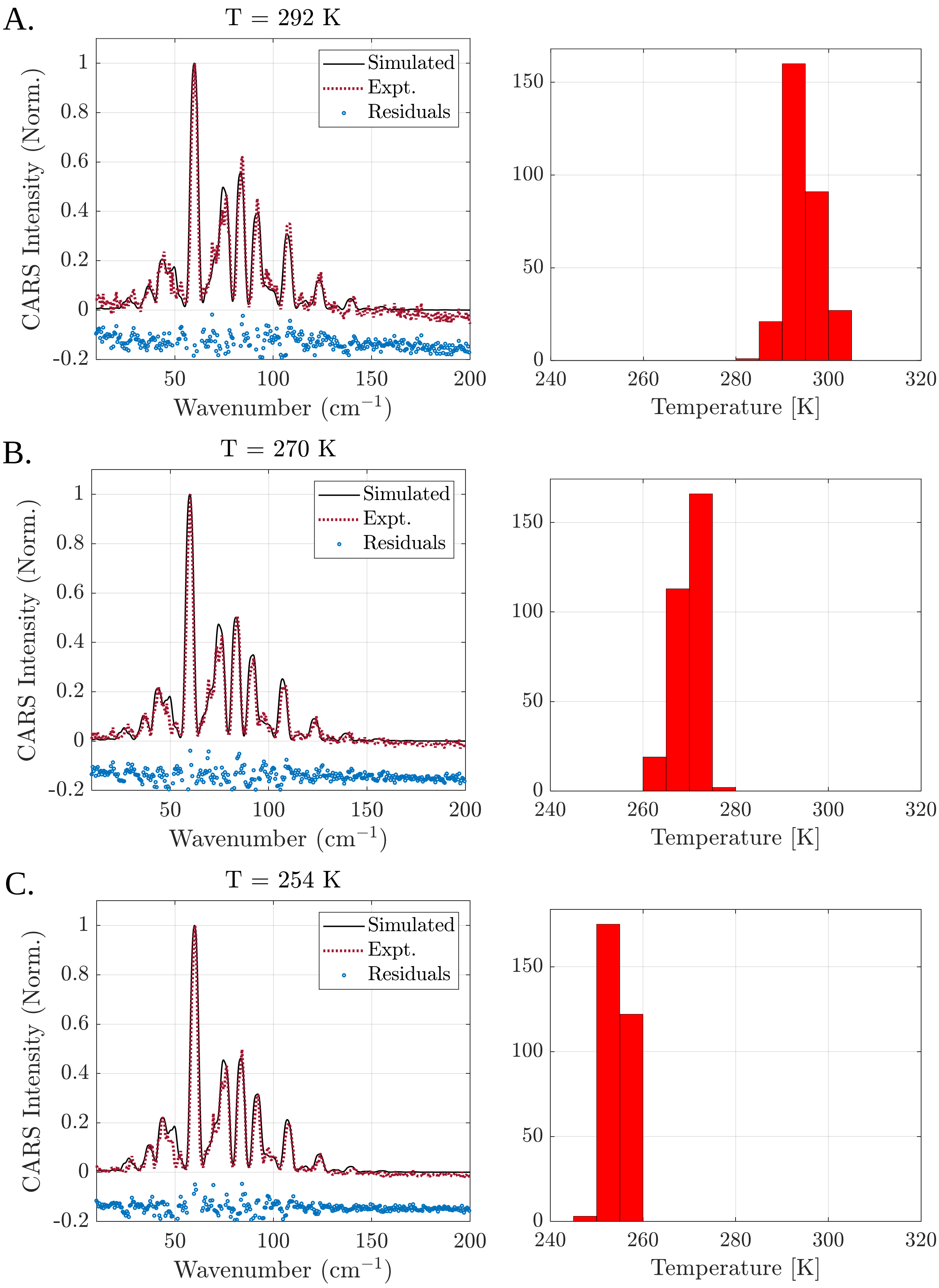

Figure 3.10: Sample CARS temperature fits at various jet positions. A) $\Delta x = -65$ µm. B) $\Delta x = -25$ µm. C) $\Delta x = -5$ µm

3.3.3 Adjustment of Measurement Volume Location with Relative Pulse Timing

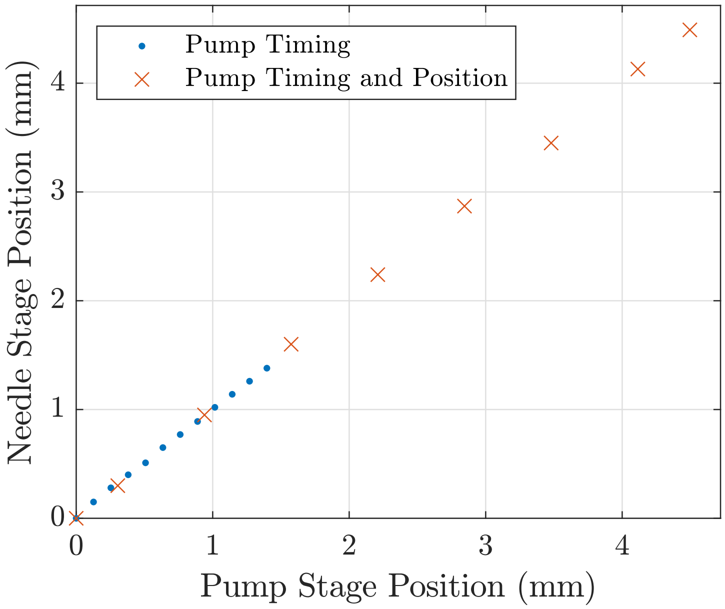

Figure 3.11: Location of the CARS measurement volume vs. pump delay stage position for 200 fs pulses. Blue symbols shows displacement of the measurement volume after a change in temporal overlap of pump/Stokes without simultaneous adjustment of spatial overlap for signal optimization. Red symbols shows data set when spatial overlap was reoptimized after a change in temporal overlap.

The results of the probe volume displacement experiments are shown in Fig. 3.11. Two sets of data were collected to investigate the amount of displacement that could be achieved by adjusting the pulse timing. In one set, only the temporal overlap of the beams was adjusted, while in the other set, spatial overlap was reoptimized as necessary to maintain CARS signal during the probe volume location scan.

From Fig. 3.11, it can be observed that by manipulating the temporal overlap alone, the CARS signal could be maintained while displacing the probe volume by 1.5 mm. However, when spatial overlap was readjusted as necessary, the CARS signal could be maintained up to at least 4.5 mm.

This result demonstrates that a change in the temporal overlap of the beams alone resulted in an equivalent change in the measurement location. Specifically, a 100 µm change in the pump delay stage position resulted in a 100 µm displacement of the measurement volume.

This feature of the counter-propagating scheme is beneficial for conducting measurements in large-scale test facilities, as it allows for adjusting the location of the measurement volume by a known amount through the manipulation of beam timing. It is also useful for precisely moving the probe volume in small, discrete increments, which is advantageous when quantifying gradients in flow properties over a small region.

Overall, the ability to control the probe volume location through temporal overlap adjustment adds significant flexibility and precision to fs/ps CARS measurements using counter-propagating phase-matching. The resolution available with this scheme would enable targeted measurements in specific regions and facilitating the study of spatially varying phenomena in a variety of systems and samples.

3.4 Conclusion

In conclusion, this experiment revealed significant findings regarding the capabilities of the counter-propagating fs/ps CARS system. One key result was the achievement of ultra-high spatial resolution using 60 fs pulses. The results showed that the counter-propagating fs/ps CARS system achieved a remarkable spatial resolution of 15.52 µm, surpassing previous techniques that typically yielded resolutions that are at least an order of magnitude larger. This improvement in spatial resolution was achieved with a relatively small crossing angle of 6°, compared to the 33° crossing angle required in other configurations.

Furthermore, the experiment demonstrated the ability of counter-propagating fs/ps CARS to adjust the measurement volume location by manipulating pulse timing. By changing the temporal overlap of the beams, the experiment showed that the CARS signal could be maintained over a distance of 1.5 mm. When spatial overlap was reoptimized as necessary, CARS signal could be maintained for over 4.5 mm, but if a collinear alignment or shallower crossing angle was used, no optimization would be necessary. This feature allows for precise movement of the probe volume in small increments, enabling targeted measurements in specific regions.

Finally, using the counter-propagating phase-matching scheme, temperature variations resulting from a microscale jet of cold air were accurately characterized, demonstrating the capability of the method to capture temperature gradients with high accuracy and resolution.

Chapter 4

fs/ps CARS in a Dual-Mode Scramjet

4.1 Motivation and Objectives

The objective of this experiment was to implement a fs/ps CARS system in the UVaSCF in order to quantify temperature and local equivalence ratio within the combustor of a dual-mode scramjet. Implementation of a fs/ps CARS system in this facility would enable measurements of local flow properties at locations that were previously inaccessible with ns CARS.

The specific purpose of this experiment was to measure local temperature and species concentrations throughout the combustor, with particular interest in the cavity flameholding region. These measurements were performed for various fueling schemes, allowing for a comprehensive understanding of the temperature and species distribution within the combustor under different operating conditions.

By integrating the fs/ps CARS system in the facility and conducting these measurements, the experiment aimed to provide valuable insights into the combustion process in a dual-mode scramjet. The ability to accurately measure temperature and species concentrations in previously inaccessible regions will contribute to a better understanding of the flow dynamics and combustion behavior, ultimately leading to improved design and optimization of scramjet engines.

4.2 Experimental Setup

4.2.1 University of Virginia Supersonic Combustion Facility

The University of Virginia Supersonic Combustion Facility (UVaSCF) is a high-temperature combustion tunnel designed to replicate flight conditions at Mach 5. This facility utilizes electrical heating and a pressurized plenum to achieve stagnation pressures of up to 10 atm and temperatures of up to 1250 K [70]. It offers extended run times lasting several hours, which allows for the collection of large data sets under statistically steady conditions. In the current study the UVaSCF is equipped with a Mach 2 nozzle. The flow exiting the nozzle simulates the flow exiting the inlet of a scramjet operating in the ramjet-scramjet transition regime. This flow passes then through an inlet isolator, a combustor. and exiting via a divergent nozzle. To facilitate optical measurements using CARS the test section of the facility is fitted with 1 cm thick fused-silica windows. The inner surfaces of the windows are placed 38.1 mm apart.

Figure 4.1 depicts a schematic of the combustor geometry, including the location of fuel injectors. The thesis explores the use of both fuel injection within the isolator (referred to as A injectors) and fuel injection immediately upstream of the cavity step (referred to as B injectors). The B injectors are further divided into separate rows: B1, B2, and B3, positioned at -2.70, -1.69, and -0.67 x/h, respectively.

Performing fs/ps CARS in the UVaSCF presents an additional challenge compared to ns CARS due to spectral broadening by self-phase modulation resulting from the interaction of laser pulses with the windows in the test section. As noted in the literature review, previous experiments utilizing ns CARS employed window extensions to avoid laser damage to the windows [29]. However, with fs/ps CARS, the reduced laser energy requirements of fs pulses to achieve Raman excitation make it possible to perform testing without the need for standoffs.

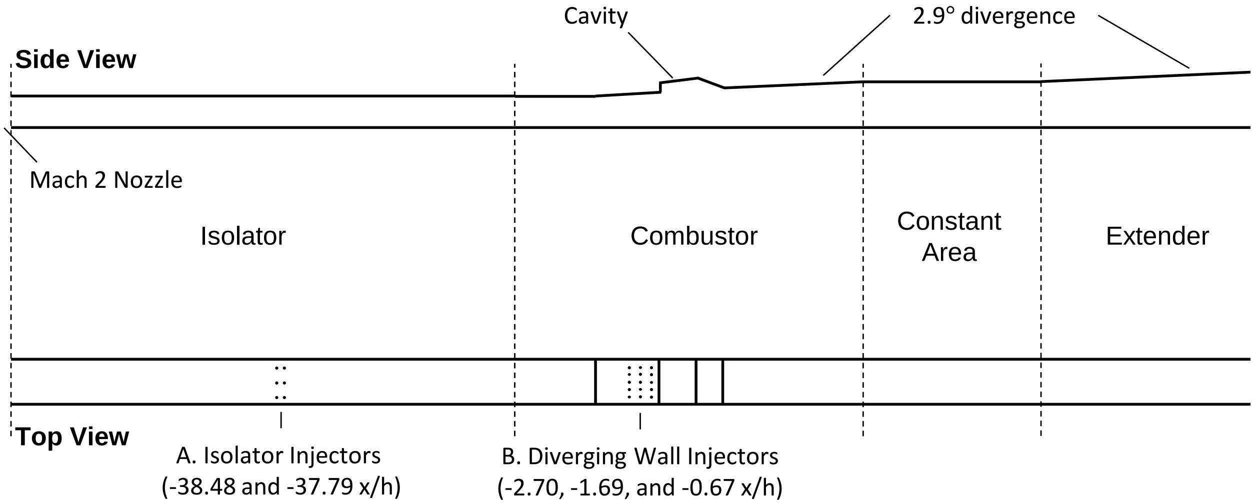

Figure 4.1: Schematic of the combustor geometry showing the location of the fuel injectors used in the experiment.

Still, the interaction between the windows and fs pulses can lead to spectral broadening of the laser beams, which can adversely affect CARS signal generation and accuracy.

Earlier investigations have revealed that the extent of these effects depends on the laser fluence at the inside surface of the windows. Moore et al. found that CARS signal could be generated beyond the laser fluence where spectral broadening occurred. For a 1 cm thick fused silica window, 10.5 mJ/cm^2 was the maximum laser fluence on the window where CARS signal generation would not be negatively impacted [71]. This information was used to devise an optical setup that avoids significant loss in CARS signal intensity due to the facility windows and enable fs/ps CARS measurements in the UVaSCF without window extensions.

4.2.2 Optical Setup

Figure 4.2 illustrates the schematic of the optical setup used for the CARS system. The setup employs a Coherent Astrella amplifier with a pulse duration of 60 fs and a repetition rate of 1 kHz. The laser generates 800 nm amplified fs pulses, which are then directed to a beam splitter. The split beam is subsequently directed to two separate pulse compressors, allowing for individual control of pulse compression despite passing through different optical components. This configuration generates two 60 fs pulses with a spectral bandwidth of 240 cm^{-1}.

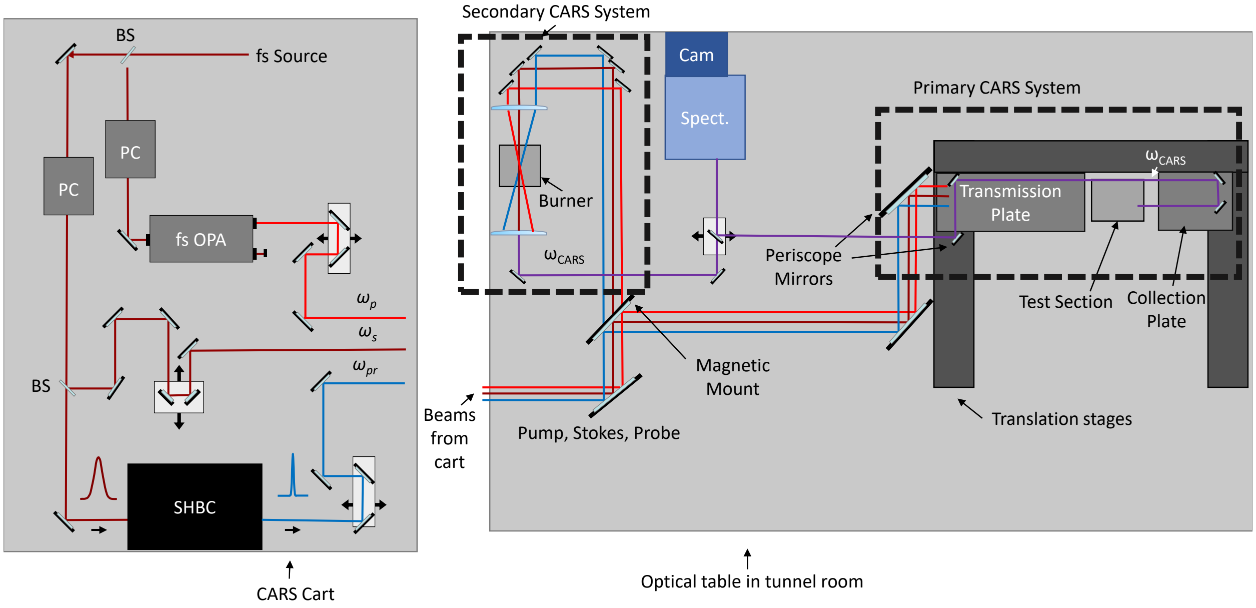

Figure 4.2: Optical layout of the CARS laser cart and primary/secondary CARS systems. PC: pulse compressor. OPA: optical parametric amplifier. BS: beam splitter. SHBC: second harmonic bandwidth compressor. A detailed diagram of the Transmission/Collection plates is shown in Fig. 4.7.

The output of one pulse compressor is directed to a fs optical parametric amplifier (Light Conversion TOPAS-Prime). The purpose of the amplifier is to convert the pump beam to a specific wavelength that can effectively excite the molecular transitions of interest. In this particular experiment, the pump pulse is tuned to a wavelength of 674 nm, which facilitates the excitation of Q-branch transitions for N_2.

The output from the second pulse compressor is split using a beam splitter. The transmitted beam serves as the Stokes beam and remains unaltered from the compressor output. The reflected beam is directed to a pulse shaper to generate a narrowband, picosecond probe beam. Given the anticipated high temperatures in the UVaSCF test section during the experiment, generating a sufficient amount of CARS signal using a single laser pulse becomes challenging.

To address this challenge, the second harmonic bandwidth compressor (SHBC) discussed in Chapter 2.3 was integrated on the laser cart in order to use a high-energy probe to maximize CARS signal generation. Motorized delay stages are included for each beam to ensure precise and repeatable temporal overlap at the measurement region, enhancing the accuracy of the measurements.

Figure 4.3 illustrates the measured time profile of the SHBC output used in the experiment. The measurement was conducted by performing a cross-correlation in time between the probe pulse and the pump/Stokes pulses in a jet of argon, with the non-resonant excitation being measured. The experiment employed a 2.47 ps probe, a shorter pulse duration than those shown in Chapter 2.3. A shorter pulse duration was chosen in order to maximize CARS signal intensity by setting the probe delay as close to the Raman excitation as possible without losing spectral resolution.

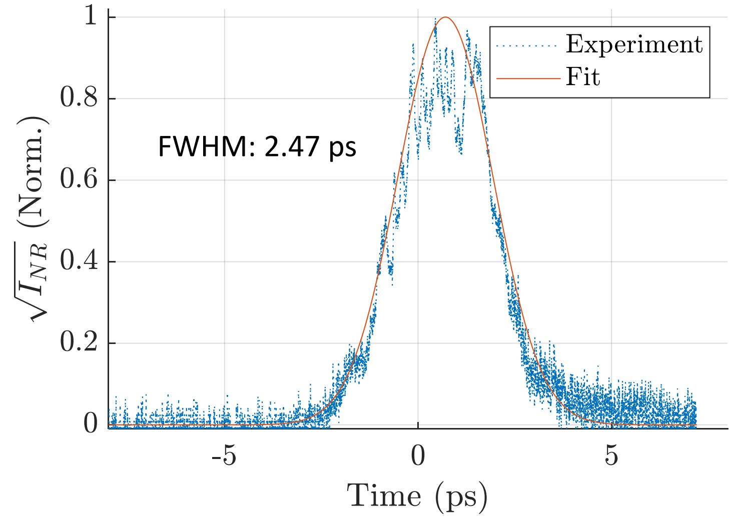

Figure 4.3: Time profile of the SHBC output used in the experiment. The measured pulse duration was 2.47 ps.

The three beams—pump, Stokes, and probe—are routed to the scramjet from an adjacent room where the CARS cart is located onto an optical table located within the tunnel room. The beam energies used in this experiment for pump, Stokes, and probe were 301 µJ, 195 µJ, and 514 µJ, respectively. For the primary fs/ps CARS system, pump, Stokes, and probe are routed together to the test section by a series of 3” mirrors (ThorLabs E02). These mirrors direct the beams through a three-axis stepper-motor driven translation stage system and onto the transmission plate mounted on the stage system. Figure 4.4 depicts a 3D model of this layout created by colleague, Zach Morris.

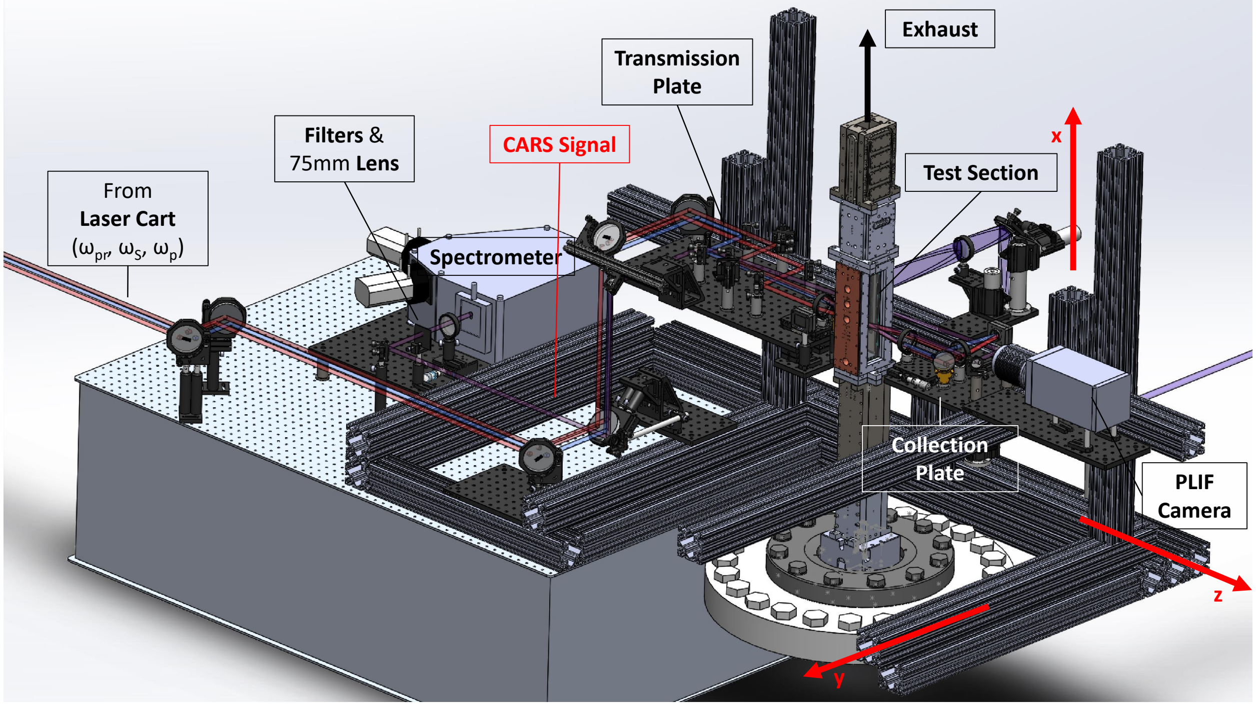

Figure 4.4: Beam routing in UVA Supersonic Combustion Facility.

Two different transmission plate layouts were utilized in the experiment as the initial design proved insufficient in generating the necessary CARS signal to acquire single-shot measurements in preliminary tests in the UVaSCF flame. As a result, modifications were implemented to enhance signal generation within the tunnel. This section will discuss both plate designs and outline the changes made to improve signal generation.

In the initial design shown in Fig. 4.5, each beam on the transmission plate was directed individually to a 150 mm focal length lens. The crossing angle was 7.6°.

During the initial test campaigns conducted in the UVaSCF, it was discovered that the initial design of the transmission plate did not generate a satisfactory level of signal for

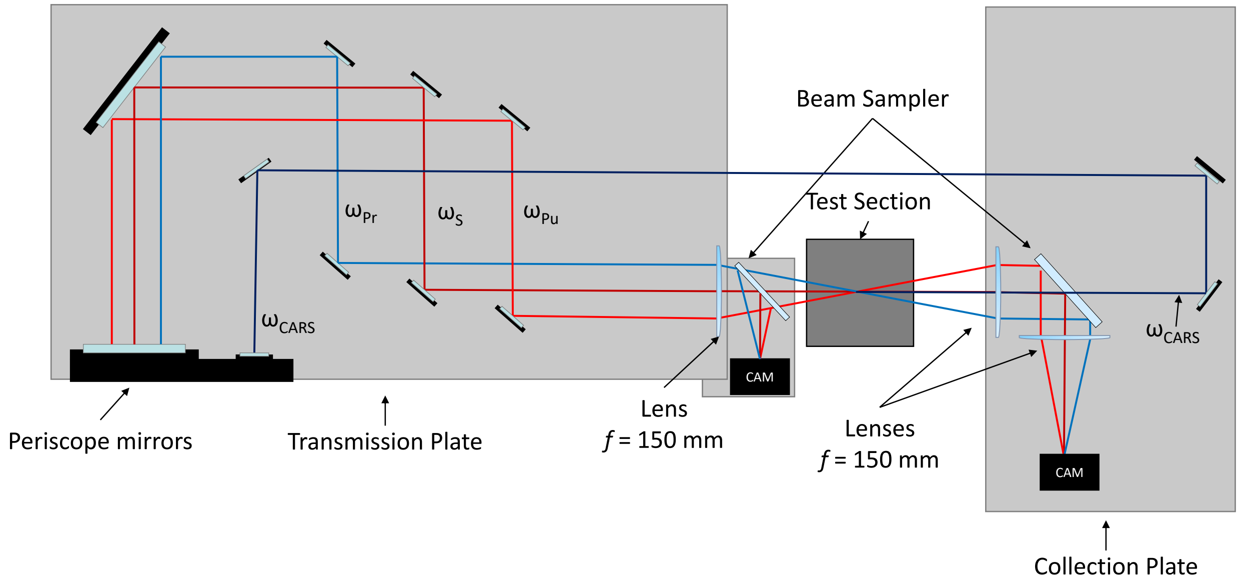

Figure 4.5: Initial design of the optical plates used in the experiment.

CARS measurements within the flame. To address this issue, two strategies were employed to enhance CARS signal generation. Firstly, the transmission plate was redesigned to reduce the crossing angle of the beams. By decreasing the angle at which the beams intersected, the overlapping region was increased, resulting in increased CARS signal generation due to the larger number of molecules being sampled. Secondly, telescopes were incorporated into the Stokes and pump beam paths to improve beam quality at the focal plane and match the plane at which both beams achieve their minimum size. For the pump beam, a telescope consisting of a -150 mm lens and a 130 mm lens was included on the CARS laser cart in order magnify the beam, which results in a smaller beam waist at the focal plane. For the Stokes beam, a telescope consisting of a 130 mm lens and a -100 mm lens was included to correct for astigmatism at the crossing plane, as shown in Fig. 4.6(A). Figure 4.6(B) shows a beam profile image after the telescope was implemented in the beam path, which shows significant improvement in mode quality of the beam at the focal plane.

In the probe beam path, a relay imaging system consisting of a 750 mm spherical lens

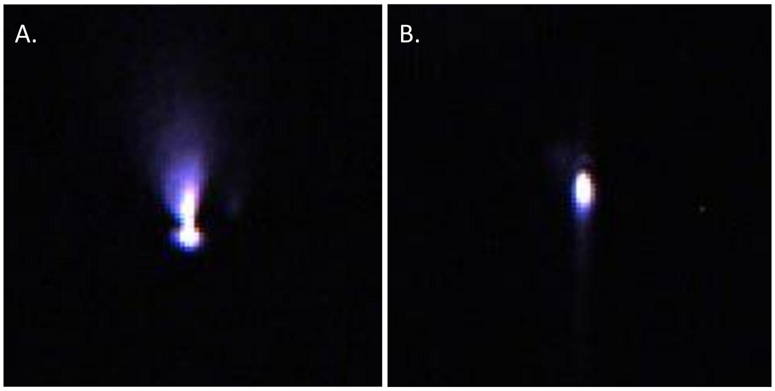

Figure 4.6: Beam profile images of the Stokes beam at the focal plane. A) No telescope. B) With telescope.

and a 1 m spherical lens is utilized to increase the beam diameter and maintain good beam quality after propagation from the second harmonic bandwidth compressor (SHBC) to the combustion tunnel. These changes ensured that the beams were focused and crossed in the same plane, maximizing laser fluence within the probe volume.

The revised design of the transmission plate is depicted in Fig. 4.7. In this design, the pump and probe beams are reflected off a single dichroic mirror towards the focusing lens, while the Stokes beam passes through the dichroic. By using the dichroic mirror, the crossing angle of the beams is reduced, maximizing the region of beam overlap and enhancing CARS signal generation. The beam crossing angle in this configuration was 4.58°.

To aid in alignment, a removable magnetic plate with a beam sampler, neutral density filters, and a camera mounted on it is positioned after the focal lens. This allows for visualization of the spatial overlap of the beams and assists in alignment procedures. The focal plane imaging system, similar to those employed by previous researchers [72, 29], helps ensure precise alignment and control of beam overlap.

Due to potential misalignment caused by facility vibrations and limited access during tunnel operations, remote adjustment of beam crossing is necessary. The transmission plate incorporates two sets of routing mirrors for each beam, along with two remotely operated picomotor optical mounts, enabling precise control over beam alignment and overlap from a remote location.

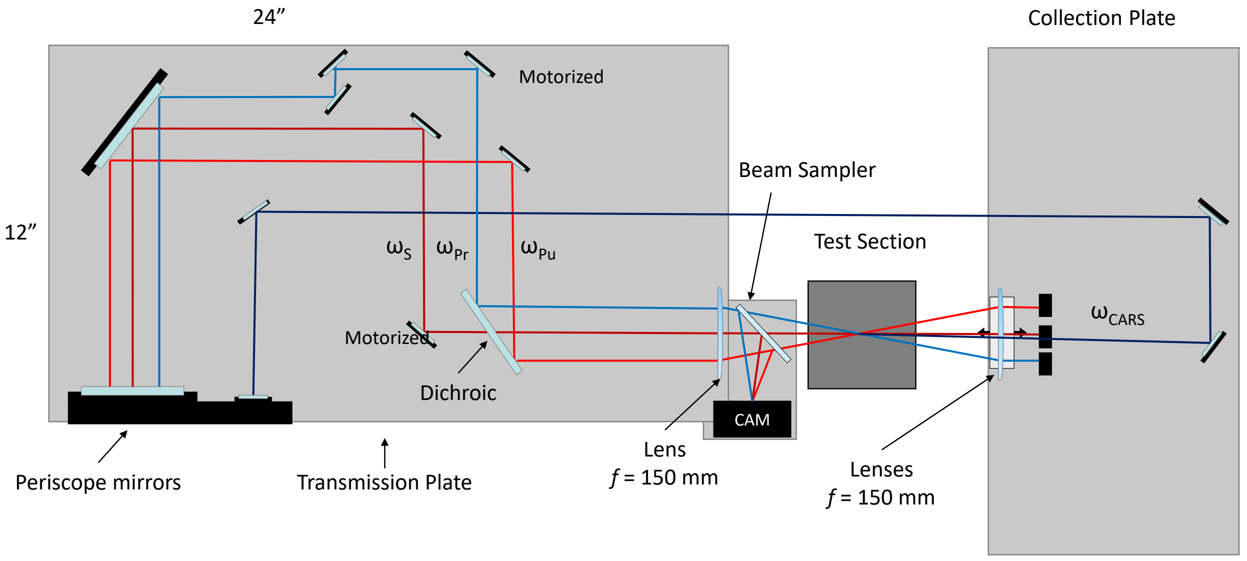

Figure 4.7: Beam path and optical setup of the transmission and collection plates shown in Fig. 4.4 used to overlap the beams in the combustion tunnel.

After crossing in the test section, the beams pass through a second lens of equal focal length to collimate the CARS signal. As shown in Fig. 4.7, this lens is placed on a manual translation stage to ensure collimation after the system is moved into the test section, where window refraction can affect collimation. The CARS signal is then directed back to the transmission plate and a separate periscope assembly via the three-axis stage system. Subsequently, the signal is directed to a spectrometer and an electron-multiplied CCD camera for detection.

To aid in initial alignment of the CARS system through the facility windows, a mock test section with dimensions identical to the tunnel test section was created. The CARS system was first aligned in the air adjacent to the tunnel test section and then translated into the mock test section, with only the front window placed in the beam path. Using the focal plane imaging system and camera, the beams were crossed at the plane where they focused after experiencing refraction effects from the window. Once CARS signal generation through the front window was achieved, the back window was added. However, the introduction of the second window caused additional refraction effects, resulting in misalignment of the collection optics. This was rectified by translating the collimating lens on the collection plate to the plane where the CARS signal was collimated with both windows in the beam path.

Additionally, a secondary CARS system, shown in Fig. 4.2, is accessible by removing a 3” mirror on a magnetic base that directs the beams towards the UVaSCF test section. Motorized stages on the CARS cart allow for precise compensation of path length differences between the primary and secondary CARS systems. The final mirror before the spectrometer, used for collecting CARS signal from the primary system, can be translated aside to enable the routing of signal from the secondary system into the spectrometer. This allows for quick transitions between the primary and secondary systems (less than 1 hour), facilitating comparison of measurements obtained from both systems.

4.2.3 Spatial Resolution

The spatial resolution of the CARS measurements in this experiment was estimated using a small jet of argon gas placed in the mock test section. The resonant CARS signal intensity was measured while translating the jet through the probe volume. As the argon gas replaces the air, a decrease in signal intensity is observed, as shown in Fig. 4.8. A Gaussian curve was fit to the data, which is a fit to the measured convolution of the argon jet and the CARS measurement volume. The FWHM of the fit to the data was 886 µm.

An estimate of the CARS measurement volume can be extracted from this fit analytically by simulating the jet as a Gaussian with a FWHM of 520.7 µm, the inner diameter of the needle in the mock test section, and by assuming that the CARS probe volume is also Gaussian. Under this assumption, the convolution of the CARS probe volume and the simulated jet should have a FWHM that equals the measured convolution of the argon jet and CARS probe volume.

The equation relating the FWHM of the CARS probe volume, the FWHM of the argon jet, and the FWHM of the measureed convolution is given by

$$FWHM_{\text{meas.}} = 2\sqrt{2ln2}(\sqrt{a^2+b^2}), \tag{4.1}$$

where a and b are related to the FWHM of the CARS probe volume and the FWHM of the argon jet by

$$FHWM_{\text{CARS}} = 2a\sqrt{2ln2} \tag{4.2}$$

and

$$FHWM_{\text{Jet}} = 2b\sqrt{2ln2}. \tag{4.3}$$

Thus, the estimated size of the CARS measurement volume was estimated to be 569 µm.

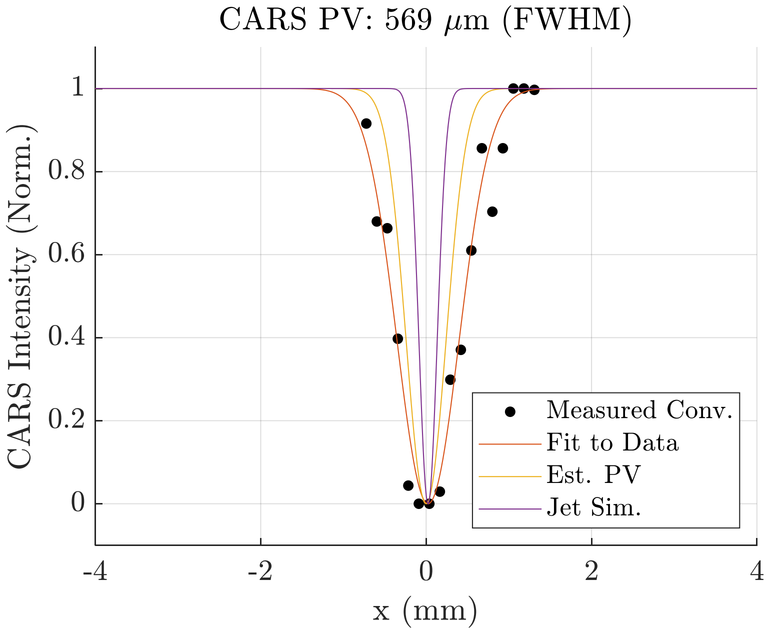

Figure 4.8: Estimate of the CARS measurement volume derived from the simulation of the argon jet and the experimental measured convolution of the Ar jet and the CARS probe volume.

4.3 Facility Considerations

4.3.1 CARS System Stability

A preliminary analysis was conducted to assess the stability of the fs/ps CARS optics and optical tables during operation of the combustion tunnel. The CARS system, spanning two rooms, two optical tables, and multiple optical breadboards, presented a potential alignment challenge when the facility was operational.

CARS spectra were acquired using the secondary CARS system during an unrelated experiment utilizing the UVaSCF. The objective of this analysis was to evaluate whether the operation of the combustion tunnel would impact the stability of the CARS system and the overlap of the laser beams. By acquiring CARS spectra during tunnel operation, the effects of vibrations and other disturbances generated by the tunnel could be assessed.

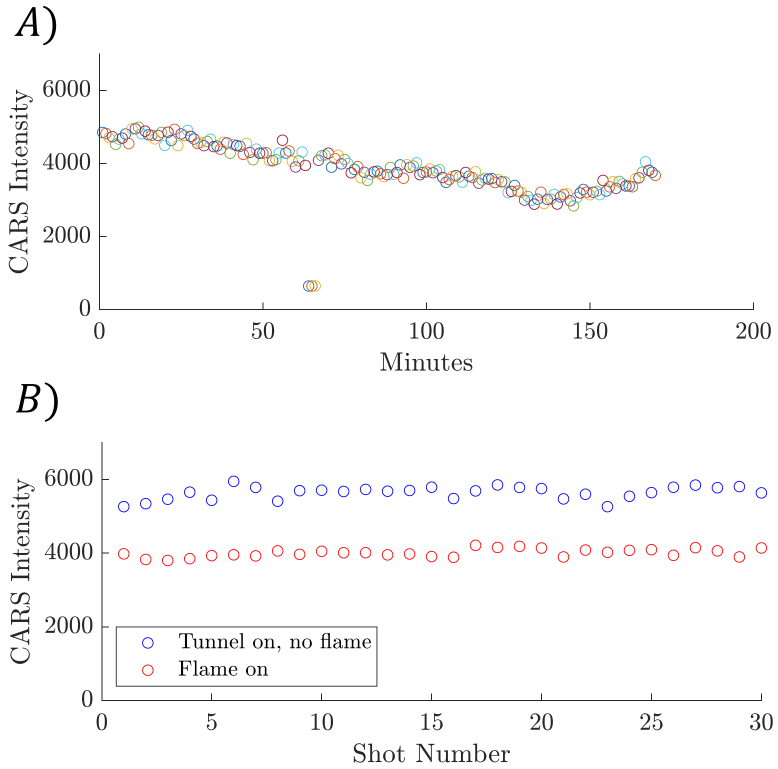

Figure 4.9: A) Measured CARS signal intensity during tunnel operation. B) Shot to shot CARS signal intensity while the tunnel was in operation with and without combustion.

In Fig. 4.9(A), the measured CARS signal intensity during the operation of the tunnel is shown. The measurements were recorded starting while the facility air was heating and during combustion testing. Throughout the experiment, the CARS signal exhibited a slight decrease in intensity, which can be attributed to typical beam drift observed during a normal day. Two outliers in the data correspond to moments when the laser was temporarily blocked. In Fig. 4.9(B) The blue data shows the shot-to-shot variation in CARS signal intensity during tunnel operation without combustion occurring. The red data illustrates the shot-to-shot variation in CARS signal intensity while the flame was active in the tunnel. In both cases, the CARS signal intensity remained constant, providing assurance regarding the stability of the laser system and alleviating concerns related to mechanical vibrations arising from the operation of the combustion tunnel.

These findings indicate that the fs/ps CARS system and its optical tables maintained stability and beam overlap even during the operation of the tunnel. The relatively stable CARS signal intensity throughout the experiment, apart from expected beam drift, reinforces confidence in the stability of the CARS system for conducting accurate measurements in the during operation of the combustion tunnel.

4.3.2 Test Section Windows

Degradation of the windows during facility operation is expected due to the high-temperatures and extended test times. However, early tests in the UVaSCF with fs/ps CARS observed catastrophic window damage beyond what is typically expected. The image in Fig. 4.10 shows the window degradation that occurred during a test campaign in the UVaSCF. The damage to the windows limited optical access to areas away from the flame, making measurements within the cavity inaccessible.

It was later discovered that the window damage was caused by coolant flow on the surface of the windows during tunnel warm up. The coolant would then fuse to the window when the flame was ignited. The coolant was present due to a leak in the plumbing system, resulting

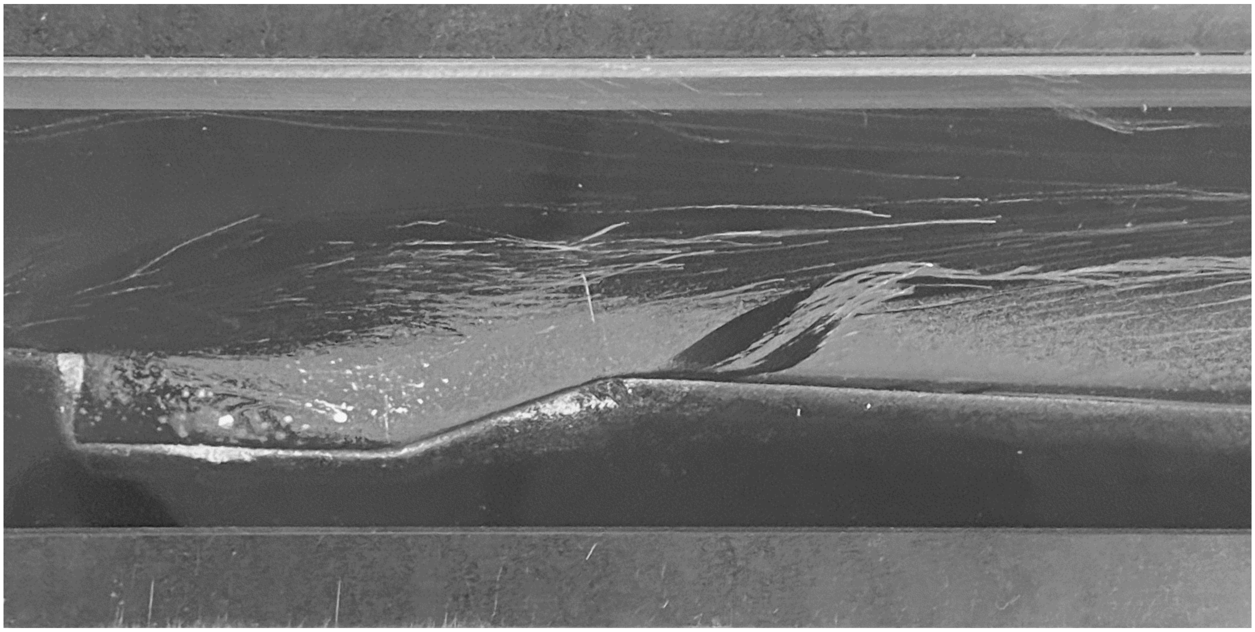

Figure 4.10: Photograph of the window degradation prohibiting CARS measurements.

in coolant getting trapped between the combustor gasket and the tunnel window. Fig. 4.11 provides an image showing the coolant present in the test section.

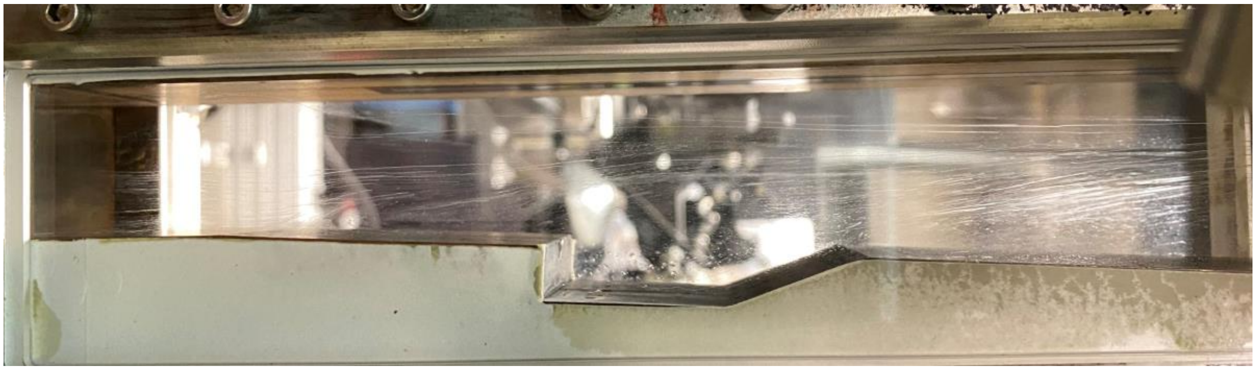

Figure 4.11: Coolant present in the test section.

After identifying the issue, fixing the coolant leak, and cleaning the windows, the tunnel was able to operate without catastrophic degradation to the windows. This allowed for optical access to the entire test section, enabling measurements within the cavity of the UVaSCF.

4.4 Test Cases and Measurement Locations

Table 4.1 summarizes the different CARS test cases performed in the UVaSCF, where both the global equivalence ratio and location of fuel injection were varied to investigate their impact on fuel distribution and temperatures within the combustor.

Table 4.1: Fueling conditions used for CARS measurement campaign.

Case	ϕ_{global}	$\dot{m}(C_2H_4)$ (g/s)	Fuel Injectors
1	0.20	2.536	B1, B2
2	0.32	4.014	B1, B2
3	0.20	A: 0.627, B: 1.882	A, B1, B2

In Case 1, a global equivalence ratio of $\phi_{\text{global}} = 0.20$ was chosen, and the B1 and B2 injectors were used. Case 2 utilized the same fuel injectors but with an increased fuel flow rate, resulting in $\phi_{\text{global}} = 0.32$. The comparison between Case 1 and Case 2 allows for an assessment of how variations in fuel rates for a fixed injector location impact flame temperature and fuel distribution.

Case 3 employed the injectors located in the isolator (A), in addition to the B1 and B2 injectors, at a global equivalence ratio of $\phi_{\text{global}} = 0.20$. This maintains the same global equivalence ratio as Case 1, but introduces fuel further upstream in the isolator, which increases the amount of fuel-air premixing before reaching the cavity. Consequently, the fuel locally injected in rows B1 and B2 is decreased. By comparing Case 3 with Case 1, it is possible to examine how changes in the amount of premixing before the cavity, while maintaining a constant global equivalence ratio, affect flame temperature and fuel distribution within the combustor.

Wall pressure measurements provide additional insights into interpreting the temperature measurements in the combustor. Figure 4.12 displays the wall pressure distributions throughout the test section for each test case. Lower pressures are observed upstream under leaner conditions. This can be attributed to the location of the shock train, which affects the pressure distribution in the combustor. The shock train position is influenced by factors such as fueling conditions and injection strategies.

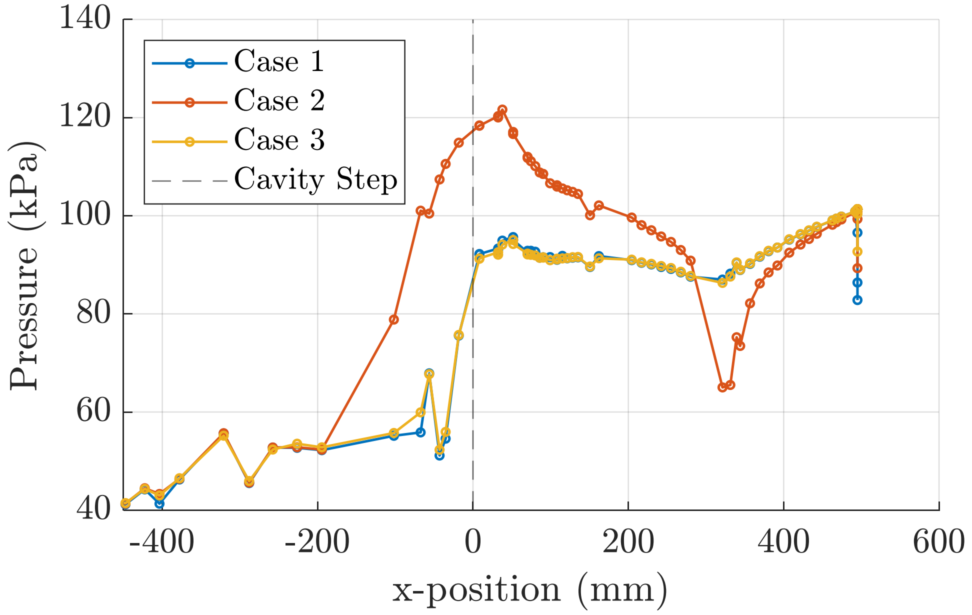

Figure 4.12: Wall pressure measurements for Cases 1, 2, and 3.

Figure 4.13 illustrates the location of the CARS measurements taken in the UVaSCF. To facilitate comparisons between test cases, specific measurement points are assigned nomenclature based on this diagram. The nomenclature is used to refer to temperature measurements and compare them across different test cases.

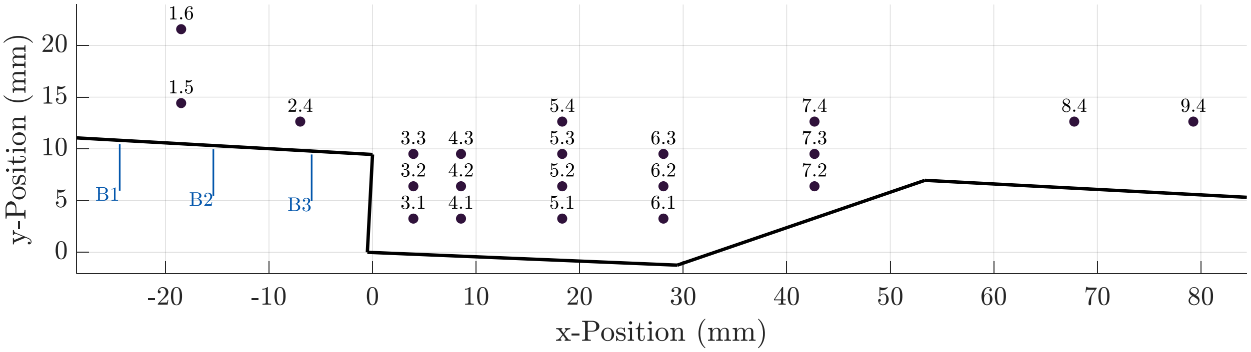

Figure 4.13: Nomenclature for CARS measurement locations in the model scramjet.

The x-plane measurement planes are identified by the first digit in the location labels shown in Fig. 4.13. For instance, the plane containing measurement points 3.1, 3.2, and 3.3 is referred to as plane 3, while the plane containing positions 1.5 and 1.6 is referred to as plane 1.

The numbers after the decimal point in the nomenclature indicate the y-plane where the measurements are located. Rows of measurements are referred to according to this digit. For example, row 1 corresponds to points 3.1, 4.1, 5.1, and 6.1, while row 4 corresponds to points 2.4, 5.4, 7.4, and 9.4.

Concerns were raised regarding potential shifts in the combustion tunnel during heating, which could lead to variations in measurement locations between test cases. However, synchronized OH PLIF images acquired at each position were used to determine measurement location during the test. The same PLIF images were then used to confirm that the measurement locations remained consistent throughout test cases 1 to 3 in post-processing. This consistency allows for direct comparisons of temperature and concentration at each location between the cases. The exception to this is measurement plane 3, and this data was shifted to be closer to the cavity leading edge for Case 2.

4.5 Results and Discussion

4.5.1 Temperature Measurements

Gas temperatures were extracted from the CARS spectra using the spectral fitting routine described in Chapter 2.5 of the thesis. In Fig. 4.14, a sample single shot CARS spectrum with the resulting best-fit temperature. A histogram of fit temperatures for 3,000 single shot CARS spectra from this position is also shown in the figure. Average temperatures and standard deviations at each measurement location were determined from the histogram.

Figure 4.15 shows shot-averaged CARS spectra with the resulting best-fit temperature for the three delays used in the experiment: 4.5 ps, 32 ps, and 42 ps. These probe delays

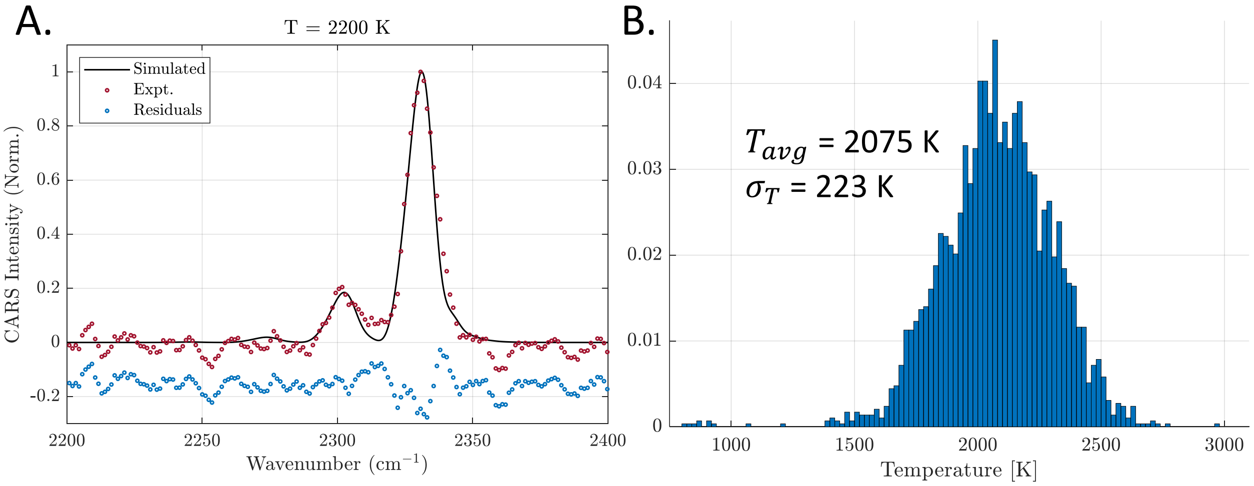

Figure 4.14: A) Sample single-shot CARS with the resulting best-fit temperature. B) Histogram corresponding to Case 1, position 4.1. Average fit temperature: 2075 K. Temperature standard deviation: 223 K.

were chosen in order to have sensitivity over a broad range of temperatures.

Figure 4.16 shows histograms of best-fit temperatures of 3000 single-shot spectra corresponding to CARS spectra acquired at 4.5 ps and 42 ps. The average fit temperature between the two delays was within 10 K, and they also resulted in similar histograms. This result demonstrates that there is good agreement in the fit temperatures between the two delays at the same measurement position and same test case.

Figure 4.18 shows the average fit temperatures at each measurement location for each case. This plot provides an overview of the temperature distribution throughout the measurement domain, allowing for observations of spatial temperature variations.

Figure 4.18 reveals that the temperature upstream of the cavity step is notably lower for Case 1 compared to Case 2 and Case 3. For instance, at position 1.5, the average fit temperature in Case 1 is 803.986 K, while in Case 2 and Case 3, the average temperatures are 899.184 K and 827.77 K, respectively. These temperatures were measured with a probe delay of 32 ps, where CARS spectral features are particularly sensitive to changes in rotational temperature. Figure 4.17 provides a sample temperature fit and histogram illustrating this

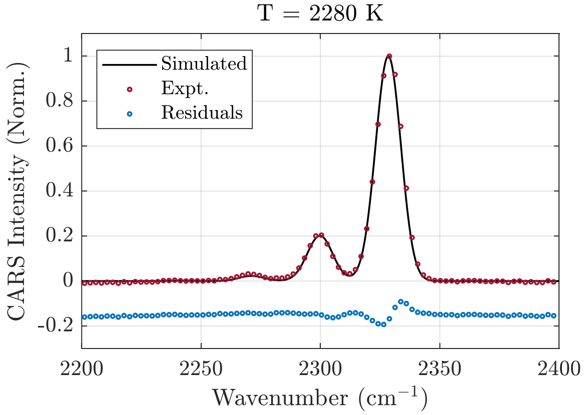

A) 4.5 ps

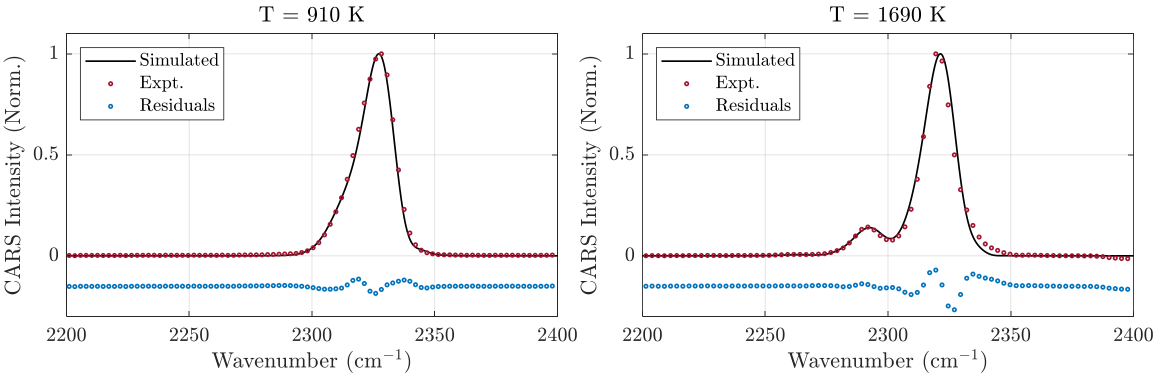

B) 32 ps

C) 42 ps

Figure 4.15: Averaged CARS spectra acquired at three probe delays. A) 4.5 ps, B) 32 ps, C) 42 ps.

lower temperature range.

For Case 1 and Case 3, where the global equivalence ratio was the same, measured pressure distributions were similar as shown earlier in Fig. 4.12. However, despite the similar pressures, Case 1 exhibited lower temperatures at these positions compared to Case 3. This highlights that the importance of local in-situ measurements of temperature, as the two fueling configurations result in different temperatures at discrete points in the flow although they have similar pressure distributions. In contrast, Case 2, which had the highest global equivalence ratio, experienced elevated pressures upstream of the cavity step. This higher pressure condition contributed to the higher temperatures observed at positions 1.5, 1.6, and 2.4 in Case 2 compared to the leaner conditions.

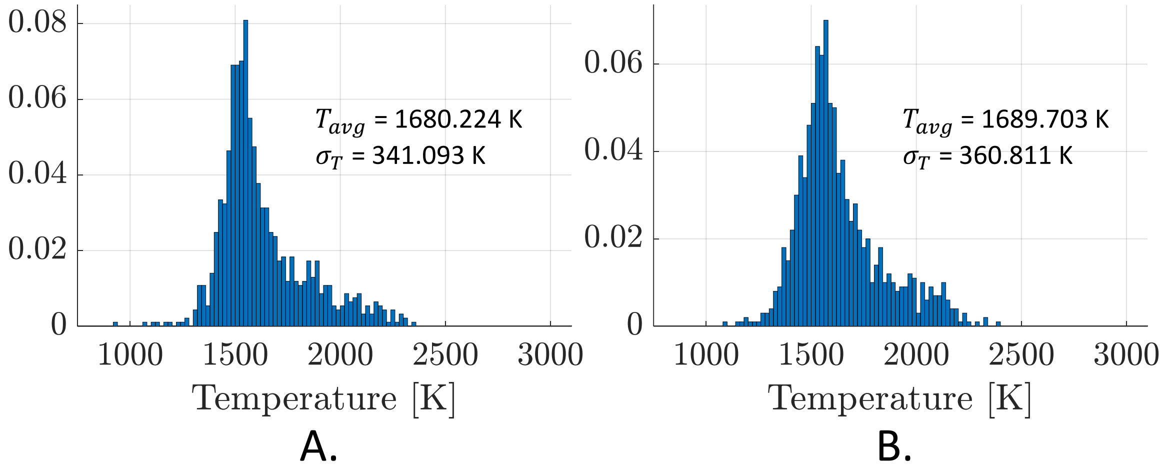

Figure 4.16: Histograms of temperature fits for a probe delay of 4.5 ps (A) and 42 ps (B). Data acquired at position 7.1 for Case 1.

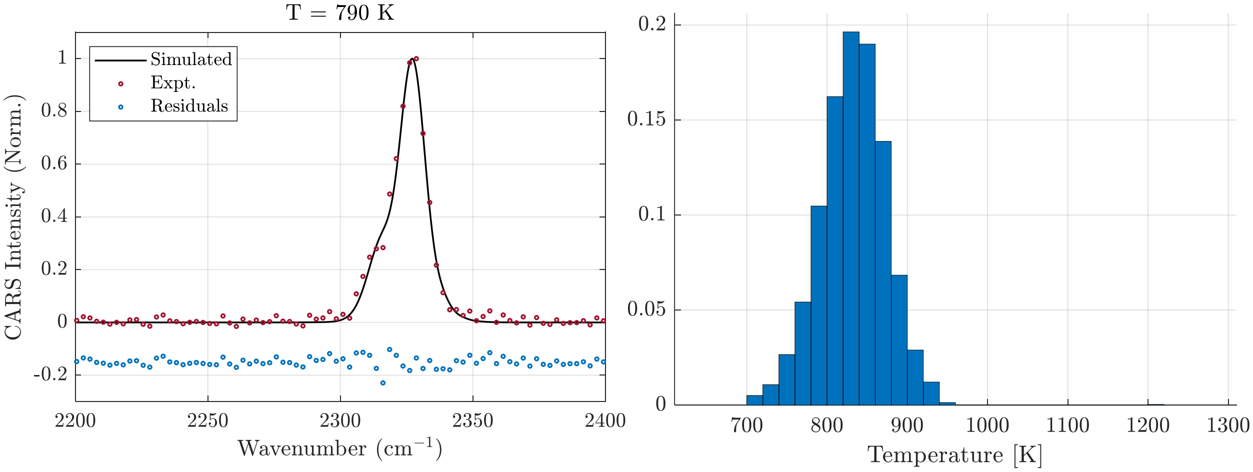

Figure 4.17: CARS data set acquired at a 32 ps probe delay. Data acquired at position 1.5 for Case 3. A) Sample temperature fit at a probe delay of 32 ps. B) Histogram of temperature at position 1.5 for Case 3.

The measured temperatures at the discrete locations shown in Fig. 4.18 were interpolated using a cubic interpolation algorithm in MATLAB to generate the contour plots in Fig. 4.19. The contour plots provide a visual representation of the temperature distribution within the cavity for each case. Figure 4.20 presents a contour plot of the temperature standard deviation within the cavity. The trends observed in these figures will be discussed below.

The degree of heat release within the cavity flameholder can be observed from these figures. In Case 1 and Case 3 ($\phi_{\text{global}} = 0.20$), higher temperatures are observed closer to the floor of the cavity compared to Case 2 ($\phi_{\text{global}} = 0.32$). A noticeable difference in temperature

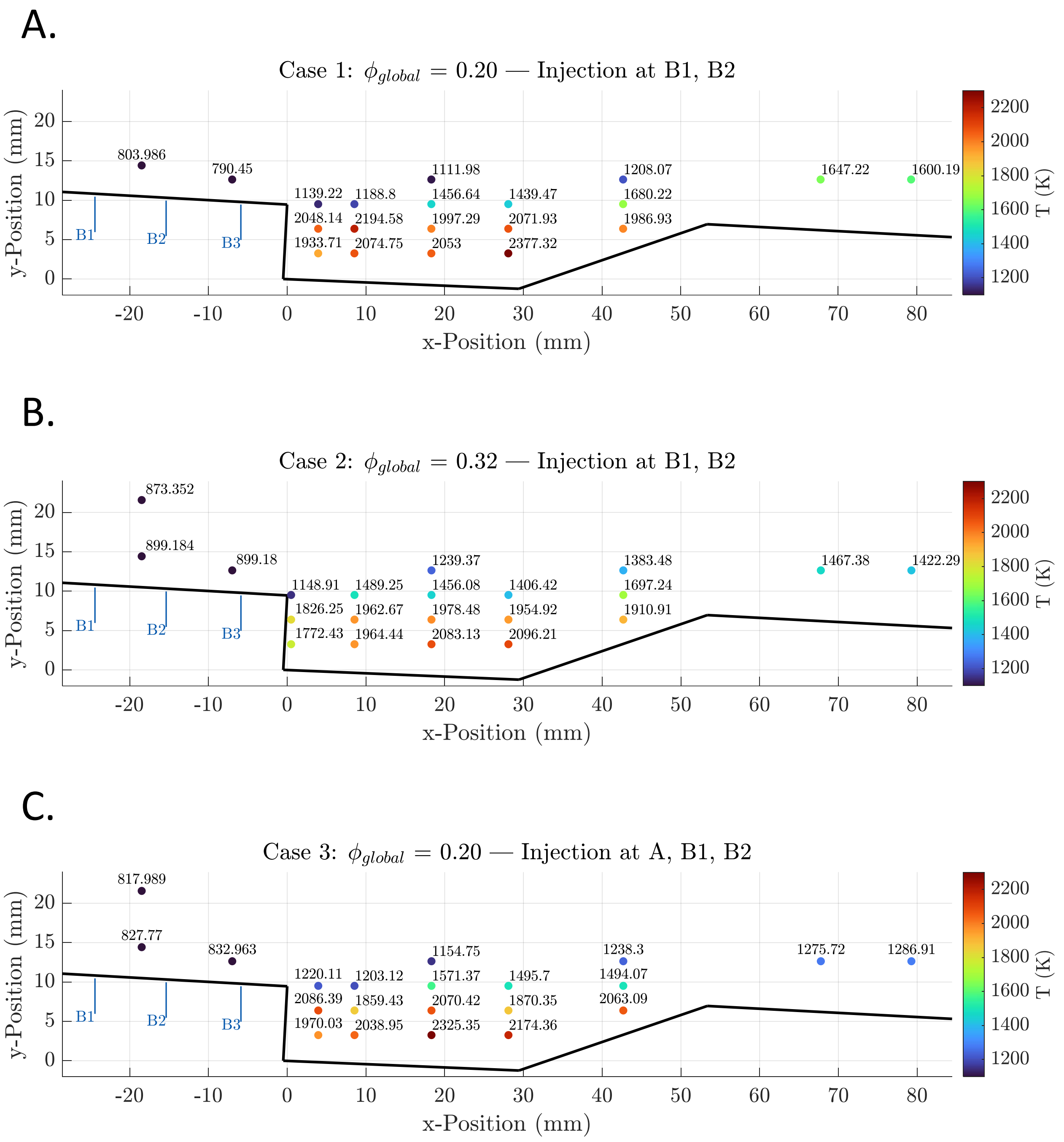

Figure 4.18: Average fit temperatures in the combustor. A) Case 1. B) Case 2. C) Case 3.

A.

Case 1: $\phi_{global} = 0.20$ — Injection at B1, B2

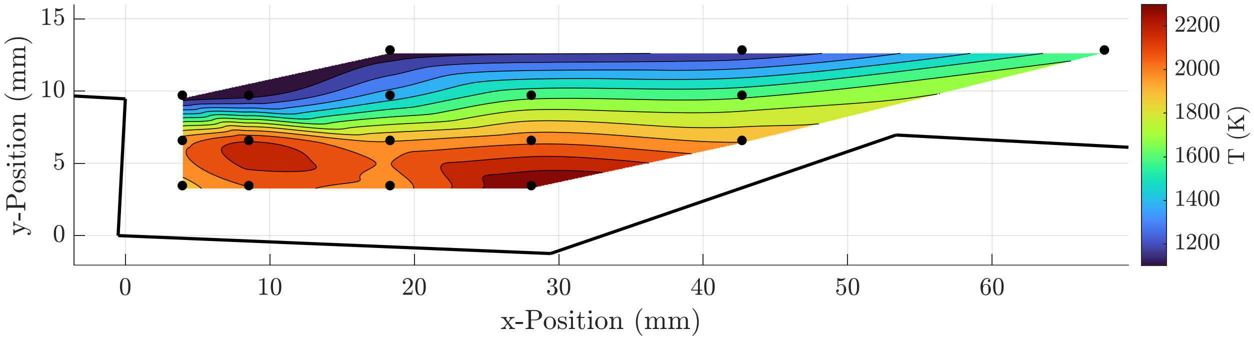

B.

Case 2: $\phi_{global} = 0.32$ — Injection at B1, B2

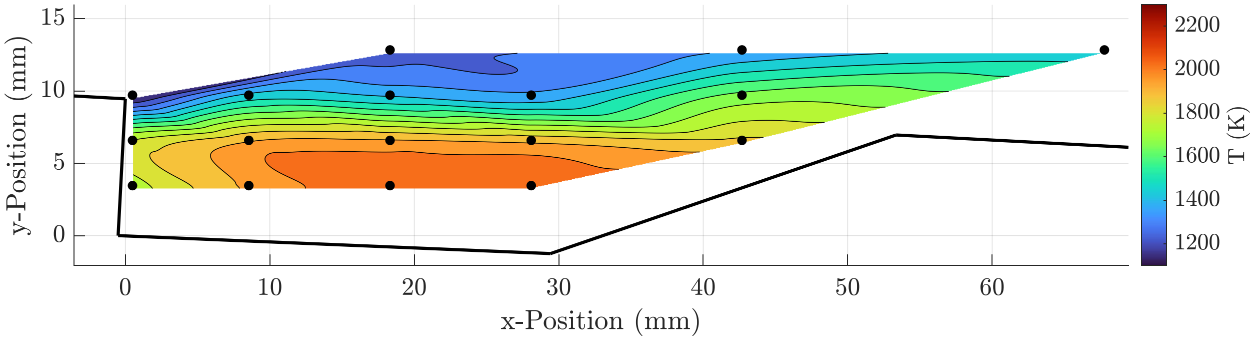

C.

Case 3: $\phi_{global} = 0.20$ — Injection at A, B1, B2

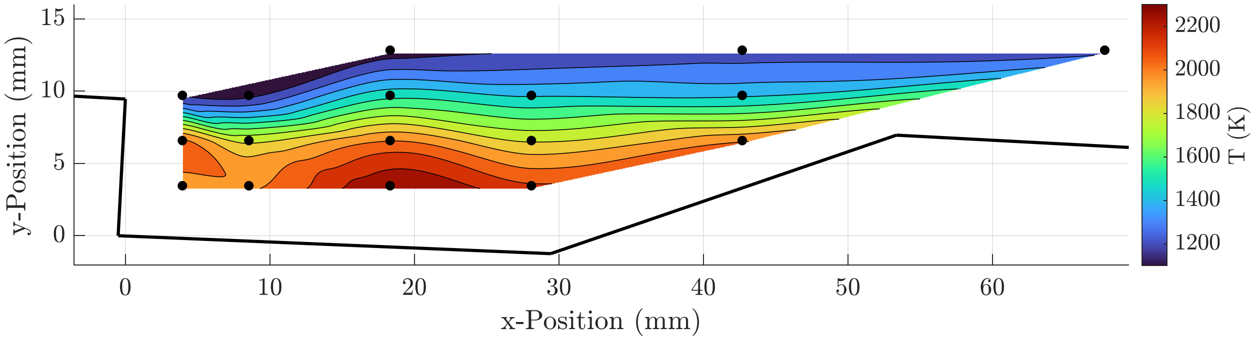

Figure 4.19: Contour plots of average fit temperatures for measurement positions located in the region cavity. Measurements at the discrete locations were interpolated to generate the contour plots. A) Case 1. B) Case 2. C) Case 3.

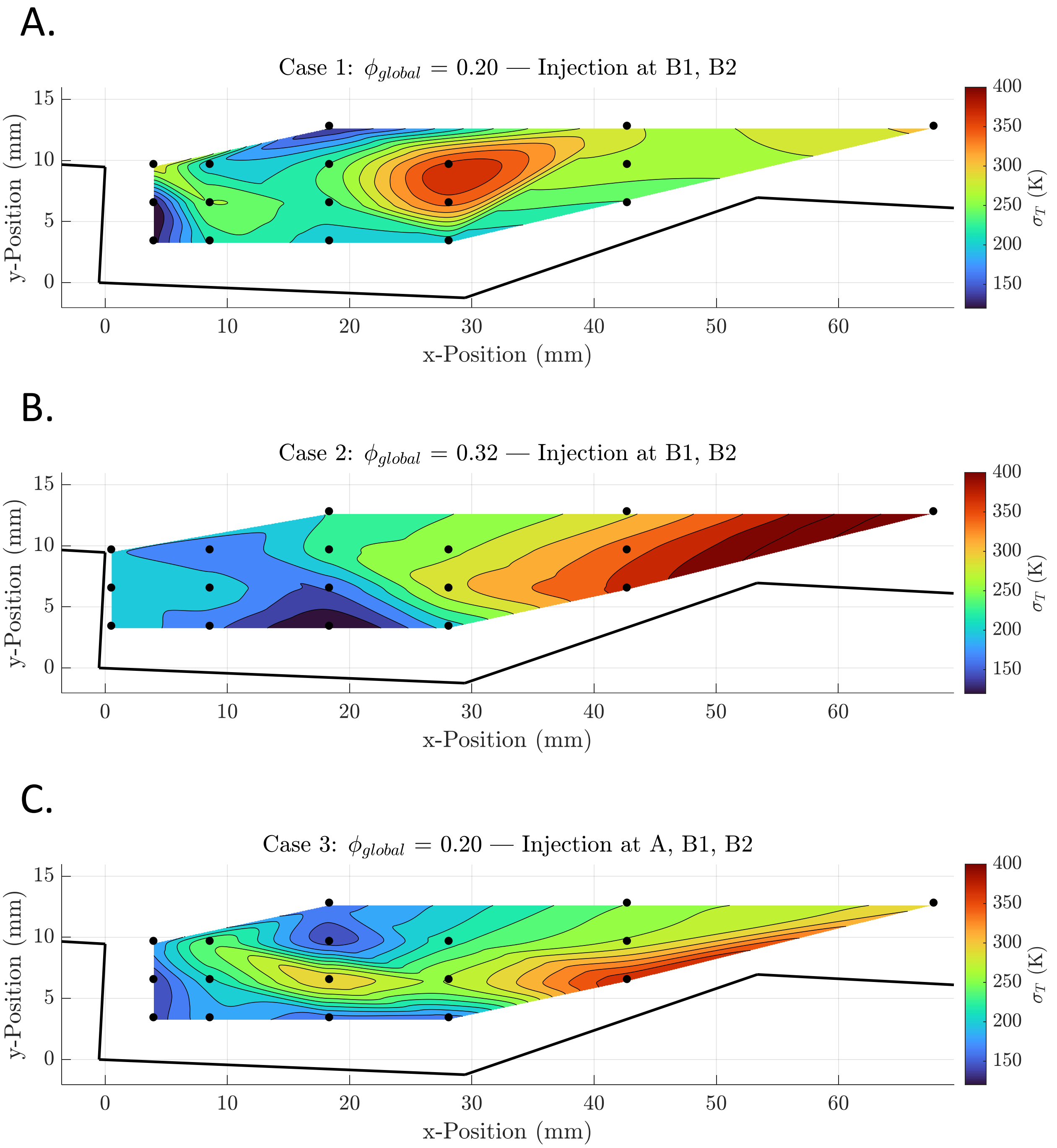

Figure 4.20: Contour plots of the standard deviations corresponding to the data shown in Fig. 4.19. A) Case 1. B) Case 2. C) Case 3.

is observed at position 5.1 (center of the cavity, adjacent to the floor) between Case 2 and Case 3. The average fit temperature at this position in Case 3 is 11.63% higher compared to Case 2 (2325 K vs. 2083 K), and temperatures across measurement row 1 (adjacent to cavity floor) are 6.43% greater in Case 3 than in Case 2. Temperatures in this measurement row are relatively similar between Case 1 and Case 3 which had the same global equivalence ratio. The average temperature in this row was 1.39% greater in Case 3 than in Case 1. This suggests that a global equivalence ratio of 0.20 results in greater heat release in the cavity than a global equivalence ratio of 0.32. At position 7.1 (located in the plane of the cavity ramp, close to the floor), Case 3 exhibits the highest average fit temperature, followed by Case 1 and Case 2. The average fit temperatures at this position for Case 3, Case 1, and Case 2 are 2063 K, 1987 K, and 1911 K, respectively. These results align with the decreasing order of local injection at B1 and B2, which also suggests that a global equivalence ratio of 0.20 results in greater heat release within the cavity compared to a global equivalence ratio of 0.32. Furthermore, when comparing Case 1 and Case 3, slightly higher temperatures are observed for Case 3, where there is less fuel at B1 and B2. Thus, we can conclude that there is a trend that there is greater amounts of heat release closer to the floor of the cavity with less fuel at B1 and B2.

In Case 1 and Case 3, two distinct ”hot” regions are observed. In Case 1, the region with the highest temperature is found in plane 6, just upstream of the cavity ramp. On the other hand, in Case 3, the highest temperature is observed in plane 5, closer to the cavity leading edge. This difference could possibly be attributed to the different x-positions at which fuel enters the cavity in the two fueling schemes. This could be due to the differences in the momentum of the fuel jets that allows fuel to penetrate at a different depth with different mounts of fuel injected.

Temperatures downstream of the cavity ramp show significant differences between Case 1 and Case 3, despite having the same global equivalence ratio. Fig. 4.18(A) and 4.18(C) demonstrate that Case 1 records higher temperatures at these positions compared to Case

3. At position 8.4, the temperature in Case 1 is 371 K higher than in Case 3 (1647 K vs. 1276 K), and at position 9.1, the temperature in Case 1 is 313 K higher than in Case 3 (1600 K vs. 1287 K). Additionally, temperatures at these two positions are higher in Case 2 compared to Case 3, potentially due to the higher pressures observed at these planes for a global equivalence ratio of 0.32. This observation again shows that even though Case 1 and Case 3 show nearly identical pressure distributions measured at the walls, they have very different temperature distributions when measuring local in-situ temperature.

From the contour plots shown in Fig. 4.19, it is evident that Case 2 exhibits colder temperatures in the cavity overall when compared to Cases 1 and 3. This could be due to the fact that the local equivalence ratio in the cavity is greater than the stoichiometric ratio in Case 2, resulting in less heat release and lower temperatures. In contrast, Cases 1 and 3 exhibit pockets of higher temperature in the cavity. This could be because the local equivalence ratio is closer to 1, leading to higher temperatures.

Figure 4.21 shows the average fit temperatures along measurement rows 1, 2, and 3 for each test case. It is observed that temperatures along measurement row 2 exhibit less variability in temperature in Case 2 compared to the leaner conditions of Cases 1 and 3. Fig. 4.21(B) presents a plot that compares cavity x-position and temperature for these points. Case 2 shows the least temperature variation along this row. In contrast, both Case 1 and Case 3 display spatial variations in local temperature as the distance from the cavity edge increases. This suggests that there is less spatial variation in measured temperature along these measurement points with more fuel at B1 and B2, as in Case 2.

The greater temperature uniformity in Case 2 could potentially be attributed to a change in the shear layer resulting from the richer injection into the cavity. To further investigate this phenomenon, a histogram of the fit temperatures for points 5.1, 5.2, and 5.3 in Case 3 is shown in Fig. 4.22. Notably, a bimodal distribution is observed in Fig. 4.22(B), indicating significant fluctuations in the presence of hot products and cooler reactants at this position. In contrast, this fluctuation is absent at the richer condition of Case 2. This supports the

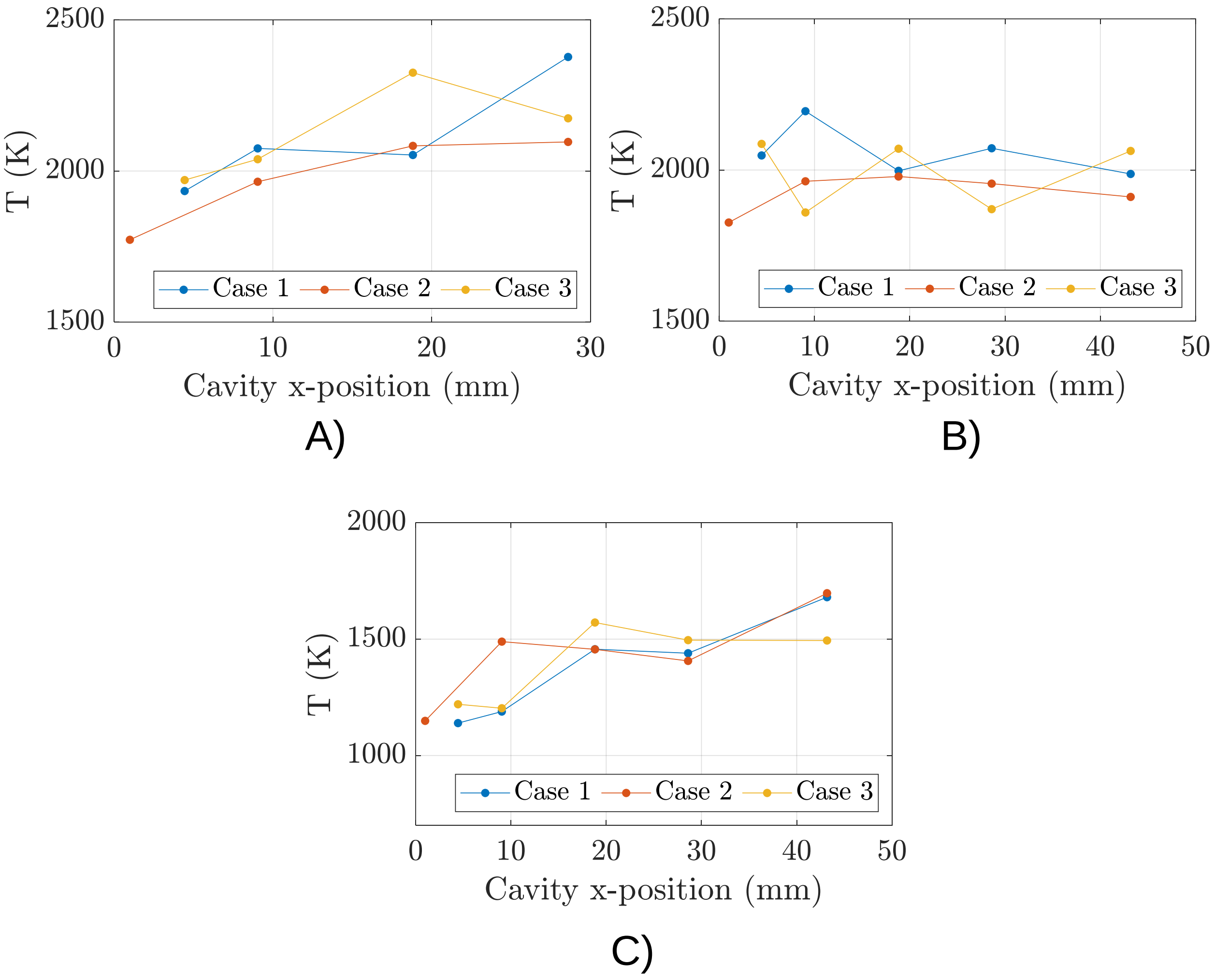

Figure 4.21: Temperatures at various x-positions in the cavity for cases 1, 2, and 3. x = 0 corresponds to the beginning of the cavity step. A) Measurement Row 1. B) Measurement Row 2. C) Measurement Row 3.

notion that the location of the unsteady shear layer is changing between the different fueling schemes. Future investigations, including a comparison with synchronized OH planar laser induced fluorescence images, can provide further confirmation of this hypothesis.

It is important to consider the distribution of instantaneous temperature measurements like the one observed in Fig. 4.22(B) when interpreting the maps of temperature standard deviation shown in Fig. 4.20. The reported values in some regions may not follow a normal Gaussian distribution due to the local flowfield at those locations.

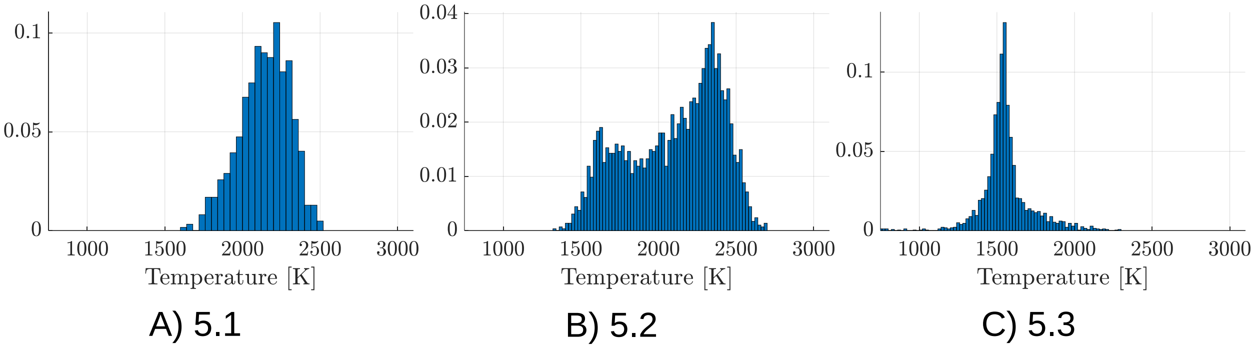

A) 5.1

B) 5.2

C) 5.3

Figure 4.22: Histograms of fit temperatures for Case 3 at positions 5.1 (A), 5.2 (B), and 5.3 (C).

4.5.2 Qualitative Fuel Distributions

Quantitative measurements of local fuel concentration were not available in this experiment due to the lack of a CARS spectral model for C_2H_4. However, qualitative measurements of fuel species relative to N_2 can be obtained by analyzing the ratios of spectral line intensities associated with the molecules of interest.

A peak ratio approach was employed , where the square root of the intensity of C_2H_4 (represented by $I_{C_2H_4}$) was divided by the square root of the intensity of N_2 (represented by I_{N_2}). This ratio, $\sqrt{I_{C_2H_4}}/\sqrt{I_{N_2}}$, provides a qualitative measurement of the C_2H_4 concentration based on the area under the curve of the spectral features [34].

While these qualitative measurements offer insights into how the fuel distribution in the engine changes between cases, they do not provide precise quantitative values. Additional efforts to achieve quantitative measurements of local equivalence ratio are underway and are discussed in detail in Chapter 5 of this thesis.

A sample CARS spectrum showing N_2 and C_2H_4 is shown in Fig. 4.23(A). Despite the pump beam being tuned to excite N_2 at 2331 cm^{-1}, the broadband excitation provided by the fs pulses also resulted in the excitation of the C_2H_4 ν_1 band at 3022 cm^{-1}. This spectral feature was utilized to compute ratios between the N_2 and C_2H_4 spectral features for qualitative comparison of C_2H_4 concentration among the different test cases.

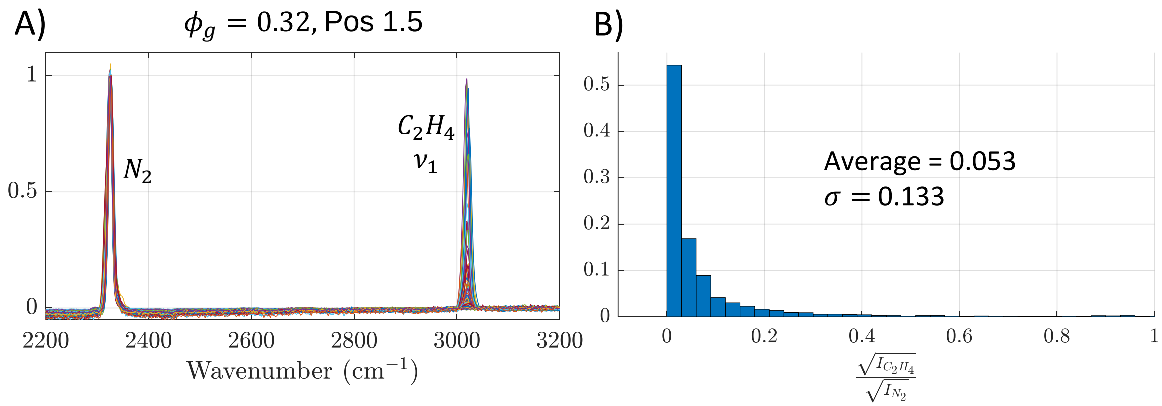

Figure 4.23: A) CARS spectra recorded at a 4.5 ps probe delay with C_2H_4 present. Data recorded at position 1.5 for Case 2. B) Histogram of measured peak ratios at this position.

To determine the relative C_2H_4 presence, the peak ratio between the C_2H_4 band and the N_2 feature was calculated for each frame. Frames with a C_2H_4 signal-to-noise ratio below 5 were excluded to ensure that concentrations were not computed for frames below the detection limit of ethylene. Average peak ratios and standard deviations were then calculated for each measurement location.

Figure 4.23(B) provides a histogram of the calculated C_2H_4 concentration for a specific measurement position, illustrating that the distribution of values does not follow a normal distribution, which is possibly due to many frames where C_2H_4 is below the detection limit. This characteristic should be considered when interpreting the plots of standard deviation given later.

Average C_2H_4 peak ratios above the fuel injectors for Cases 1, 2, and 3 are presented in Fig. 4.25. These measurement locations were selected during Case 1 data acquisition based on where significant fuel was visible in the CARS spectra. The same positions were recorded and repeated for Case 2 and Case 3.

Consistent with expectations, the highest concentration of C_2H_4 is observed directly above the B2 fuel injectors in all three cases. Case 2, which had the highest local injection at B1 and B2, exhibited the greatest concentration of C_2H_4 at this point.

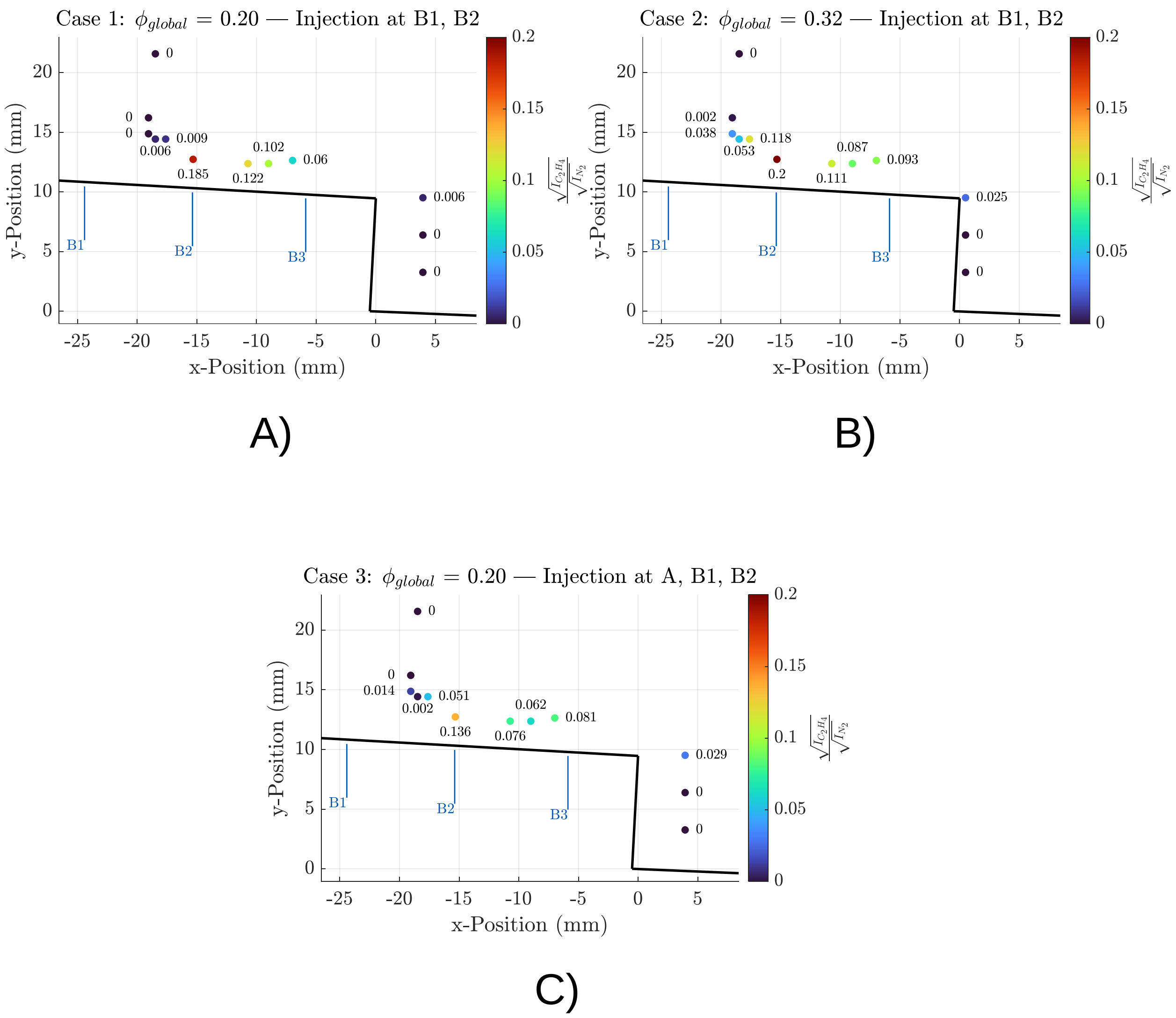

Figure 4.24: Average C_2H_4 peak ratio upstream of the cavity. A) Case 1. B) Case 2. C) Case 3.

Fuel is detected at greater distances from the injectors (larger y-positions) for both Case 2 and Case 3 compared to Case 1. In Case 2, this can be attributed to more fuel penetrating into the free stream due to the increased pressure of the fuel jet resulting from the higher local fuel injection at B1 and B2. In Case 3, the presence of fuel further away from the wall is likely due to the mixing of the fuel injected at position A (in the isolator) with the freestream air. Since the fuel at position A was injected from the same side of the tunnel as the B1 and B2 injectors, most of the fuel is concentrated closer to the wall of the combustor, which explains in the absence of fuel closer the center of the duct even with fuel injection in the

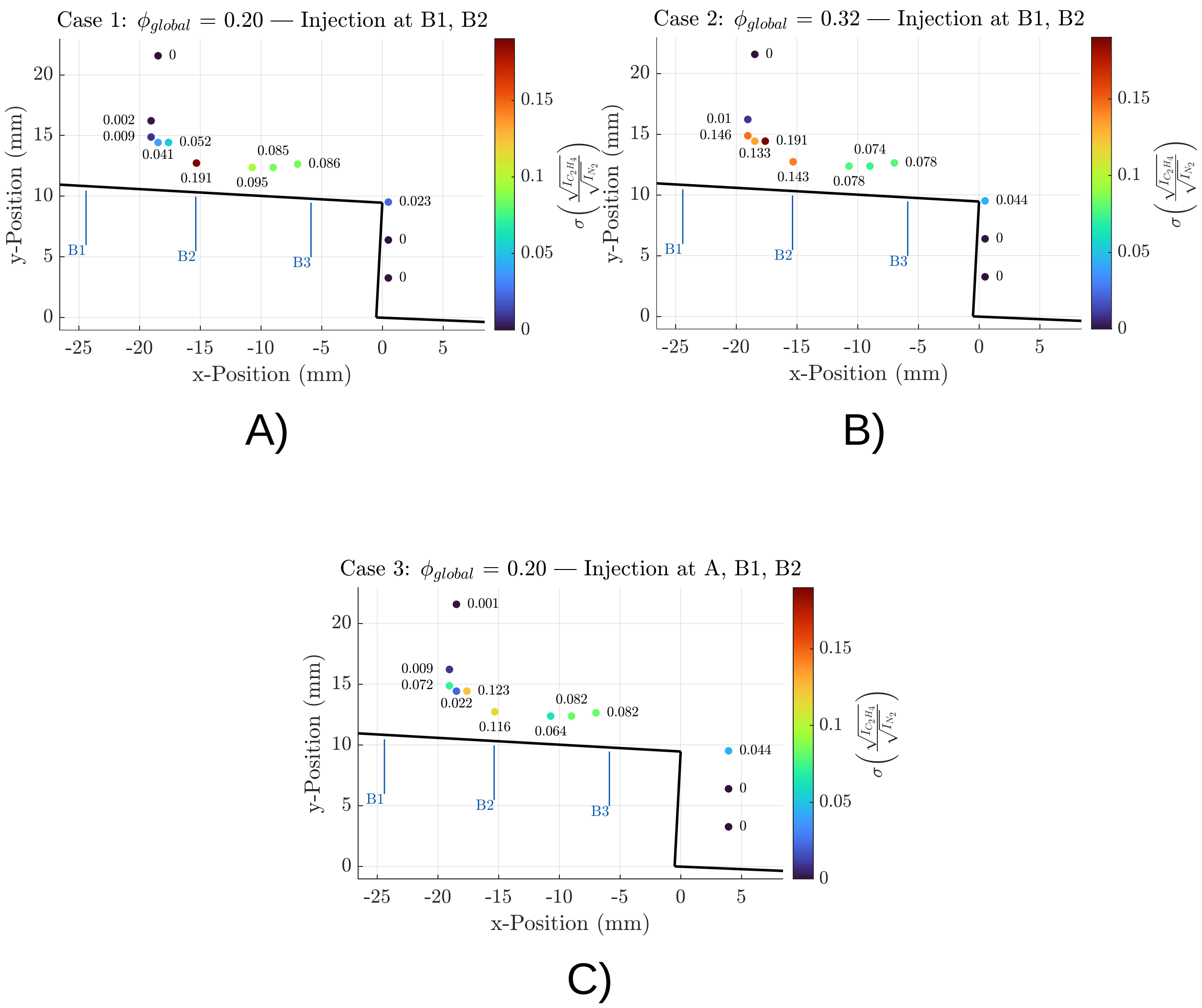

Figure 4.25: C_2H_4 peak ratio standard deviation upstream of the cavity. A) Case 1. B) Case 2. C) Case 3.

isolator.

The contour plots in Fig. 4.26 illustrate the average C_2H_4 peak ratio distribution in the cavity for each test case, while the contour plots in Fig. 4.27 depict the standard deviation in C_2H_4 peak ratios in the cavity. These contour plots were generated in the same manner as the temperature contour plots (using a cubic interpolation in MATLAB).

In Case 1, a significant portion of the fuel enters the cavity at plane 5. This suggests that the majority of the fuel enters the cavity at the middle or at the rear of the cavity. In Case 2, a higher concentration of fuel is observed closer to the leading edge of the cavity. In Case 3,

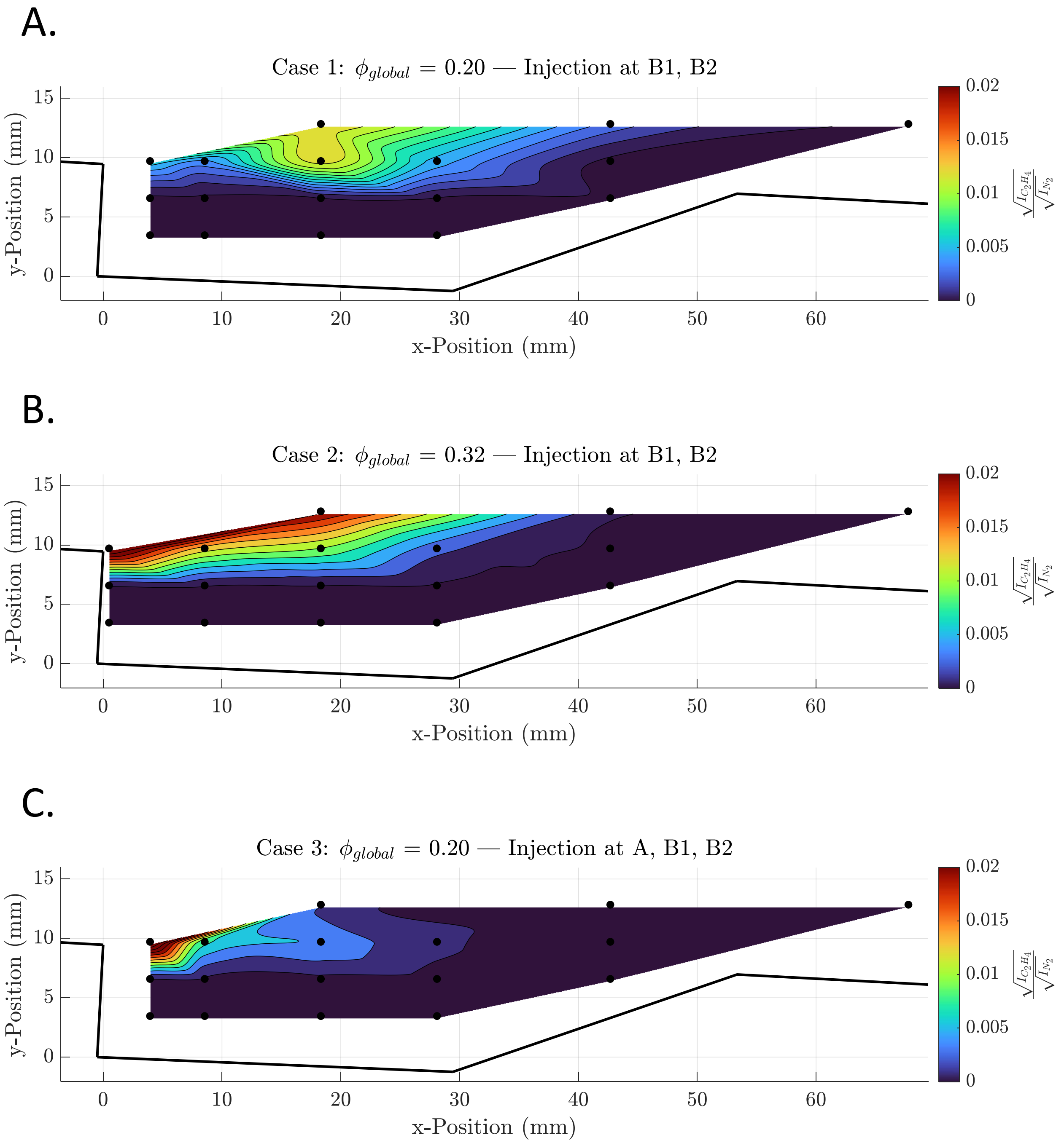

Figure 4.26: Contour plots of average C_2H_4 peak ratios in the cavity. A) Case 1. B) Case 2. C) Case 3.

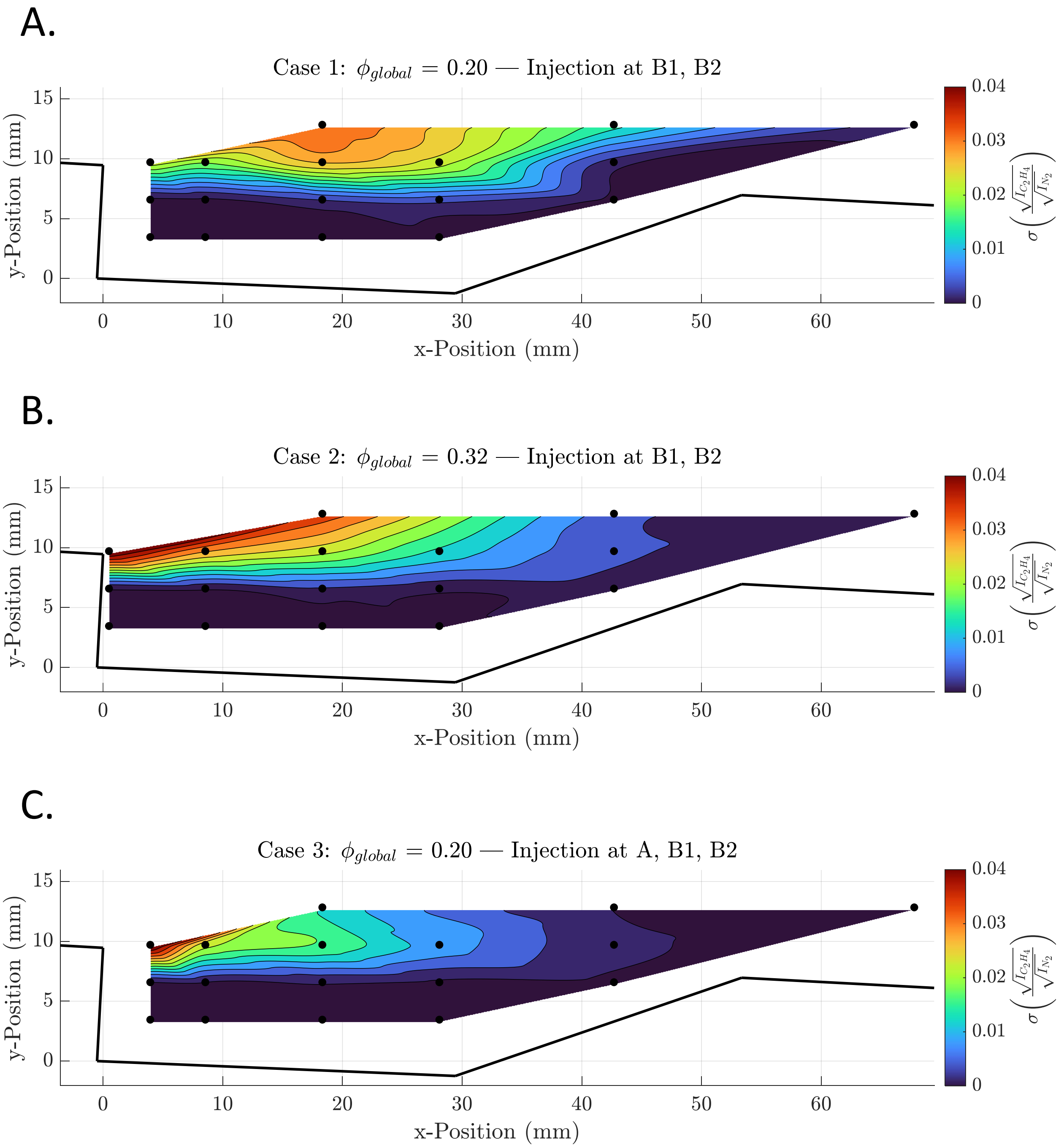

Figure 4.27: Contour plots of C_2H_4 peak ratio standard deviation in the cavity. A) Case 1. B) Case 2. C) Case 3.

most of the fuel enters the cavity near the leading edge and does not mix as far downstream as in Case 1.

Notably, the fuel concentration at position 3.3 (just downstream of the cavity leading edge) is approximately 5 times higher in Case 3 compared to Case 1, although there is more fuel injected locally at B1 and B2 in Case 1. This could be due to the fact that the fuel in Case 3 does not penetrate as far into the free stream as Case 1 due to the lower momentum of the fuel plume. It could be that the fuel near the wall is entering the cavity just downstream of the leading edge as most of the fuel is present close to the wall. Greater characterization of the fuel distribution in measurement row 4, as well as insight into the shock structures, could provide insight into why this is the case.

Case 1 and Case 3 exhibit significantly different fuel distributions within the cavity despite having the same global equivalence ratio. This highlights the impact injector configuration and fuel injection location can have on the fuel distribution and the resulting temperatures that are observed in the cavity. The observed differences in fuel distribution are consistent with the earlier observation that the location of greatest heat release in the cavity occurs at lower x-positions in Case 3 compared to the other cases (as indicated by the temperature contour plots).

A correlation between measured relative fuel concentration and measured temperature at a single measurement location is depicted in Fig. 4.28. These measurements were recorded for Case 2 at position 2.4. CARS spectra here were acquired at 32 ps. From this figure, it is evident that the fit temperatures tend to decrease with increasing relative fuel concentration at this location. This explains why Case 1 observed lower temperatures upstream of the cavity leading edge than Case 3, despite their similar pressure distributions. Case 1 had more cold fuel injected at B1 and B2 than Case 3, and so lower temperatures are observed due to greater mixing between the fuel and the air.

It is worth noting that the correlation between fuel concentration and temperatures within the flame could not be established due to noise limitations. However, future investigations

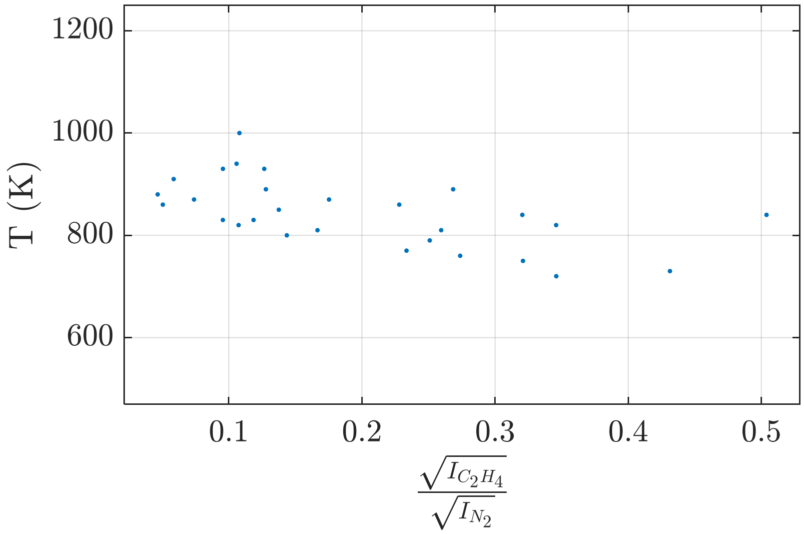

Figure 4.28: Correlation between measured relative fuel concentration and measured temperature. Data recorded at Case 2, position 2.4 with CARS spectra acquired at 32 ps.

should focus on targeted excitation of C_2H_4 during testing, allowing for more exploration of concentration-temperature relationships within the flame.

4.6 Conclusion

In conclusion, the variations in fuel injection location and global equivalence ratio have a significant impact on the temperature distribution within the combustor cavity. Less fuel injection at rows B1 and B2 results in higher temperatures near the cavity floor, and a global equivalence ratio of 0.20 corresponds to greater heat release and higher temperatures measured within the cavity compared to a global equivalence ratio of 0.32.

Temperature differences upstream of the cavity close-out ramp suggest that factors beyond global equivalence ratio, such as the pressure distribution as dictated by location of the shock train in the combustor, can influence the temperature profiles within the combustor.

These results highlight the significance of fueling conditions and injection strategies in influencing flame stabilization behavior within a scramjet combustor. Further investigations—including synchronized imaging techniques and further analysis of the data collected in this work—can enhance understanding of these phenomena and inform the optimization of scramjet engine technology.

Future work will involve developing methods to quantify local equivalence ratio from CARS spectra. Potential methods to accomplish this are discussed in the following chapter.

Chapter 5

Quantifying Local Equivalence Ratio with fs/ps CARS

5.1 Motivation and Objectives

Equivalence ratio is defined as the ratio between the fuel-to-oxidizer ratio and the stoichiometric fuel-to-oxidizer ratio, given by

$$\phi = \frac{n_{fuel}/n_{ox}}{(n_{fuel}/n_{ox})_{St}}. \tag{5.1}$$

Global equivalence ratios in the engine can be calculated from the fuel and air flow rates, but the local distribution of fuel and air cannot be discerned from the global equivalence ratio. Combustion behavior is dictated by how the fuel and air is distributed locally at various locations in the engine, or local equivalence ratios. Measurements of local equivalence ratios would provide significant insight into how fueling conditions impact combustion in a scramjet engine.

Quantitative measurements of local equivalence ratios with fs/ps CARS would be enabled by the development of a time-domain fs/ps CARS model specifically for the fuel species or by utilizing a calibration method. Both C_2H_4 and H_2 have been used as fuels in the UVaSCF scramjet facility. However, the existing spectral model used in this thesis [58, 59] does not currently include the capability to simulate the CARS response of C_2H_4 or H_2. The current model is primarily limited to diatomic molecules such as N_2 and O_2, necessitating an expansion of the model to incorporate C_2H_4 for the purpose of quantifying local equivalence ratios.

The theory for simulating the time and frequency spectral response of diatomic molecules has been previously described in literature [32, 73], but modeling of molecules such as C_2H_4 has been limited due to the computational complexity arising from the polyatomic structure of the molecule.

In this chapter, efforts to quantify local equivalence ratios with fs/ps CARS are discussed. Experimental spectra of N_2, O_2, and C_2H_4 were obtained at a distance of 2.5 mm from the exit of an in-line gas heater to compare them with a preliminary and simplified fs/ps CARS model for C_2H_4. Additionally, a calibration method, which can be used to measure local equivalence ratios in the absence of a complete CARS model, was tested for various mixtures of C_2H_4, N_2, and O_2 across a temperature range of 300 K to 500 K.

5.2 CARS Spectral Modeling of Fuel Species

5.2.1 Hydrogen (H_2)

In the case of H_2, the calculation of the molecular response function (Eq. 2.6) will allow the use of a fs/ps CARS model to measure temperature and relative concentration when H_2 is present. The theory used to calculate spectral line positions and intensities are discussed here.

For Raman transition frequencies of diatomic molecules, the vibrational energy levels can be calculated by treating the molecule as an anharmonic oscillator. The vibrational energies, denoted as $G(v)$, can be directly calculated from known molecular constants using the equation:

$$G(v) = \omega_e(v + \frac{1}{2}) - \omega_e x_e(v + \frac{1}{2})^2 + \omega_e y_e(v + \frac{1}{2})^3 - \omega_e z_e(v + \frac{1}{2})^4 + ... \tag{5.2}$$

Here, v represents the vibrational quantum number, ω_e is the first vibrational constant (harmonic frequency), and $\omega_e x_e$, $\omega_e y_e$, and $\omega_e z_e$ are additional vibrational anharmonic correction constants.

Rotational energy levels for diatomic molecules can be calculated by treating the molecule as a rigid rotor. The rotational energy, denoted as $F_v(J)$, of the rigid rotor is given by the equation:

$$F_v(J) = B_v J(J + 1) - D_v J^2(J + 1)^2, \tag{5.3}$$

where J represents the rotational quantum number, B_v is a rotational constant, and D_v is another rotational constant that accounts for centrifugal forces on the bond. The rotational constants can be expanded using known molecular constants:

$$B_v = B_e - \alpha_e(v + \frac{1}{2}) + \gamma_e(v + \frac{1}{2})^2 - ... \tag{5.4}$$

$$D_v = D_e +_e (v + \frac{1}{2}) + \delta_e(v + \frac{1}{2})^2 + ... \tag{5.5}$$

In Eq. 5.4 and Eq. 5.5, B_v and D_v are written as expansions with known molecular constants. The molecular constants used to calculate both vibrational and rotational energies for H_2 are included in Table 5.1.

Raman intensities were calculated by applying a Boltzmann distribution and utilizing

Table 5.1: Molecular constants for calculating H_2 line positions.

Constant	Value	Source
ω_e	4401.21	[74]
$\omega_e x_e$	121.33	[74]
$\omega_e y_e$	0.812	[75]
$\omega_e z_e$	0	[75]
B_e	60.853	[74]
α_e	3.062	[74]
γ_e	0.057	[75]
D_e	0.0471	[74]
β_e	-0.0027	[75]
δ_e	0.74144	[74]

Table 5.2: Molecular constants for calculating H_2 Raman intensities.

Constant	Value	Source
B_e	60.853	[74]
ω_e	4401.21	[74]
a'	0.7894	[76]
a_1	-1.6029	[62]
γ'	0.0276528	[77]
$\frac{p_1}{p_0}$	2.57712	[77]
F_{iso}	0.027	[62]
F_{aniso}	0.79	[62]

Raman cross sections based on Eq. 2.9, along with the Herman-Wallis factors described in Eq. 2.10. The constants used for these calculations can be found in Table 5.2.

The Q-branch line positions and corresponding Raman intensities for H_2 are presented using a stick diagram in Fig. 5.1. Notably, even at relatively low temperatures such as 273 K, higher level rotational states exhibit significant population. This is illustrated in Fig. 5.2, which depicts the population distribution for H_2 derived from a Boltzmann distribution at various temperatures.

Fig. 5.3 illustrates the simulated Q-branch CARS spectra of H_2 at a temperature of T = 273 K, specifically at a probe delay of 6 ps, assuming the absence of collisional broadening. In this simulation, the wavelengths of the electric fields used for pump, Stokes, and probe

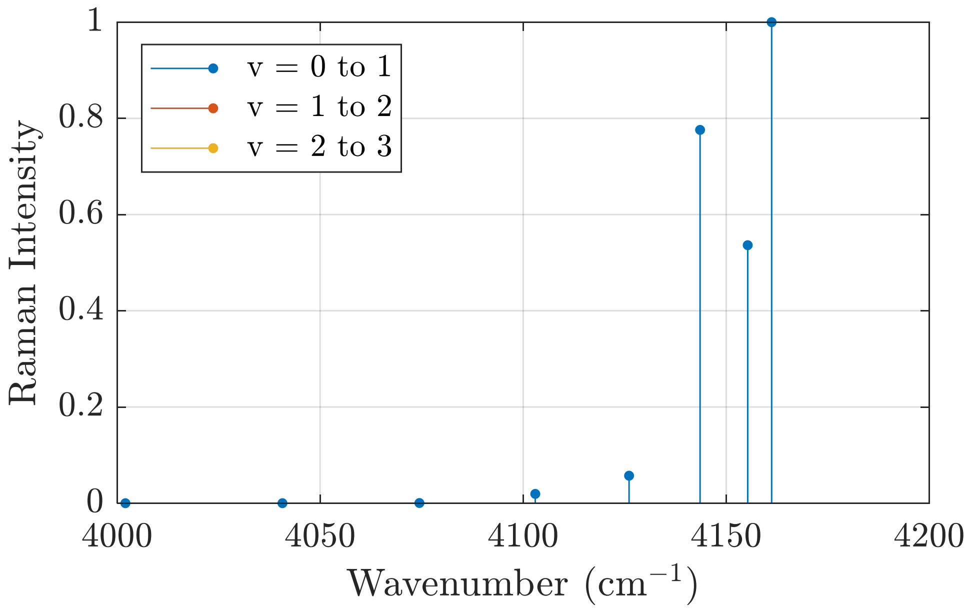

Figure 5.1: Stick diagram of Q-branch line positions and Raman intensities for H_2 at T = 273 K.

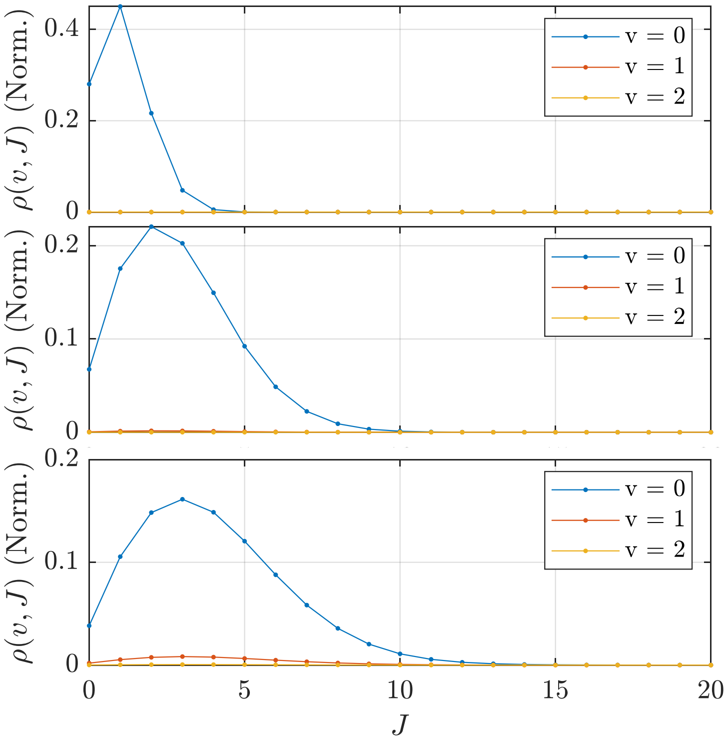

Figure 5.2: Boltzmann distributions of H_2 at three different temperatures: T = 273 K, T = 1200 K, and T = 2000 K.

are 600 nm, 800 nm, and 400 nm, respectively. The selection of a 600 nm pump wavelength aligns with the frequency of the transition $v = 0, J = 0 \rightarrow v = 1, J = 0$.

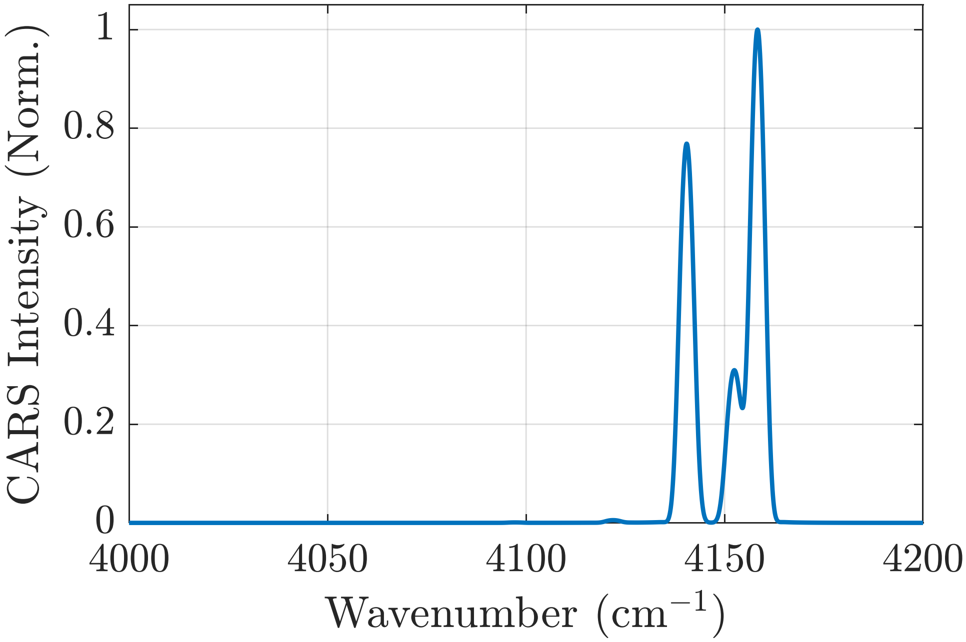

Figure 5.3: Q-branch CARS spectra of H_2. $T = 273$ K, $\tau_{probe} = 6$ ps.

A comprehensive calculation of the molecular response function for H_2 requires a collisional linewidth model, which has not yet been implemented in the current model.

5.2.2 Ethylene (C_2H_4)

The fs/ps CARS response of C_2H_4 presents challenges in simulation due to its polyatomic structure, requiring methods to reduce computational complexity and cost. Unlike diatomic molecules such as N_2 and O_2 which are commonly investigated, the simulation of C_2H_4 is more complex. C_2H_4 is an asymmetric top molecule with 12 normal modes of vibration, out of which four modes are Raman active. These modes of vibration are:

- ν_1: symmetric CH stretch
- ν_2: CC stretch
- ν_3: symmetric HCH bending

- ν_5: asymmetric CH stretch

While ν_1, ν_2, and ν_3 are polarized bands, the ν_5 band is depolarized and is not observed in CARS spectra. A band is considered depolarized if the depolarization ratio (ρ) is greater than 0.75 [78]. The depolarization ratio is determined by the ratio of peak intensities of the parallel and perpendicular components of Raman scattered light as given by the equation:

$$\rho = \frac{I_{perpendicular}}{I_{parallel}}. \tag{5.6}$$

In the case of the ν_5 band of C_2H_4, the asymmetric nature of the vibration leads to depolarization of the band since the polarization of the Raman scattered light is perpendicular to the incident electric fields [79]. As a result, the simulation of the ν_5 band can be omitted, while the Raman spectra of ν_1, ν_2, and ν_3 must be simulated to model the CARS spectra of C_2H_4 accurately.

Quantum mechanical descriptions do not provide explicit theory to represent the energy levels of an asymmetric top molecule [80], making precise calculations of rotational energy levels computationally demanding. The immense number of sub-levels ($2J + 1$) associated with each value of J further complicates accurate simulation of the molecule. Therefore, simplifying assumptions are necessary in modeling the CARS spectra of C_2H_4. Similar simplifications have been employed in previous studies on polyatomic molecules like methane (CH_4) and CO_2 to model fs/ps CARS spectra [81, 59].

Ongoing work involves the calculation of the molecular response function (Eq. 2.6) specifically for C_2H_4, and a preliminary model is currently under development. Vibrational energies for the Raman-active modes of C_2H_4 are calculated by treating each mode as an independent anharmonic oscillator, disregarding mode coupling. The vibrational energies (G) can be calculated using Eq. 5.2. To account for anharmonicity in the vibrational energies of C_2H_4, the second-order vibrational constant ($\omega_e x_e$) is calculated using known fundamental and harmonic frequencies for each vibrational mode. For the ground vibrational state, $\omega_e x_e$ is given by

$$\omega_e x_e = -\frac{\omega_0 - \omega_e}{2}, \tag{5.7}$$

where ω_0 is the fundamental frequency and ω_e is the harmonic frequency. The fundamental and harmonic frequencies for the Raman-active vibrational modes of C_2H_4 are extracted from Ref. [82], as shown in Table 5.3. From these values, the $\omega_e x_e$ values for these modes can be calculated, and these values are also presented in Table 5.3.

Table 5.3: Vibrational constants for calculating C_2H_4 energy levels.

Constant	ν_1	ν_2	ν_3
ω_0	3022.03	1625.40	1343.54
ω_e	3153	1655	1370
$\omega_e x_e$	65.485	14.800	13.230

The vibrational energy levels of C_2H_4 accounting for anharmonicity were calculated by considering each vibrational mode as an independent anharmonic oscillator. Based on the calculated values of $\omega_e x_e$ for each mode, the vibrational energy levels were determined. The energy level diagram depicting these vibrational energy levels is shown in Fig. 5.4.

Raman shifts for Q-branch transitions at J = 0 were calculated using Eq. 2.7. Ongoing work towards complete model development involves the calculation of rovibrational energies for each vibrational mode of C_2H_4. The determination of these energies is crucial for accurately modeling the Raman transition frequencies. To assess the temperature-dependent portion of the Raman transition intensities, the population distribution of the molecular energy levels was calculated using a Boltzmann distribution.

To accurately determine the temperature and relative concentration, it is necessary to determine the molecular constants for C_2H_4 that are used in the calculation of Raman cross sections (Eq. 2.9). In the current work, relative Raman cross-sections with respect to N_2 for

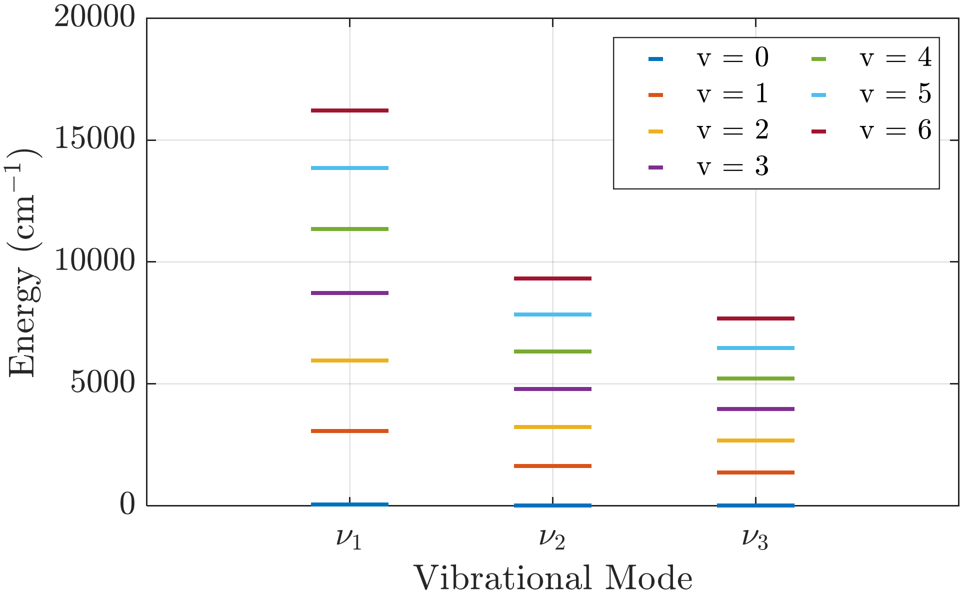

Figure 5.4: Energy level diagram accounting for zero-point energy for ν_1, ν_2, and ν_3 modes of C_2H_4 from v = 0 to v = 6.

the different Raman-active vibrational modes of C_2H_4 were obtained from Ref. [83]. These relative cross section values are listed in Table 5.4.

Table 5.4: Raman cross sections relative to N_2 for the Raman-active vibrational modes of Ethylene.

Wavenumber	$(\frac{\partial\sigma}{\partial\Omega})$
3020	6.4
1623	2.1
1342	2.8

Finally, a Gaussian lineshape was convolved with the calculated transition line positions to estimate the Raman spectra of C_2H_4. This approach was used as a substitute for a collisionally-broadened linewidth model. A sample of the simulated spectra, specifically for a temperature of 1100 K, is depicted in Fig. 5.5.

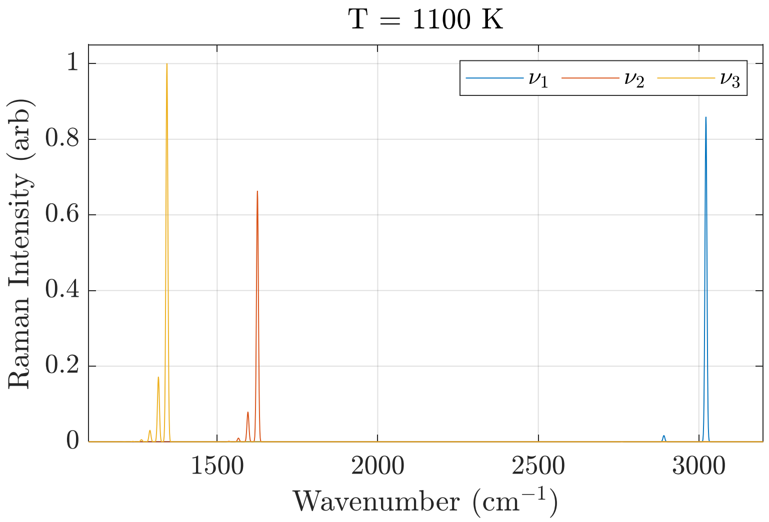

Figure 5.5: Simulated Raman spectrum of ν_1, ν_2, and ν_3 modes of C_2H_4 at T = 1100 K.

5.3 Calibration Method

An alternative approach for measuring relative species concentration in the absence of a fully developed fs/ps CARS time-domain model is a calibration method. In a previous study, a quasi-calibration method was employed to determine the concentration of ethylene using ns CARS [30]. This method is currently being considered for quantifying fuel/air ratios based on acquired fs/ps CARS spectra.

Engel et al. [34] and Brauer and Leipertz [84] have demonstrated that mole fractions can be directly extracted from CARS spectra by relating the measured CARS signal intensity to the number density in the measurement volume. The CARS signal intensity is proportional to the square of the number density and is related by the following expression:

$$N_i^2 \propto \frac{I_{CARS}}{A_i I_{NR} \left(\frac{\partial\sigma}{\partial\Omega}\right)_i^2}, \tag{5.8}$$

where A_i is an experimental constant, I_{NR} is the non-resonant CARS intensity, and $\left(\frac{\partial\sigma}{\partial\Omega}\right)_i$ is the relative Raman cross section of the molecule of interest. The mole fraction of a gas component is then given by

$$\chi_i = \frac{N_i}{\sum_i N_i}. \tag{5.9}$$

Thus, for a binary mixture of C_2H_4, N_2, and O_2, the mole fraction of C_2H_4 can be calculated as

$$\chi_{C_2H_4} = \frac{N_{C_2H_4}}{N_{C_2H_4} + N_{N_2} + N_{O_2}}. \tag{5.10}$$

The mole fraction can be directly related to the CARS signal intensity using the equation:

$$\chi_{C_2H_4} = \frac{\frac{\sqrt{I_{CARS}(C_2H_4)}}{\sqrt{I_{NR}(C_2H_4)}}}{\frac{\sqrt{I_{CARS}(C_2H_4)}}{\sqrt{I_{NR}(C_2H_4)}} + \frac{1}{K}\left[\frac{\sqrt{I_{CARS}(N_2)}}{\sqrt{I_{NR}(N_2)}} + \frac{\sqrt{I_{CARS}(O_2)}}{\sqrt{I_{NR}(O_2)}}\right]}, \tag{5.11}$$

where K is a constant that includes all quantities not dependent on temperature or gas composition. The value of K can be determined by fitting the equation for various temperatures, generating a calibration curve. This curve can then be utilized to extract measurements of relative species concentration from CARS spectra for a known temperature.

5.4 Experimental Setup

The CARS optical setup utilized in this chapter is depicted in Fig. 5.6. This configuration is similar to the general experimental setup for vibrational CARS described in Chapter 2.2. The pump beam was tuned to 660 nm and 700 nm to target N_2, O_2, and the various modes of C_2H_4 simultaneously. A 4f-pulse shaper was employed to generate a ps probe. The gas temperature was measured using a thermocouple placed 4.5 mm from the exit of the gas cell heater. The gas was heated using a custom-built in-line gas cell heater built in the laboratory.

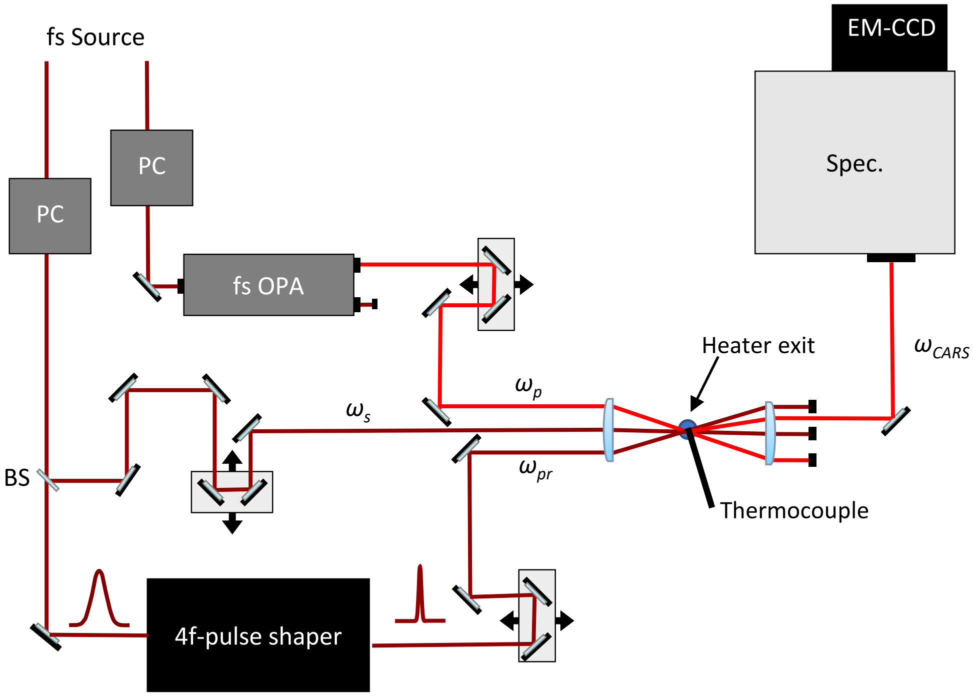

Figure 5.6: CARS optical layout used to acquire spectra of heated mixtures of ethylene and air.

The flow rates used in the experiment are presented in Table 5.5. The mole fractions of the gas mixture were determined based on the mass flow controllers (MFCs) by converting the flow rates from standard liters per minute (SLPM) to molar flow rates (mol/s).

Table 5.5: Flow rates used and corresponding concentration of C_2H_4.

C_2H_4 (SLPM)	Air (SLPM)	$\chi(C_2H_4)$
0.25	4.75	0.05
0.5	4.5	0.10
0.75	4.25	0.15
1	4	0.20
1.25	3.75	0.25

5.5 Results and Discussion

5.5.1 Preliminary Model Validation

The experimental spectra of ethylene/air mixtures were collected to investigate the effect of temperature and species concentration on the spectral features related to C_2H_4, O_2, and N_2. To study the temperature response, a heated gas jet was utilized. A sample of these spectra at two temperatures, T = 300 K and T = 500 K, is shown in Fig. 5.7(A).

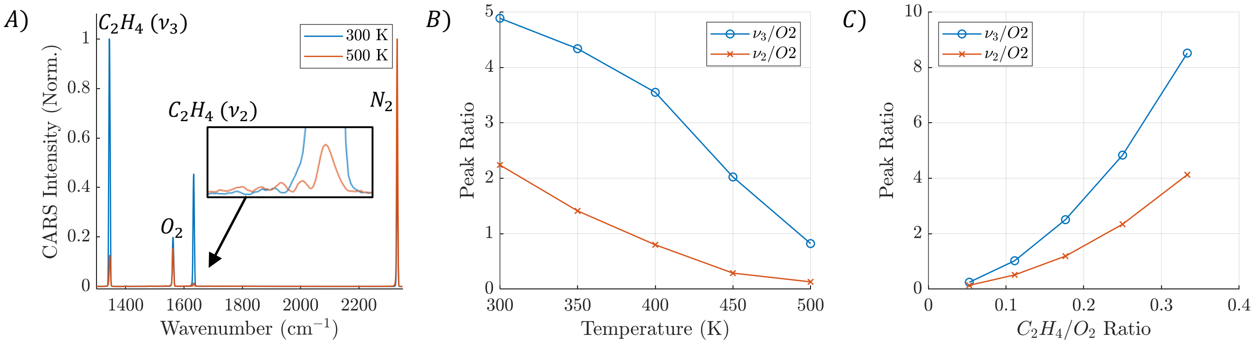

Figure 5.7: A) CARS spectra obtained at 300 K (blue) and 500 K (red) for a mixture consisting of 20% ethylene and 80% air. The spectra demonstrate how the spectral features change with temperature (B) and species concentration (C).

The experimental data shows the presence of spectral features corresponding to higher level rotational states in the ν_2 band of C_2H_4 even at relatively low temperatures. This observation suggests that C_2H_4 exhibits greater sensitivity to temperature compared to molecules like N_2, where such features are not observed. This behavior must be accurately incorporated into the model to ensure accurate temperature measurements using C_2H_4 CARS.

In Fig. 5.7(B), the response of the peak ratio of C_2H_4 features to changes in temperature is shown. This figure illustrates how the relative intensities of the C_2H_4 peaks vary with temperature. Fig. 5.7(C) displays the response of the peak ratio of C_2H_4 features to changes in the C_2H_4/O_2 composition.

These figures indicate that not only the relative species concentration but also the temperature influence the differences in CARS signal intensity between the C_2H_4 features. Accurate modeling of the temperature dependence of these features is necessary and will be pursued to complete the C_2H_4 model and enable measurements of local equivalence ratios using CARS spectra.

The preliminary model for C_2H_4 was compared with low-temperature experimental spectra, as shown in Fig. 5.8, to validate the spectral line positions. Although there are minor discrepancies in the line positions, there is a significant discrepancy in the CARS intensity.

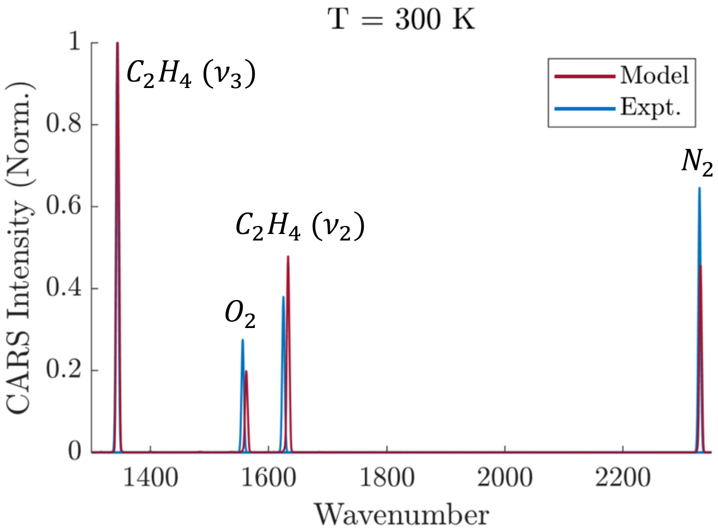

Figure 5.8: A comparison of the fs/ps CARS model (red) and experimental measurements (blue) at 300 K.

To improve the accuracy of the CARS model for C_2H_4, several additional calculations and considerations need to be addressed. One important aspect is the calculation of Placzek-Teller coefficients and Herman-Wallis factors for each vibrational mode of C_2H_4, which are used in Eq. 2.9 to calculate Raman cross sections. These factors must be determined in order to accurately estimate the intensity of the CARS signal.

Future work should focus on calculating these coefficients and factors to fully simulate C_2H_4 fs/ps CARS spectra over the entire temperature range of interest. Additionally, a more comprehensive calculation of energy levels, including higher rotational states, is necessary to complete the model. This is important because the experimental spectra show evidence of higher-level rotational states in the ν_2 band of C_2H_4 at low temperatures. Incorporating these higher-level states into the model will improve its accuracy and allow for more reliable temperature measurements using C_2H_4 CARS.

5.5.2 Low Temperature Calibration for Measuring Local Equivalence Ratio

A calibration curve was generated to measure mole fractions in mixtures of C_2H_4 and air. The curve was created by acquiring CARS spectra in the gas cell heater at temperatures ranging from 300 K to 500 K. The concentrations of C_2H_4 in the mixtures varied from 5% to 25%.

Two sample CARS spectra acquired at 300 K were shown in Fig. 5.9. Both spectra shown here are normalized to the Nitrogen feature. The red line corresponds to a C_2H_4 mole fraction of 0.25, indicating a higher concentration of C_2H_4 in the mixture. The blue line corresponds to a C_2H_4 mole fraction of 0.05, representing a lower concentration.

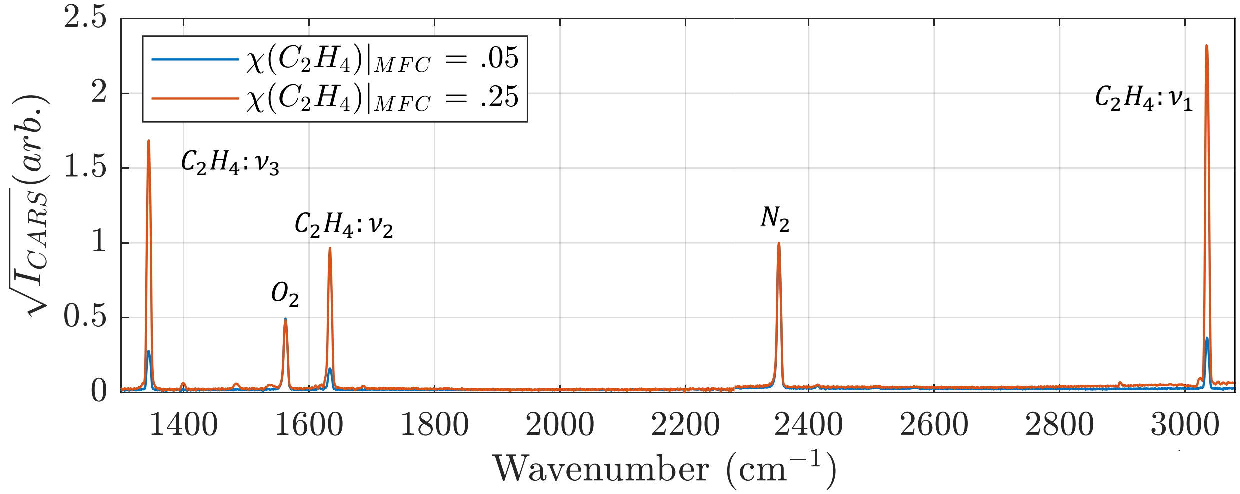

Figure 5.9: Experimental CARS spectra of a mixture of Ethylene and air. Both spectra are normalized to Nitrogen.

Table 5.6 displays the measured mole fractions of C_2H_4 using the calibration method. The ν_1 band of C_2H_4 was used to measure these mole fractions at various temperatures ranging from 300 K to 500 K in 50 K increments. The mole fractions correspond to different concentrations of C_2H_4 (0.05, 0.10, 0.15, 0.20, and 0.25).

Table 5.6: Measured mole fraction of C_2H_4 using the constant K determined from the ν_1 band of C_2H_4. Measurements are shown for T = 300 K to 500 K in increments of 50 K.

Temp. (K)	0.05	0.10	0.15	0.20	0.25
300	0.0484	0.0991	0.1491	0.2006	0.2514
350	0.0534	0.0996	0.1539	0.1928	0.2527
400	0.0469	0.1005	0.1494	0.2016	0.2492
450	0.0474	0.0885	0.1408	0.1991	0.2596
500	0.0456	0.0901	0.1486	0.2002	0.2558

The constant K in Eq. 5.11 was determined by employing a fitting routine to minimize the discrepancy between the measured C_2H_4 mole fractions obtained from CARS and the mole fractions derived from the mass flow controllers. Table 5.7 presents the values of K obtained at different temperatures.

Table 5.7: Values for K found for 300 K to 500 K for the ν_1 band of C_2H_4.

Temperature (K)	K (const.)
300	0.0738
350	0.0802
400	0.1010
450	0.1515
500	0.2605

Figure 5.10 illustrates the measured mole fractions of C_2H_4 plotted against the mole fractions determined from the mass flow controllers at each temperature. The figure includes a line of best fit that represents the relationship between the measured mole fractions and the known mole fractions. These results serve to demonstrate the process of calibrating and validating the measurement of C_2H_4 mole fractions using the constant K found for the ν_1 band of C_2H_4. This method can be performed for each band of C_2H_4 observed. Accurate

calibration of the constant K as a function of temperature will allow for the determination of accurate C_2H_4 mole fractions based on CARS spectra.

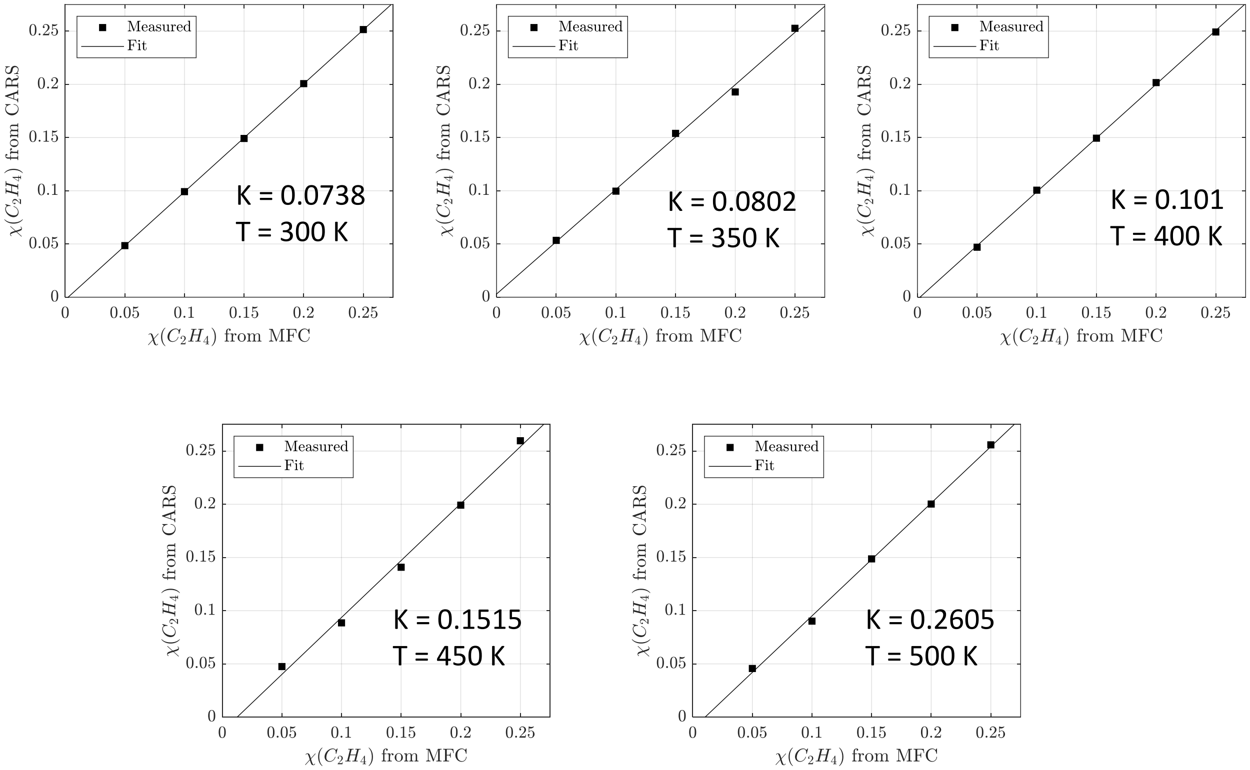

Figure 5.10: Measured mole fractions of C_2H_4 obtained from the ν_1 band of C_2H_4 are plotted as a function of mole fraction determined from the mass flow controller. The trend line represents the relationship between the measured mole fractions and the known mole fractions.

Figure 5.11 depicts the values of the constant K plotted against temperature and a polynomial curve fit to the data. The curve fit was generated using a MATLAB polynomial fitting routine. It is important to note that this curve fit is specifically applicable when utilizing the ν_1 band of C_2H_4 for extracting mole fractions from CARS spectra. The curve provides a mathematical representation of the relationship between the constant K and temperature, aiding in the accurate determination of C_2H_4 mole fractions based on CARS measurements involving the ν_1 band of C_2H_4.

Figure 5.12 displays the measured mole fractions obtained from CARS using both the ν_2 and ν_3 bands of C_2H_4 at T = 300 K, along with a trend line representing the mole fraction

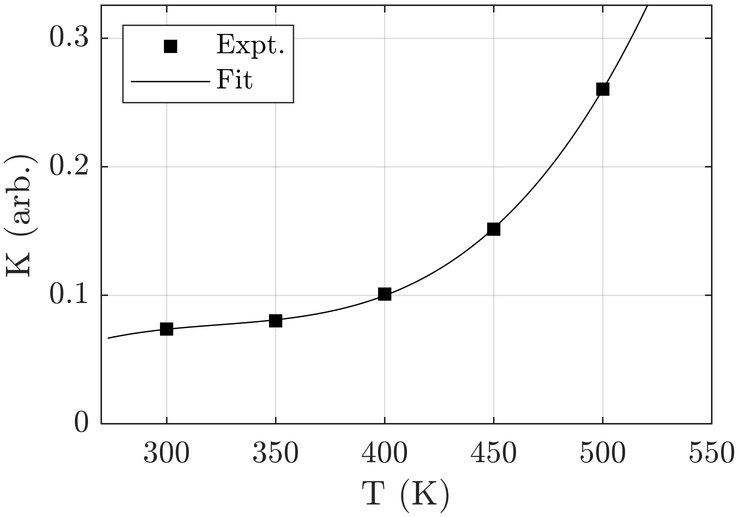

Figure 5.11: Calibration curve generated from values of K found from T = 300 K to 500 K.

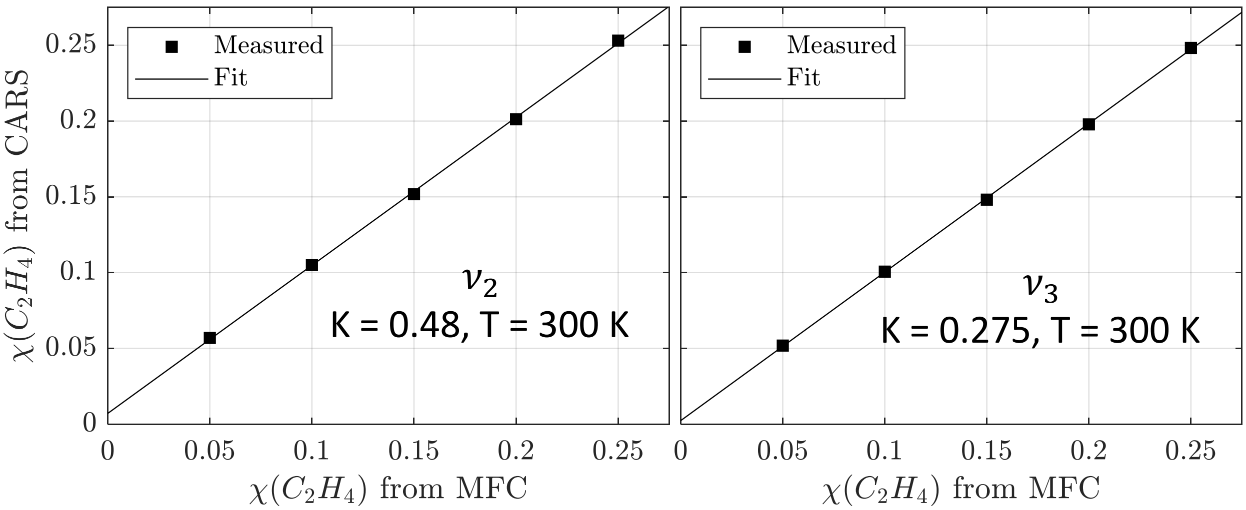

Figure 5.12: Measured mole fractions of C_2H_4 from the ν_2 and ν_3 bands of C_2H_4, and trend line as a function of mole fraction determined from mass flow controller.

determined from the mass flow controllers. Table 5.8 presents the measured mole fractions of C_2H_4 at T = 300 K that were obtained from CARS using the three Raman active vibrational modes of C_2H_4, namely, ν_1, ν_2, and ν_3.

The comparison between the measured mole fractions of C_2H4 obtained from CARS and the mole fractions calculated from mass flow rates show good agreement overall for all three

Table 5.8: Measured mole fraction of C_2H_4 for T = 300 K for each band of C_2H_4.

$\chi(C_2H_4)\vert_{MFC} =$	0.05	0.10	0.15	0.20	0.25
$\chi(C_2H_4)\vert_{CARS}$: ν_1	0.0484	0.0991	0.1491	0.2006	0.2514
$\chi(C_2H_4)\vert_{CARS}$: ν_2	0.0568	0.1051	0.1518	0.2012	0.2531
$\chi(C_2H_4)\vert_{CARS}$: ν_3	0.0518	0.1006	0.1481	0.1978	0.2483

modes of C_2H4, indicating accurate fitting of the calibration parameter K for all three modes. However, there is a slight decrease in accuracy observed in the mole fraction measured with CARS at a gas mixture of $\chi(C_2H_4)|MFC = 0.05$. This discrepancy is likely attributed to the limitated accuracy of the mass flow controller to regulate lower flow rates, considering that the flow rate used in the experiment was 0.25 SLPM. It is important to note this limitation when interpreting the CARS measurements at lower mole fractions of C_2H_4.

5.6 Conclusion

In conclusion, this chapter addressed the need for a method to quantify local equivalence ratios in the UVaSCF. Two main approaches were discussed: developing a fs/ps CARS model for the fuel species of interest and implementing a calibration method.

Experimental spectra of N_2, O_2, and C_2H_4 were obtained near the exit of a gas heater. These measurements served two purposes: validating a preliminary fs/ps CARS model specifically for C_2H_4 and demonstrating a calibration technique to extract quantitative measurements of species concentration using CARS.

The validation of the preliminary model for C_2H_4 involved comparing it with low-temperature experimental spectra. While there were minor discrepancies in the line positions, a significant discrepancy was observed in the CARS intensity.

Additional work is required to complete the molecular response function for C_2H_4 and H_2, taking into account collisional broadening effects. Additionally, a calibration at the temperatures expected in the UVaSCF needs to be performed in order to accurately quantify local equivalence ratios using this method.

Chapter 6

Summary and Future Work

6.1 Summary

In this thesis, a novel counter-propagating beam configuration for fs/ps CARS was developed to achieve spatial resolution of 15.52 µm. The size of the measurement region was demonstrated to depend on the pulse width, which can be adjusted using the post-amplification pulse compressor. Additionally, the location of the CARS probe volume could be adjusted by varying only the temporal overlap between the excitation pulses. The counter-propagating fs/ps CARS system was used to successfully resolve the temperature profile within a microscale sonic gas jet with a measured FWHM of 66 µm, highlighting its ability to resolve microscale variations in temperature.

These results demonstrate the impact and the potential of fs/ps CoPCARS for various applications requiring precise spatial resolution. This technique can be applied to environments with steep gradients where conventional phase matching schemes would result in significant spatial averaging due to larger probe volumes. A significant impact of this work is that microscale spatial resolution can be achieved with a compact experimental setup (low crossing angles), enabling the integration of a high-resolution fs/ps CARS system in test facilities with limited optical access and spatial limitations.

Furthermore, a fs/ps CARS system using traditional BOXCARS phase-matching was successfully implemented in the UVaSCF model scramjet to quantify temperatures throughout the combustor, including the flameholding cavity, without the use of window standoffs. This allowed for mapping temperatures at different test conditions investigating changes in global equivalence ratio and fuel injection location. Local temperature measurements revealed differences between test cases that were not resolvable using wall pressure measurements. These in-situ measurements enable investigation of flame stabilization behavior in a supersonic flow that cannot be performed with wall instrumentation.

The integration of a fs/ps CARS system into the UVaSCF has laid the groundwork for future measurement campaigns in the facility to investigate flame stability in a scramjet engine. Extensive measurements of properties throughout the combustor can be taken for various operating conditions to generate an experimental database for validation of numerical simulations. fs/ps CARS can also be used to provide inlet conditions for CFD simulations for a variety of operating conditions.

A CARS spectral model for C_2H_4 is under development to enable quantitative measurements of local equivalence ratio with fs/ps CARS in the UVaSCF. Comparisons of C_2H_4 line positions calculated in the model were compared to experimentally acquired C_2H_4 CARS spectra. Additionally, a calibration method to measure C_2H_4-air ratios from fs/ps CARS spectra was tested at low temperatures (T = 300 K to T = 500 K), and can be pursued as an alternative to the CARS spectral model.

6.2 Future Work

In the future, the counter-propagating phase-matching configuration could be implemented for measurements in a turbulent flame, taking advantage of its capability to characterize gradients in a reacting flow. To enable time-resolved measurements, a high-energy probe such as an SHBC or a standalone ps laser amplifier would be necessary due to the small size of the probe volume resulting from the two counter-propagating fs pulses.

In the UVaSCF, future work should focus on further analysis of the test results discussed in Chapter 4 and further investigations of flame stabilization behavior. Schlieren imaging can provide insights into changes in shock structures within the combustor, which may explain variations in fuel distribution under similar global equivalence ratios.

Additionally, finer mapping of the cavity can be achieved using 0D-CARS to characterize temperature gradients across the shear layer above the cavity. Alternatively, implementing a 1-dimensional fs/ps CARS system in the UVaSCF could improve the resolution of gradients in the flow. Complete characterization of the inlet conditions for each test case should be performed for use in numerical flow simulations. Additional investigation of the correlation between fuel concentration and temperatures in the engine can be achieved by targeting the C_2H_4 Raman frequency more efficiently.

The computation of the full molecular response function for C_2H_4 must be completed to enable the direct quantitative measurement of local equivalence ratio using fs/ps CARS. This involves calculating the Placzek-Teller coefficients and Herman-Wallis factors, as well as including higher rotational states in the energy level calculations for C_2H_4. These improvements will lead to more accurate calculation of C_2H_4 fs/ps CARS spectra. Alternatively, a calibration at higher temperatures can be performed in the UVaSCF to enable quantitative measurements in the absence of a full spectral model.

Bibliography

[1] W. Heiser, D. Pratt, D. Daley, and U. Mehta, *Hypersonic Airbreathing Propulsion.* American Institute of Aeronautics and Astronautics, Inc., 1 1994.

[2] G. Dugger, A. I. of Aeronautics, and Astronautics, *Ramjets.* AIAA selected reprint series, American Institute of Aeronautics and Astronautics, 1969.

[3] C. Segal, *The Scramjet Engine.* Cambridge University Press, 2009.

[4] D. J. Micka, D. A. Knaus, J. Temme, and J. F. Driscoll, "Passive optical combustion sensors for scramjet engine control," American Institute of Aeronautics and Astronautics, 7 2015.

[5] S. kyun Im and H. Do, "Unstart phenomena induced by flow choking in scramjet inlet-isolators," *Progress in Aerospace Sciences*, vol. 97, pp. 1–21, 2 2018.

[6] Q. Liu, D. Baccarella, and T. Lee, "Review of combustion stabilization for hypersonic airbreathing propulsion," *Progress in Aerospace Sciences*, vol. 119, p. 100636, 11 2020.

[7] D. J. Micka and J. F. Driscoll, "Combustion characteristics of a dual-mode scramjet combustor with cavity flameholder," *Proceedings of the Combustion Institute*, vol. 32, pp. 2397–2404, 2009.

[8] A. Ben-Yakar and R. K. Hanson, "Cavity flame-holders for ignition and flame stabilization in scramjets: An overview," *Journal of Propulsion and Power*, vol. 17, pp. 869–877, 7 2001.

[9] V. A. Vinogradov, S. A. Kobigsky, and M. D. Petrov, "Experimental investigation of kerosene fuel combustion in supersonic flow," *Journal of Propulsion and Power*, vol. 11, pp. 130–134, 1 1995.

[10] P. Ortwerth, A. Mathur, V. Vinogradov, V. Grin, M. Goldfeld, and A. Starov, "Experimental and numerical investigation of hydrogen and ethylene combustion in a mach 3-5 channel with a single injector," in *32nd Joint Propulsion Conference and Exhibit*, p. 3245, 1996.

[11] M. G. Owens, S. Tehranian, C. Segal, and V. A. Vinogradov, "Flame-holding configurations for kerosene combustion in a mach 1.8 airflow," *Journal of Propulsion and Power*, vol. 14, no. 4, pp. 456–461, 1998.

[12] L. Ma, Q. Lei, Y. Wu, W. Xu, T. M. Ombrello, and C. D. Carter, "From ignition to stable combustion in a cavity flameholder studied via 3d tomographic chemiluminescence at 20 khz," *Combustion and Flame*, vol. 165, pp. 1–10, 3 2016.

[13] L. M. L. Cantu, E. C. A. Gallo, A. D. Cutler, P. M. Danehy, R. D. Rockwell, C. T. Johansen, C. P. Goyne, and J. C. McDaniel, "Oh plif visualization of a premixed ethylene-fueled dual-mode scramjet combustor," American Institute of Aeronautics and Astronautics, 1 2016.

[14] C. T. Johansen, C. D. McRae, P. M. Danehy, E. C. A. Gallo, L. M. L. Cantu, G. Magnotti, A. D. Cutler, R. D. Rockwell, C. P. Goyne, and J. C. McDaniel, "Oh plif visualization of the uva supersonic combustion experiment: configuration a," *Journal of Visualization*, vol. 17, pp. 131–141, 5 2014.

[15] L. M. L. Cantu, E. C. A. Gallo, A. D. Cutler, B. F. Bathel, P. M. Danehy, R. D. Rockwell, C. P. Goyne, and J. C. McDaniel, "Visualization of simulated fuel–air mixing in a dual-mode scramjet," *Journal of Propulsion and Power*, vol. 32, pp. 373–382, 3 2016.

[16] J. D. Miller, S. J. Peltier, M. N. Slipchenko, J. G. Mance, T. M. Ombrello, J. R. Gord, and C. D. Carter, "Investigation of transient ignition processes in a model scramjet pilot cavity using simultaneous 100 khz formaldehyde planar laser-induced fluorescence and ch* chemiluminescence imaging," *Proceedings of the Combustion Institute*, vol. 36, pp. 2865–2872, 2017.

[17] K.-C. Lin, M. Ryan, C. Carter, M. Gruber, and C. Raffoul, "Raman scattering measurements of gaseous ethylene jets in a mach 2 supersonic crossflow," *Journal of Propulsion and Power*, vol. 26, pp. 503–513, 5 2010.

[18] N. R. Grady, R. W. Pitz, C. D. Carter, and K.-Y. Hsu, "Raman scattering measurements of mixing and finite-rate chemistry in a supersonic reacting flow over a piloted, ramped cavity," *Combustion and Flame*, vol. 165, pp. 310–320, 3 2016.

[19] B. McGann, T. Lee, T. Ombrello, C. D. Carter, S. D. Hammack, and H. Do, "Inlet distortion effects on fuel distribution and ignition in scramjet cavity flameholder," *Journal of Propulsion and Power*, vol. 35, pp. 601–613, 5 2019.

[20] T. Ombrello, N. S. Okhovat, and M. R. Rhoby, "Measurements of scramjet fueling conditions," American Institute of Aeronautics and Astronautics, 1 2018.

[21] R. Spearrin, C. Goldenstein, I. Schultz, J. Jeffries, and R. Hanson, "Simultaneous sensing of temperature, co, and co2 in a scramjet combustor using quantum cascade laser absorption spectroscopy," *Applied Physics B*, vol. 117, no. 2, pp. 689–698, 2014.

[22] M. R. Rhoby, N. S. Okhovat, A. Kerst, K. C. Gross, and T. Ombrello, "Preliminary investigation of scramjet fueling flowfield with hyperspectral imaging," American Institute of Aeronautics and Astronautics, 7 2017.

[23] A. C. Eckbreth, *Laser Diagnostics for Combustion Temperature and Species.* CRC Press, 1996.

[24] A. C. Eckbreth and T. J. Anderson, "Dual broadband cars for simultaneous, multiple species measurements," *Applied optics*, vol. 24, no. 16, pp. 2731–2736, 1985.

[25] S. P. Kearney, "Hybrid fs/ps rotational cars temperature and oxygen measurements in the product gases of canonical flat flames," *Combustion and Flame*, vol. 162, pp. 1748–1758, 5 2015.

[26] D. R. Richardson, S. P. Kearney, and D. R. Guildenbecher, "Post-detonation fireball thermometry via femtosecond-picosecond coherent anti-stokes raman scattering (cars)," *Proceedings of the Combustion Institute*, vol. 38, pp. 1657–1664, 2021.

[27] K. A. Vereschagin, V. V. Smirnov, O. M. Stelmakh, V. I. Fabelinsky, V. A. Sabelnikov, V. V. Ivanov, W. Clauss, and M. Oschwald, "Temperature measurements by coherent anti-stokes raman spectroscopy in hydrogen-fuelled scramjet combustor," *Aerospace Science and Technology*, vol. 5, pp. 347–355, 7 2001.

[28] S. O'Byrne, P. M. Danehy, S. A. Tedder, and A. D. Cutler, "Dual-pump coherent anti-stokes raman scattering measurements in a supersonic combustor," *AIAA Journal*, vol. 45, pp. 922–933, 4 2007.

[29] A. D. Cutler, G. Magnotti, L. Cantu, E. Gallo, R. Rockwell, and C. Goyne, "Dual-pump coherent anti-stokes raman spectroscopy measurements in a dual-mode scramjet," *Journal of Propulsion and Power*, vol. 30, pp. 539–549, 5 2014.

[30] A. D. Cutler, E. C. Gallo, L. M. Cantu, R. D. Rockwell, and C. P. Goyne, "Coherent anti-stokes raman spectroscopy of a premixed ethylene–air flame in a dual-mode scramjet," *Combustion and Flame*, vol. 189, pp. 92–105, 3 2018.

[31] J. D. Miller, M. N. Slipchenko, T. R. Meyer, H. U. Stauffer, and J. R. Gord, "Hybrid femtosecond/picosecond coherent anti-stokes raman scattering for high-speed gas-phase thermometry," *Optics Letters*, vol. 35, p. 2430, 7 2010.

[32] J. D. Miller, S. Roy, M. N. Slipchenko, J. R. Gord, and T. R. Meyer, "Single-shot gas-phase thermometry using pure-rotational hybrid femtosecond/picosecond coherent anti-Stokes Raman scattering," *Optics Express*, vol. 19, no. 16, pp. 15627–15640, 2011.

[33] S. M. Alberts, R. J. Thompson, H. K. Chelliah, and C. E. Dedic, "Temperature and species measurements of counterflow flames using coherent anti-stokes raman scattering," American Institute of Aeronautics and Astronautics, 1 2022.

[34] S. R. Engel, J. D. Miller, C. E. Dedic, T. Seeger, A. Leipertz, and T. R. Meyer, "Hybrid femtosecond/picosecond coherent anti-stokes raman scattering for high-speed ch ¡sub¿4¡/sub¿ /n ¡sub¿2¡/sub¿ measurements in binary gas mixtures," *Journal of Raman Spectroscopy*, vol. 44, pp. 1336–1343, 10 2013.

[35] B. D. Prince, A. Chakraborty, B. M. Prince, and H. U. Stauffer, “Development of simultaneous frequency- and time-resolved coherent anti-stokes raman scattering for ultrafast detection of molecular raman spectra,” *The Journal of Chemical Physics*, vol. 125, p. 044502, 7.

[36] S. Roy, J. R. Gord, and A. K. Patnaik, “Recent advances in coherent anti-stokes raman scattering spectroscopy: Fundamental developments and applications in reacting flows,” *Progress in Energy and Combustion Science*, vol. 36, pp. 280–306, 4 2010.

[37] J. Y. Zhu and D. Dunn-Rankin, “Cars thermometry in high temperature gradients,” *Applied Physics B Photophysics and Laser Chemistry*, vol. 56, pp. 47–55, 1 1993.

[38] P. Magre, P. Moreau, G. Collin, R. Borghi, and M. Péalat, “Further studies by cars of premixed turbulent combustion in a high velocity flow,” *Combustion and Flame*, vol. 71, pp. 147–168, 2 1988.

[39] T. Parameswaran and D. R. Snelling, “Estimation of spatial averaging of temperatures from coherent anti-stokes raman spectroscopy,” *Applied Optics*, vol. 35, p. 5461, 9 1996.

[40] T. Seeger, M. C. Weikl, F. Beyrau, and A. Leipertz, “Identification of spatial averaging effects in vibrational cars spectra,” *Journal of Raman Spectroscopy*, vol. 37, pp. 641–646, 6 2006.

[41] A. Montello, M. Nishihara, J. W. Rich, I. V. Adamovich, and W. R. Lempert, “Picosecond cars measurements of nitrogen rotational/translational and vibrational temperature in a nonequilibrium mach 5 flow,” *Experiments in Fluids*, vol. 54, p. 1422, 1 2013.

[42] C. E. Dedic, J. B. Michael, and T. R. Meyer, “Investigation of energy distributions behind a microscale gas-phase detonation tube using hybrid fs/ps coherent anti-stokes raman scattering,” American Institute of Aeronautics and Astronautics, 1 2017.

[43] D. Romanov, A. Filin, R. Compton, and R. Levis, “Phase matching in femtosecond boxcars,” *Optics Letters*, vol. 32, p. 3161, 11 2007.

[44] A. Bohlin, E. Nordström, H. Carlsson, X.-S. Bai, and P.-E. Bengtsson, “Pure rotational cars measurements of temperature and relative o2-concentration in a low swirl turbulent premixed flame,” *Proceedings of the Combustion Institute*, vol. 34, pp. 3629–3636, 1 2013.

[45] J. A. Shirley, R. J. Hall, and A. C. Eckbreth, “Folded boxcars for rotational raman studies,” *Optics Letters*, vol. 5, p. 380, 9 1980.

[46] D. A. Greenhalgh, “Comments on the use of boxcars for gas-phase cars spectroscopy,” *Journal of Raman Spectroscopy*, vol. 14, pp. 150–153, 6 1983.

[47] S. Chandra, A. Compaan, and E. Wiener-Avnear, “Phase matching in coherent anti-stokes raman scattering,” *Journal of Raman Spectroscopy*, vol. 10, pp. 103–105, 1 1981.

[48] A. Compaan and S. Chandra, “Coherent anti-stokes raman scattering with counter-propagating laser beams,” *Optics Letters*, vol. 4, p. 170, 6 1979.

[49] G. Laufer and R. Miles, “Angularly resolved coherent raman spectroscopy (arcs),” *Optics Communications*, vol. 28, pp. 250–254, 2 1979.

[50] C. J. Kliewer, “High-spatial-resolution one-dimensional rotational coherent anti-stokes raman spectroscopy imaging using counterpropagating beams,” *Optics Letters*, vol. 37, p. 229, 1 2012.

[51] H. Kobayashi, T. Kawahata, K. Seyama, T. Fujimari, and J.-S. Kim, “Relationship between the smallest scale of flame wrinkles and turbulence characteristics of high-pressure, high-temperature turbulent premixed flames,” *Proceedings of the Combustion Institute*, vol. 29, pp. 1793–1800, 1 2002.

[52] C. Geipel, *High-Spatial-Resolution Laser Diagnostics for a Dual-Mode Scramjet.* PhD thesis, University of Virginia, 2020.

[53] A. C. Eckbreth, “Boxcars: Crossed-beam phase-matched cars generation in gases,” *Applied Physics Letters*, vol. 32, pp. 421–423, 4 1978.

[54] J. D. Miller, M. N. Slipchenko, and T. R. Meyer, “Probe-pulse optimization for non-resonant suppression in hybrid fs/ps coherent anti-stokes raman scattering at high temperature,” *Optics Express*, vol. 19, p. 13326, 7 2011.

[55] A. M. Weiner, “Femtosecond pulse shaping using spatial light modulators,” *Review of Scientific Instruments*, vol. 71, pp. 1929–1960, 5 2000.

[56] S. P. Kearney and D. J. Scoglietti, “Hybrid femtosecond/picosecond rotational coherent anti-stokes raman scattering at flame temperatures using a second-harmonic bandwidth-compressed probe,” *Optics Letters*, vol. 38, p. 833, 3 2013.

[57] S. Laimgruber, H. Schachenmayr, B. Schmidt, W. Zinth, and P. Gilch, “A femtosecond stimulated raman spectrograph for the near ultraviolet,” *Applied Physics B*, vol. 85, pp. 557–564, 11 2006.

[58] C. E. Dedic and J. B. Michael, “Thermalization dynamics in a pulsed microwave plasma-enhanced laminar flame,” *Combustion and Flame*, vol. 227, pp. 322–334, 2021.

[59] R. J. Thompson and C. E. Dedic, “Hybrid fs/ps cars for quantifying co and co2,” American Institute of Aeronautics and Astronautics, 1 2022.

[60] R. J. Silbey, “Principles of nonlinear optical spectroscopy by shaul mukamel (university of rochester). oxford university press: new york. 1995. xviii + 543 pp. $65.00.isbn0 - 19 - 509278 - 3.,'' JournaloftheAmericanChemicalSociety, vol. 118, pp. 12872 - -12872, 11996.$

[61] C. M. Penney, R. L. S. Peters, and M. Lapp, "Absolute rotational raman cross sections for n2, o2, and co2," *Journal of the Optical Society of America*, vol. 64, p. 712, 5 1974.

[62] M. Marrocco, "Comparative analysis of herman-wallis factors for uses in coherent anti-stokes raman spectra of light molecules," *Journal of Raman Spectroscopy*, vol. 40, pp. 741–747, 7 2009.

[63] G. Placzek and E. Teller, "Die rotationsstruktur der ramanbanden mehratomiger molekle," *Zeitschrift fr Physik*, vol. 81, pp. 209–258, 3 1933.

[64] R. Gaufres and S. Sportouch, "The placzek-teller coefficients bj,kj,k for negative j," *Journal of Molecular Spectroscopy*, vol. 39, pp. 527–530, 9 1971.

[65] R. Mallipeddi and P. N. Suganthan, "Differential evolution algorithm with ensemble of parameters and mutation and crossover strategies," 2010.

[66] C. E. Dedic, "Hybrid fs/ps coherent anti-stokes raman scattering for multiparameter measurements of combustion and nonequilibrium," 2017.

[67] K. K. Ramesh, J. R. Edwards, C. P. Goyne, and J. C. McDaniel, "Large eddy simulation of high-speed, premixed ethylene combustion (invited)," American Institute of Aeronautics and Astronautics, 1 2015.

[68] P. O'Shea, M. Kimmel, X. Gu, and R. Trebino, "Highly simplified device for ultrashort-pulse measurement," *Optics Letters*, vol. 26, p. 932, 6 2001.

[69] "Auflösung einer mechanischen aufgabe.," *Journal für die reine und angewandte Mathematik (Crelles Journal)*, vol. 1826, pp. 153–157, 1 1826.

[70] R. Krauss and J. M. Jr., "A clean air continuous flow propulsion facility," American Institute of Aeronautics and Astronautics, 7 1992.

[71] W. C. Moore, A. Kim, R. J. Thompson, and C. E. Dedic, "High resolution coherent anti-stokes raman scattering to study supersonic combustion," American Institute of Aeronautics and Astronautics, 1 2022.

[72] D. Bivolaru and G. C. Herring, "Focal-plane imaging of crossed beams in nonlinear optics experiments," *Review of Scientific Instruments*, vol. 78, p. 056102, 5 2007.

[73] H. U. Stauffer, J. D. Miller, M. N. Slipchenko, T. R. Meyer, B. D. Prince, S. Roy, and J. R. Gord, "Time- and frequency-dependent model of time-resolved coherent anti-stokes raman scattering (cars) with a picosecond-duration probe pulse," *The Journal of Chemical Physics*, vol. 140, p. 024316, 1 2014.

[74] K. P. Huber and G. H. Herzberg, *NIST Chemistry WebBook, NIST Standard Reference Database Number 16,*. National Institutde of Standards and Technology.

[75] R. E. Palmer, "The carsft computer code calculating coherent anti-stokes raman spectra: User and programmer information," 2 1989.

[76] E. Ishiguro, T. Arai, M. Mizushima, and M. Kotani, "On the polarizability of the hydrogen molecule," *Proceedings of the Physical Society. Section A*, vol. 65, pp. 178–187, 3 1952.

[77] R. H. Tipping and J. F. Ogilvie, "Herman-wallis factors for raman transitions of 1-state diatomic molecules," *Journal of Raman Spectroscopy*, vol. 15, pp. 38–40, 2 1984.

[78] C. D. Allemand, "Depolarization ratio measurements in raman spectrometry," *Applied Spectroscopy*, vol. 24, pp. 348–353, 5 1970.

[79] P. Atkins and J. de Paula, *Physical Chemistry.* 8th ed., 2006.

[80] G. Herzberg and B. L. Crawford, "Infrared and raman spectra of polyatomic molecules.," *The Journal of Physical Chemistry*, vol. 50, pp. 288–288, 3 1946.

[81] T. Y. Chen, C. J. Kliewer, B. M. Goldberg, E. Kolemen, and Y. Ju, "Time-domain modelling and thermometry of the ch4 ¡math altimg="si1.svg"¿ ¡msub¿ ¡mi¿¡/mi¿ ¡mn¿1¡/mn¿ ¡/msub¿ ¡/math¿ q-branch using hybrid femtosecond/picosecond coherent anti-stokes raman scattering," *Combustion and Flame*, vol. 224, pp. 183–195, 2 2021.

[82] J. M. L. Martin, T. J. Lee, P. R. Taylor, and J. François, "The anharmonic force field of ethylene, c ¡sub¿2¡/sub¿ h ¡sub¿4¡/sub¿ , by means of accurate ¡i¿ab initio¡/i¿ calculations," *The Journal of Chemical Physics*, vol. 103, pp. 2589–2602, 8 1995.

[83] J. Kiefer, T. Seeger, S. Steuer, S. Schorsch, M. C. Weikl, and A. Leipertz, "Design and characterization of a raman-scattering-based sensor system for temporally resolved gas analysis and its application in a gas turbine power plant," *Measurement Science and Technology*, vol. 19, p. 085408, 8 2008.

[84] A. Braeuer and A. Leipertz, "Two-dimensional raman mole-fraction and temperature measurements for hydrogen-nitrogen mixture analysis," *Applied Optics*, vol. 48, p. B57, 2 2009.